EFFICIENT DISCRETE MODELLING OF AXISYMMETRIC RADIATING STRUCTURES

by

Oluwafunmilayo Agunlejika, B.Tech, M.Sc

A Doctoral Thesis submitted in partial fulfilment of the requirements for the award of Doctor of Philosophy (PhD) at Loughborough University

December 2015

DEDICATION

To my Parents, Samuel and Charlotte Adejumobi

Thank you for giving me the basic foundation of education: the launching pad to higher altitude and wings to fly to my dreams.

ABSTRACT

This thesis describes research on ‘Efficient Discrete Modelling of Axisymmetric Radiating Structures’. Investigating the possibilities of surmounting the inherent limitation in the Cartesian rectangular Transmission Line Modelling (TLM) method due to staircase approximation by efficiently implementing the 3D cylindrical TLM mesh led to the development of a numerical model for simulating axisymmetric radiating structures such as cylindrical and conical monopole antennas.

Following a brief introduction to the TLM method, potential applications of the method are presented. Cubic and cylindrical TLM models have been implemented in MATLAB and the code has been validated against microwave cavity benchmark problems. The results are compared to analytical results and the results obtained from the use of commercial cubic model (CST) in order to highlight the benefit of using a cylindrical model over its cubic counterpart.

A cylindrical TLM mesh has not previously been used in the modelling of axisymmetric 3D radiating structures. In this thesis, it has been applied to the modelling of both cylindrical monopole and the conical monopole. The technique can also be applied to any radiating structure with axisymmetric cylindrical shape. The application of the method also led to the development of a novel conical antenna with periodic slot loading. Prototype antennas have been fabricated and measured to validate the simulated results for the antennas.

ACKNOWLEDGEMENTS

My greatest appreciation goes to God, who has been my anchor through this journey.

I would like to thank my supervisors, Dr. James A. Flint and Mr. Robert D. Seager for their helpful suggestions and guidance. It made me chuckle now when I think of how much I have improved over the period of this research. You gave me enough room to be independent yet stayed close enough to support me whenever I hit the challenging walls that littered the path of success. Thank you for believing in me.

Special thanks go to my internal assessor, Dr. S.C. Pomeroy whose yearly evaluation and positive suggestions have helped channel the research to a lovely conclusion. I am also grateful to my external examiner, Prof. Alistair Duffy for his rigorous professional examination of this thesis work. I appreciate Prof. Donard De Cogan for his valuable suggestions regarding the centre termination of the cylindrical cavity and Prof. Christos Christopoulos for his thoughtful recommendation. My appreciations also go to Dr. Alford Chuaraya, Garry Wagg, Terry West and Phil Armistead for their help with the antenna fabrication and measurements. Thanks to Dr. Shiyu Shang for his help with the 3D printing of the dielectric load for the antenna slot.

The work presented was partly supported with funds from the Schlumberger Foundation for the Future Faculty and the Petroleum Technology Development Fund. I took the risk of starting my research without any sponsorship. That was not a bright idea but it has ended well. Thank you for coming to my aid.

My gratitude goes to my parents and my siblings. No bird can fly without wings. Dad and mum, you gave me wings when you gave me the basic

education on which I can build a career. Moreover, thank you mum for coming over into the cold weather of UK to take care of my children in time of need. Dad, you are no longer around to see me finish this but your words kept me going when the going became tough. I truly miss you. To my siblings, I sincerely appreciate your timely calls and encouragements.

I will like to say thank you to all the lovely people I met at the University and in my local Churches at Nottingham and Loughborough during my years of studies at Loughborough University. You have all contributed to the success of this research. Special thanks go to: Bukola Oke, Chinwe Njoku, Ozak Esu, Phil Ogun, Isaac Daniel, Segun Aina, Peter Awe, Sola and Yemi Ogunkeyede, Tasos Deligiannis, Ben Clark, Parthepan and Elijah Adegoke, Pastor Alawale, Pastor Joseph Nipah, Rev. Phil Weaver and Rev. David Holmes.

I will also like to appreciate my husband, Ezekiel and my children, Temi and Femi for their understanding and continuous support. Thank you Ezekiel, you made me a strong woman and I know there is no hurdle too high to surmount. Temi and Femi, you have the first hand idea of the cost of mummy's Ph.D. You are fantastic and I want you to know that I love you so much.

O. Agunlejika

December, 2015

AUTHORS' PUBLICATIONS

[1] O. Agunlejika, J. A. Flint, and R. D. Seager, "Transmission Line Modelling of Axisymmetry Curvilinear Structures," *IET Colloquium on Antennas, Wireless and Electromagnetics*, 2014, pp. 1–18, London, United Kingdom.

[2] O. Agunlejika, J. A Flint, and R. D. Seager, "Application of Cylindrical Transmission Line Method to the Modelling of Curvilinear Axisymmetric Radiating Structure," *Loughborough Antennas and Propagation Conference (LAPC)*, 2014, pp. 340–343, Loughborough, United Kingdom.

[3] O. Agunlejika, J. A. Flint, and R. D. Seager, "Transmission Line Modelling of Cylindrical Cavity Loaded with a Slotted Dielectric Rod," in *IEEE International RF and Microwave*, 2015, pp. 3–6, Kuching, Malaysia.

[4] O. Agunlejika, J. A. Flint, and R. D. Seager, "Parametric Study of the Effect of Annular Slot on the Operating Frequency of Solid Cone Antenna," in *2016 International Workshop on Antenna Technology (iWAT)*, 2016, pp. 73–76, Florida, USA.

[5] O. Agunlejika, J. A. Flint, and R. D. Seager, "Solid Conical Antenna with Annular Slots," *Applied Computational Electromagnetics*, 2016, pp. 25-26, Hawaii, USA.

TABLE OF CONTENTS

LIST OF ABBREVIATIONS

Abbreviation	Expansion
2D	Two Dimensional
3D	Three Dimensional
ABC	Absorbing Boundary Condition
CAN	Asymmetrical Condensed Node
EM	Electromagnetics
EMC	Electromagnetic Compatibility
FDBPM	Finite Difference Beam Propagation Method
FDFD	Finite Difference Frequency Domain Method
FDFEM	Frequency Domain Finite Element Method
FDTD	Finite Difference Time Domain Method
FEM	Finite Element Method
FMM	Fast Multipole Methods
HSCN	Hybrid Symmetrical Condensed Node
MoM	Methods of Moments
SCN	Symmetrical Condensed Node
SSCN	Symmetrical Super-Condensed Node
TDFEM	Time Domain Finite Element Method
TDIE	Time Domain Integral Equation
TE	Transverse Electric

TLM	Transmission Line Modelling method
TLS	The solver developed by the author
TM	Transverse Magnetic
Γ	TLM reflection coefficient

SYMBOLS FOR ELECTROMAGNETICS, PHYSICAL PROPERTIES OF MATERIALS AND WAVES

Symbol	Denotes
E_r, E_θ, E_z	Electric field components in cylindrical coordinate (Vm^{-1})
H_r, H_θ, H_z	Magnetic field components in cylindrical coordinate (Am^{-1})
Y_0	Intrinsic admittance of free space ($1/Z_0$)
ε_0	Permittivity of free space ($8.85 \times 10^{-12} Fm^{-1}$)
ε_r	Relative Permittivity (dimensionless)
μ_0	Permeability of free space ($4\pi \times 10^{-7} Hm^{-1}$)
μ_r	Relative Permeability (dimensionless)
$\boldsymbol{D}, D_x, D_y, D_z$	Electric flux density and components (Cm^{-2})
F	Frequency (Hz)
T	Time (s)
Z_0	Intrinsic impedance of free space
ρ	The electric charge density (Cm^{-3})).
c	Velocity of electromagnetic propagation in free space (ms^{-1})
$\boldsymbol{B}, B_x, B_y, B_z$	Magnetic flux density and components (Wbm^{-1})
$\boldsymbol{E}, E_x, E_y, E_z$	Electric field strength vector and components in rectangular Cartesian coordinate (Vm^{-1})
$\boldsymbol{H}, H_x, H_y, H_z$	Magnetic field strength vector and components in

	rectangular Cartesian coordinate (Am^{-1})
$\boldsymbol{J}, J_x, J_y, J_z$	Current density vector and components (Am^{-2})
ε	Absolute Permittivity (Fm^{-1})
μ	Absolute Permeability (Hm^{-1})

CIRCUIT THEORY AND TLM NOTATION

Symbol	Denotes
$\boldsymbol{Y}_{oq}$	The normalised characteristic admittance of a capacitive stub (dimensionless)
Z_0	Characteristic impedance of free space (≅ 377Ω)
Z_l	Characteristic impedance of the link line (Ω)
Z_s	Surface impedance of the boundary (Ω)
$\boldsymbol{Z}_{sq}$	The normalised characteristic impedance of an inductive stub (dimensionless)
f_c	TLM mesh dispersion cut-off frequency (Hz)
v_{tlm}	Velocity of waves in TLM (ms^{-1})
λ_m	The modelled wavelength (m)
Δl	Space step (m)
$\Delta r, \Delta T, \Delta z$	Node dimensions for a cylindrical node (m)
Δt	Time step (s)
$\Delta x, \Delta y, \Delta z$	Node dimensions for a rectangular node (m)
C	Capacitance (F)
G	Conductance (S)
I	Nodal current (A)
L	Inductance (H)
R	Resistance (Ω)

Symbol	**Denotes**
V	Nodal voltage (V)
Y	Transmission line characteristic admittance (S)
Z	Transmission line characteristic impedance (Ω)
Γ	TLM reflection coefficient
S	Scattering matrix
σ	Electric conductivity (Sm^{-1})
λ	Wavelength (m)
τ	Transmission coefficient

MATHEMATICS SYMBOLS

Symbols	Denotes
$\nabla . \boldsymbol{A}$	Divergence of vector A (Scalar dot product)
$\nabla \times \boldsymbol{A}$	Curl of vector A (Vector cross product)
∞	Infinity
i, j, k	Dummy indices
π	Ratio of circumference to diameter ≈ 3.141593

LIST OF FIGURES

LIST OF TABLES

CHAPTER 1

INTRODUCTION

Axisymmetric structures are found frequently in microwave engineering, such as those found in microwave cavities, coaxial transmission lines, wire antennas and broadband antennas. The behaviour of these structures, as well as most systems in Electromagnetics (EM), can be described by Maxwell's equations. To understand the propagation of the EM waves in these structures and the materials they are made up of, Maxwell's equations have to be solved either in differential or integral form. A few of these structures such as simple strip lines have simple reliable analytic solutions to the Maxwell's equations. However, many systems in practice are complex and the solutions to the equations are not trivial. Therefore, numerical solutions using computer simulations are employed in practice.

These methods of solving complex problems using computer simulation are commonly referred to as numerical modelling techniques. Numerical modelling techniques involve discretising the equations in time or frequency as well as in space, such that the equations can be solved using a computer. A wide range of numerical techniques for solving electromagnetic problems in both differential and integral forms have been developed.

The field of study that deals with solving EM problems using numerical techniques, also known as computer simulation techniques, is commonly referred to as Computational Electromagnetics (CEM). CEM is a demanding branch of engineering because the EM waves propagate over large distances in a very short time and each material the propagating waves

come in contact with also interacts with the waves. Further complication is added to the analysis of these waves by the anisotropic and non-linear behaviour of the materials they come in contact with. The aim of this thesis is to model axisymmetric radiating structures using a CEM method called the Transmission Line Modelling (TLM) method or the Transmission Line Matrix method.

Since the pioneering article on the TLM method was published by Johns and Buerle in 1971 [1], the method has been studied extensively and has become a powerful numerical tool in solving electromagnetic (EM) problems. It is gaining increasing acceptance in the EM community because of its stability, ease of application and capability for wideband applications [2]. TLM has been successfully applied to simulate a wide range of microwave problems and it has been found useful when modelling antennas in complex environments [3]–[5]. The application of rectangular Cartesian TLM to the modelling of radiating structures is not a new concept and it has been extensively reported in the literature [6]–[9].

However, this numerical modelling method involves the representation of the problem space in a discretised manner; a procedure simply referred to as meshing of the simulation space. A TLM mesh in its basic form is rectangular in nature and this makes mesh-to-structure conformity a problem when modelling structures with curved features [10]. This difficulty is a result of the fact that curved boundaries are approximated to fit the numerical cells, resulting in a staircase approximation error at the curved edges. Although many commercial solvers apply the TLM method to the analysis of microwave structures, the simulations are based on rectangular meshes [11]. Consequently, this results in a requirement to use a large number of steps to represent smooth edges.

Since the accurate solution of problems in electromagnetics ideally requires conformity of the mesh with the structure being modelled, meshes have to be formed in such a way that they map into the problem space or into the system of interest as closely as possible [12]. In this regard, particular attention is required in the description of localised geometry details and geometrical features that have curved boundary when modelling complex systems. When applying a rectangular TLM mesh to simulate antennas, the common option for an acceptable level of accuracy to be obtained is to perform *mesh adaptation* such that a finer mesh is used around the curved boundaries [13]. The accuracy obtained through mesh adaptation comes at the cost of an increase in both computer storage and computation time as demonstrated in Chapter 3. Unstructured meshes such as the triangular and tetrahedral meshes, which are more adaptable to the modelled structure have recently been developed for TLM simulation method [14], [15]. However, the generation of these adaptable meshes can also be mathematically intensive depending on the nature of the object/structure to be modelled. Since the nodes in these meshes have different scattering behaviour, large storage space is also required to process and store the scatter-connect procedure information for every node in the mesh [14]. Moreover, to achieve an acceptable level of accuracy, these unstructured meshes, like their rectangular counterpart, require some form of modification to fit curved edges to the mesh.

To improve accuracy and still optimise storage and computation time, curvilinear meshes where curved lines are used in the mesh formulation have been proposed for better mesh-to-structure conformity [16]–[20]. The cylindrical TLM mesh is an example of one of these curvilinear meshes. A planar circular microstrip antenna has been reported to be successfully simulated using cylindrical mesh [11] but there has not been any known work done on nonplanar 3D antenna structures using cylindrical mesh. In

this thesis, the application of curvilinear cylindrical TLM mesh to modelling of radiating structures with axisymmetric shape is discussed.

1.1 THE PROBLEM STATEMENT

The efficient incorporation of suitably structured meshes in full-field time domain models for accurate description of curved boundaries where the need is to avoid staircase approximations is a challenging procedure [21]. With increasing technological advancement, the requirement for accurate and efficient antenna design processes is becoming more important. This poses a problem because many of the modelling tools in existence for solving electromagnetic problems are either based on a rectangular Cartesian mesh or other parallelepiped meshes with sharp corners. However, when it comes to the modelling of radiating structures with curved boundaries, the fundamental issues of the staircase approximation error in rectangular Cartesian TLM mesh comes into play.

Substantial work has been done to improve the TLM method but the issues associated with accurate and efficient representation of curved boundaries are a point of concern [22]–[24]. In this research, a numerical model for axisymmetric radiating structures with curved boundaries is developed, based on the 3D cylindrical TLM algorithm.

1.2 FOCUS OF RESEARCH

This aim of this research is to improve the accuracy of modelling axisymmetric structures by implementing a 3D cylindrical TLM mesh. The research investigates the possibilities of surmounting the staircase approximation limitation that is inherent in the rectangular Cartesian TLM by efficiently implementing the 3D cylindrical TLM mesh. The investigation results in the development of a numerical model for simulating

axisymmetric radiating structures such as cylindrical and conical monopole antenna. The developed model maximises the efficiency of TLM in antenna modelling by exploiting the axisymmetric nature of these radiating structures of interest to save time and computer resources and improving the capability of TLM in ultra-wide band applications.

The objectives are:

- To bridge the gap between the theoretical foundations of cylindrical TLM and its applications.
- To develop a simulation code for solving electromagnetic problems in MATLAB using the TLM algorithm
- To investigate the performance of the developed numerical solver.
- To model axisymmetric radiating structures such as dipole, monopole and wideband conical antenna structures using the developed solver.
- To study the effects of slots and dielectric loaded slots on the performance of the conical antenna.

1.3 CHOICE OF MODELLING METHOD

CEM has experienced a phenomenal growth in the electromagnetic community and time domain differential methods are becoming increasingly popular [25]–[27]. This is due to the fact that they are versatile in handling complex electromagnetic problems and provide simulation results that are meaningful to microwave engineers and circuit designers. Research into numerical modelling techniques has evolved over the years and has been established in different fields of applications. Some of the computational methods that are more widely used are Finite Element Method - Frequency Domain Finite Element Method (FD-FEM) and Time Domain Finite Element Method (TD-FEM) [28], Finite Difference Methods - Finite

Difference Beam Propagation Method (FD-BPM), Finite Difference Time Domain (FDTD) method and Finite Difference Frequency Domain method (FDFD) [29]–[31], Transmission Line Modelling method (TLM) [32], Time Domain Integral Equation (TDIE) techniques [33], [34], Method of Moments (MOM) [35] and Fast Multipole Methods (FMM) [36], Geometrical Theory of Diffraction (GTD) [37] and Finite Integration Technique (FIT) [38] to mention a few.

The various available methods offer a wide range of modelling capabilities with varying accuracy. The finite difference method (FDTD or FDFD) involves spatial discretisation into rectangular blocks and it is commonly applied in time domain form. It produces electric and magnetic fields at alternate halves of the time step if applied in the time domain version but the frequency domain application requires the solution of a set of simultaneous linear equations. It is suitable for complex geometry but boundaries generally must lie on cell faces, which lead to staircase approximations of curved boundaries [31], [39]. The Finite Element Method (FDFEM or TDFEM) involves spatial discretisation into tetrahedral blocks. It is most commonly formulated in the frequency domain. It operates by reducing the problem to a set of simultaneous linear equations, which are then solved by minimising energy functional. Complex configurations and material types are easily achieved in FEM and it is possible to attain accurate geometry representation because the elements can be individually scaled to fit the problem at hand. However, the flexibility of the element shapes means that more effort, than what is required for rectangular discretisation, goes into data preparation in FEM and with complicated geometry; FEM use a lot of elements, particularly near to small geometrical features [40]. In MOM, the modelling space is discretised into wires, conducting patches or dielectric volumes. Although the time domain MOM exists, it is commonly applied in the frequency domain. It functions by reducing the integral form of Maxwell’s equation to a set of simpler linear

equations, which are then solved by the technique called “the method of weighted residuals”. The implementation of highly accurate absorbing boundaries is possible in MOM. However, different forms of the field integral equations apply to different sort of problem, which means that combining two problem types such as wire and patches on a single modelling space is not a trivial thing to accomplish [35].

The axisymmetric structures considered in this thesis include cylindrical dipole, cylindrical monopole and conical dipole antennas. These structures may be broadband in nature depending on their configurations. Computational tools for broadband operations in most cases are simulated in the time domain [21]. This is due to the fact that in dealing with the most general material and conductor configurations at high frequencies, differential time-domain techniques offer the most versatile simulation tool. They have the capability of covering a wide frequency band in a single simulation with an impulsive excitation and allow for solutions without the need to solve large linear systems of equations [41]. Moreover, when solving complex electromagnetic problems or modelling electromagnetic fields in the time domain, the spectral characteristics are obtained over a wide range of frequencies and the EM wave can be easily traced [42]. Transient phenomena can also be studied directly and dispersive and non-linear behaviour can be easily modelled [43]. They are also particularly well suited for implementation on parallel or vector processors [43]. In addition, getting results in the frequency domain is not a problem because results obtained in the time domain can easily be converted to frequency domain using Fourier Transform [44]. In this light, FDTD and TLM are two appealing numerical methods.

FDTD and TLM are both full-wave numerical techniques for solving Maxwell’s equations and are closely related [45]. TLM nodes are modelled using equivalent transmission lines for each node while FDTD models the

propagation through the elements using a discrete form of Maxwell's curl equation. Results obtained from the two models have even been found to have equivalent results in certain situations [46] [47]. For instance, Hoefer [43] suggested that dispersion of the propagation vector is a good basis for comparing discrete time domain field models and he investigated the dispersion characteristic of TLM and FDTD equivalent schemes. He concluded that the two models lead to practically identical results and he recommended that the final choice between TLM and FDTD depends on personal preferences and familiarity with one or the other method. A school of thought says there is some difference between the two methods in term of their formulation but Jin and Vahldieck [48] researched the derivation of TLM using centred differencing and averaging and reported a positive outcome, meaning that TLM can be formulated as the physical model of a transmission line network or as the mathematical model of Maxwell's equations. Another school of thought suggested that the only difference between the two lies in their field of application - FDTD found more application in radiation and scattering while TLM has found its major use in guided propagation problems[49]. However, more recent research has proved that TLM can be equally applied in radiating and scattering problems as FDTD [50] proving this distinction to be invalid.

As closely related as the two techniques are, TLM has been found to have advantages over FDTD in certain applications. For instance, the TLM boundary description is found to be twice as fine in relation to the FDTD and TLM provides engineers with conceptual models using transmission line rather than a mathematical model using differencing as applied in the finite difference methods [51]. Furthermore, both electric and magnetic field components are available at the same time step in TLM, which means that all six field components can be access at one point in space, while they are separated by half-time step in FDTD [52]; TLM stability has been found to be better than that of FDTD in materials with high permittivity and TLM

also performs better in modelling the fields around sharp conducting edges [30].

Moreover, TLM is a conceptually simple but powerful technique for solving electromagnetic problems and the method has been proven to be well suited to analysing complex electromagnetic structures [53]. It is a time-based numerical modelling method [3] [54] meaning that it can produce an impulse response for the modelled system, which makes it suitable for wideband applications [2]. It has been known to be a versatile numerical tool in solving electromagnetic (EM) problems because of its stability and ease of application [55] and it has the benefit of being a relatively straightforward algorithm that is easy to implement [2]. It also has the ability to take into account the local material properties, which means that inhomogeneous materials can be described and complex physical structures can be modelled. For this thesis, the computational tool of choice is the TLM method.

1.4 NOVELTY OF RESEARCH

For objects with curved edges, it has been found that the TLM cylindrical mesh yields more accurate results and brings about a reduction in the number of nodes required for simulation compared to using a rectangular Cartesian or other parallelepiped mesh. A TLM solver based on both rectangular Cartesian and cylindrical TLM meshes has been developed in MATLAB to verify this fact. This solver has the capability to simulate microwave cavity problems and resonant structures. Canonical microwave cavity problems with known analytical solutions have been simulated using the developed solver and the results are encouraging. The cylindrical mesh also allows the exploitation of symmetry and this results in optimised modelling time when modelling cylindrical curvilinear structures.

Radiating structures such as dipole, monopole and conical antennas were modelled using the developed cylindrical solver. The simulation produced results such as the operating frequency of the antenna, which agree with analytical expectations. Prototype antennas were fabricated and measured to validate the simulated results and the results compared well.

A novel conical antenna with periodic slot loading was developed and measured. The simulation was conducted using the newly developed solver and the proposed antennas fabricated and measured for results comparison. Parametric studies on the effects of slot parameters such as its position, depth, width and permittivity (dielectric loading) on the performance of the solid cone antenna was carried out. Features displayed by the slotted-cone antennas can be used as a tool for frequency selective property in conical antennas operation, adjusting the operation bandwidth of a cone antenna and to reject a band of unwanted frequencies. The inclusion of removable dielectric material in the slots means that dielectric materials of various permittivity values can be used to shift the operating frequency as desired.

1.5 STRUCTURE OF THESIS

Chapter 2 reviews the fundamentals of TLM. The derivations of the rectangular TLM parameters and the formulations of TLM algorithm for both 2D and 3D electric waves are also presented.

Chapter 3 is dedicated to simulations of canonical problems with known theoretical solutions with the intention to validate the rectangular Cartesian part of the code written for this research (TLS).

Chapter 4 deals with the fundamentals of cylindrical TLM and simulated results for benchmarked microwave problems solved with cylindrical mesh of the developed solver.

Chapter 5 describes the application of the cylindrical TLM to the modelling of axisymmetric radiating structures. Measured results of the fabricated prototype compared to the simulated cylindrical and conical monopole antennas are presented.

In Chapter 6, the modelling of axisymmetric conical antennas with incorporated slots is described. Measured results of fabricated prototype slotted-cone antennas are compared to the simulated results.

In Chapter 7, general remarks on the results achieved in the process of modelling the axisymmetric radiating structures effectively using TLM mesh and directions for further research are outlined.

CHAPTER 2

INTRODUCTION TO TRANSMISSION LINE MODELLING THEORY

This Chapter gives a general introduction to the Transmission Line Modelling (TLM) method. The historical background of TLM method, the theoretical relations of rectangular TLM nodes to the Maxwell's equations, the TLM implementation procedure and boundary application in TLM method are discussed.

2.1 EVOLUTION OF TLM: THE HISTORICAL BACKGROUND

TLM has developed steadily over the years and is still evolving. The work of Johns and Beurle in 1971 [1] started the research into TLM method and played a significant role in its development. They were the first to propose the TLM formulation of Maxwell's equations. Their work was inspired by the circuit analogy of EM phenomena proposed by Kron in 1944 [56]. Johns and Beurle described a novel numerical technique for solving two-dimensional (2D) problems based on Huygens' principle [57]. Huygens' Principle simply states that secondary wavelets that spread outward with a speed equal to the speed of light are generated from every point of a wave front. It can be inferred that every point in an EM wave acts as a source of the continuing wave if Huygens' analysis is considered in the light of Ampere's law (a flowing current in a conductor gives rise to a magnetic

field) and Faraday's law (varying magnetic field gives rise to an electric field).

The theory of TLM is based on Maxwell's equations in differential form [3] but the algorithm is relatively straight-forward to implement because it uses the concepts of circuit theory [2]. TLM does not solve the mathematics of Maxwell's equations directly but conceptually fills the simulation space with transmission lines and calculates both the electric and magnetic fields using the scatter-connect procedure of pulse propagation along the link lines in the modelling space [58]**.** Time is also discretised in TLM models such that the scatter-connect procedure takes place within a stipulated discrete timeframe. As in any numerical method, the simulation space is finite and is normally truncated at its periphery by the application of suitable *boundaries*. Boundaries are implemented by applying various reflection coefficients to the pulse arriving at the boundaries. They are applied at the points of transition between two different materials in inhomogeneous media and at the simulation edge. These boundaries are either placed at the centre of the nodes nearest to the position where the boundary is required or between two adjacent nodes nearest to the targeted position.

2D TLM was the first TLM structure developed. It was made up of two transmission lines connected at the centre. The connecting point was referred to as the *node*; a grid of these nodes was called a *mesh* and the connecting lines between two nodes were called *link lines*. This structure was named *shunt node* based on the nature of its connection at the node [1]. The shunt node was later optimised to accommodate the modelling of inhomogeneous and lossy material and the corresponding *series node* was also developed [59], [60]. A typical 2D node is as shown in Fig. 2.1.

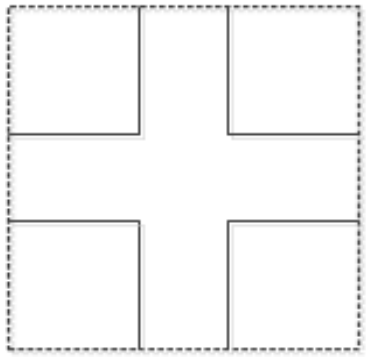

Fig. 2.1: A typical 2D TLM node.

Following the successful development of 2D TLM, Akhtarzad and Johns developed the *Expanded TLM node* [10]. Problems mostly encountered in general engineering applications are three dimensional (3D); therefore the expanded TLM node was developed to address these types of problems. Its development involved the combination of series and shunt nodes to represent the six fields in space [10] . Its equivalent circuit consists of three shunt and three series nodes electrically connected. The expanded TLM node is similar in structure to the Finite Difference Frequency Domain (FDTD) scheme developed by Yee [31] but unlike FDTD, it uses more variables. The expanded node, however, has the advantage of generating three of the six field components at each scattering point instead of one as is the case in FDTD. The expanded TLM node is as shown in Fig. 2.2.

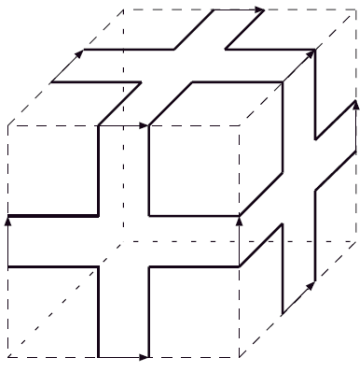

Fig. 2.2: The Expanded Node after Trenkic [62].

The complicated topology of the expanded TLM node is a disadvantage because the scattering procedure at its shunt nodes has a shift of half a discretisation interval in time with respect to scattering in its series nodes [63]. The implication of the shift is that field components with different polarisations are calculated at points that are physically separated, which makes it difficult to apply boundary conditions. The inability to place boundaries correctly introduced possible errors especially when dealing with the interfaces between different materials [53]. The theory of the expanded node was reviewed in detail by Hoefer [22]. Some of the shortcomings observed in the Expanded TLM node application were improved on by Saguet and Pic [64] and led to the development of the *Asymmetrical Condensed Node* (ACN) shown in Fig. 2.3.

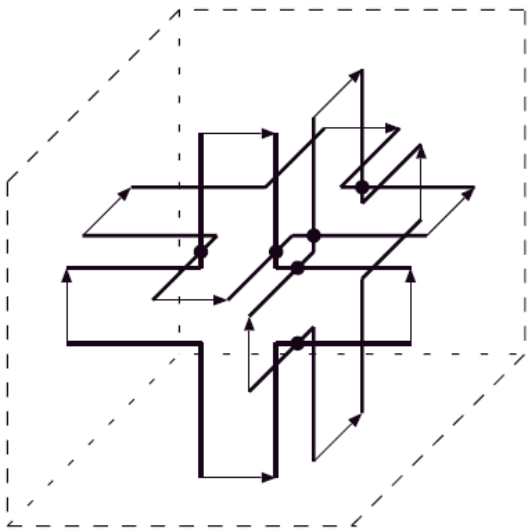

Fig. 2.3: The Asymmetrical Condensed Node after Trenkic [62].

The ACN has the advantage of performing the scattering operation at one point, which makes it more efficient in terms of computational resources. In addition, all the field components can be obtained at a single point at the same time and the boundary can be easily placed either at the centre of the node or between two nodes. However, like the Expanded Node, the ACN

node is asymmetric in nature and the first connection at the node can either be series or shunt depending on the direction of approach. The implication of this is that the boundaries may have slightly different properties when approached from different sides and this difference can be significant when dealing with high frequencies [65]. The ACN was later developed into *Symmetrical Condensed Node* (SCN) by Johns [53]. A typical SCN is as shown in Fig. 2.4.

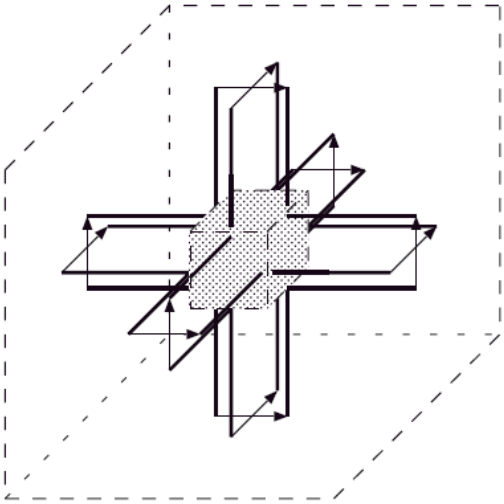

Fig. 2.4: Symmetrical Condensed Node after Trenkic [62].

The SCN provides the six field components at the same point and allows for easy placement of boundaries especially in inhomogeneous media. It is fully symmetric, which removes the difficulties associated with the asymmetric structures. The symmetry gives better accuracy and reduced dispersion when using irregular nodes in a mesh[66]. The theory and application of the SCN TLM is detailed in [3].

This thesis will be limited to the use of the 2D and the 3D SCN TLM techniques but it is worth mentioning that various other techniques have since been developed to enhance the implementation of TLM. Some of these developments allow for arbitrary shapes and geometries with fine

details to be modelled in TLM using hybrid variable mesh techniques [67], multi-grid techniques [16], [68]–[70] and general curvilinear meshes [71]–[73]. Cylindrical TLM is a typical example of the curvilinear mesh. The theory and implementation of this technique will be discussed to detail in Chapter 4.

Some other developments such as the variation of the characteristic impedance of the link lines to form hybrid TLM mesh such as Hybrid Symmetrical Condensed TLM Nodes and Symmetrical Super-Condensed TLM Nodes [74], [75] and the development of the Frequency Domain TLM (FDTLM) [76]–[78] have resulted in a more efficient implementation of TLM.

2.2 MAXWELL'S EQUATIONS AND RECTANGULAR CARTESIAN TLM ANALOGIES

As earlier mentioned in Section 2.1, Maxwell's equations in differential form are the basis for the theory of TLM. The components of the transmission lines are derived from the analogy between Maxwell's equations and equations guiding the propagation of waves called *wave equations*. The ease with which the TLM can be applied means that it is possible to use it without an in-depth understanding of its relation to the basic Maxwell's equations it solves [79]. In this Section, the relationship between Maxwell's equations and the TLM components will be explored. In its simplest form, the TLM mesh is a rectangular Cartesian grid of uniformly spaced intersecting transmission lines. This basic structure is what gave it the name rectangular Cartesian TLM. For the rest of this thesis, it will simply be referred to as rectangular TLM mesh. The focus of this Section will be on the analogies of the Maxwell's equations to the rectangular TLM mesh.

2.2.1 MAXWELL'S EQUATIONS IN RECTANGULAR CARTESIAN FORM

Generally, Maxwell's equations is expressed as [3]

$$\nabla \times \boldsymbol{H} = \boldsymbol{J} + \frac{\partial \boldsymbol{D}}{\partial t} \tag{2.1}$$

$$\nabla \times \boldsymbol{E} = -\frac{\partial \boldsymbol{B}}{\partial t} \tag{2.2}$$

$$\nabla . \boldsymbol{D} = \rho \tag{2.3}$$

$$\nabla . \boldsymbol{B} = 0 \tag{2.4}$$

where $\boldsymbol{H}$ is magnetic field strength (Am^{-1}), **E** is the electric field strength (Vm^{-1}); $\boldsymbol{D}$ is the electric displacement field (Cm^{-2})); $\boldsymbol{B}$ is magnetic flux density (T or Wbm^{-1}); $\boldsymbol{J}$ is the conduction current density (Am^{-2}); ρ is the electric charge density (Cm^{-3})).

In linear, isotropic, non-dispersive materials, $\boldsymbol{D}$ and $\boldsymbol{B}$ are related to $\boldsymbol{H}$ and $\boldsymbol{E}$ by

$$\begin{aligned} \boldsymbol{D} &= \varepsilon \boldsymbol{E} = \varepsilon_0 \varepsilon_r \boldsymbol{E} \\ \boldsymbol{B} &= \mu \boldsymbol{H} = \mu_0 \mu_r \boldsymbol{H} \end{aligned} \tag{2.5}$$

where ε and μ are the permittivity and permeability of the medium respectively, ε_r and μ_r are the relative permittivity and relative permeability of the material respectively and ε_0 (= $8.85\times10^{-12}\ Fm^{-1}$) and μ_0 ($= 4\pi \times 10^{-7} \cong 1.26 \times 10^{-6}\ Hm^{-1}$) are the permittivity and permeability of free space respectively.

In rectangular coordinates, Maxwell's curl equation (2.1) can be expressed as (2.6) - (2.8); (2.2) expressed as (2.9) - (2.11); (2.3) as (2.12) and (2.4) as (2.13).

$$\frac{\partial H_z}{\partial y} - \frac{\partial H_y}{\partial z} = J_x + \frac{\partial D_x}{\partial t} \tag{2.6}$$

$$\frac{\partial H_x}{\partial z} - \frac{\partial H_z}{\partial x} = J_y + \frac{\partial D_y}{\partial t} \tag{2.7}$$

$$\frac{\partial H_y}{\partial x} - \frac{\partial H_x}{\partial y} = J_z + \frac{\partial D_z}{\partial t} \tag{2.8}$$

$$\frac{\partial E_z}{\partial y} - \frac{\partial E_y}{\partial z} = -\frac{\partial B_x}{\partial t} \tag{2.9}$$

$$\frac{\partial E_x}{\partial z} - \frac{\partial E_z}{\partial x} = -\frac{\partial B_y}{\partial t} \tag{2.10}$$

$$\frac{\partial E_y}{\partial x} - \frac{\partial E_x}{\partial y} = -\frac{\partial B_z}{\partial t} \tag{2.11}$$

$$\frac{\partial E_x}{\partial x} + \frac{\partial E_y}{\partial y} + \frac{\partial E_z}{\partial z} = \frac{\rho}{\varepsilon} \tag{2.12}$$

$$\frac{\partial H_x}{\partial x} + \frac{\partial H_y}{\partial y} + \frac{\partial H_z}{\partial z} = 0 \tag{2.13}$$

where H_x, H_y, H_z are the magnetic field components in x, y and z direction; E_x, E_y, E_z are the electric field components in x, y and z directions; B_x, B_y, B_z are magnetic field components in the x, y and z direction; D_x, D_y, D_z are the electric displacement fields in the x, y and z directions.

In this Section, Maxwell's equations have been expressed in rectangular coordinate. These equations will be used in Section 2.3.2 to show the relationship of the Maxwell's equations to the parameters of the rectangular TLM.

2.2.2 ANALOGIES OF MAXWELL'S EQUATIONS TO THE RECTANGULAR TLM CIRCUIT PARAMETERS

It is important to understand the composition of the rectangular TLM model in order to compare it to Maxwell's equations. The basic building block for the TLM algorithm is the 2D model, which has two configurations on the *x-y* plane – the shunt and the series configurations. The shunt configuration models magnetic fields transverse to the direction of propagation of the EM wave and admits only electric field components in the direction of propagation, which means that the non-zero field components modelled are: H_x, H_y and E_z. This is termed the *Transverse Magnetic mode* (*TM mode*). The TLM series configuration models electric field components that are transverse to the direction of propagation and admits only magnetic field components in the direction of propagation, which implies that the non-zero field components are E_x, E_y and H_z. This is referred to as the *Transverse Electric mode* (*TE mode*). Nevertheless, both the series and the shunt nodes can be used in simulating either TE or TM modes by applying the principle of duality in electromagnetics [3], as long as the appropriate analogy between the circuit quantities and the fields is established. For simplicity, the two models will be discussed separately and then the results will be combined to form equations for general TLM nodes.

In the shunt node configuration, other field components beside H_x, H_y and E_z are set to zero and the Maxwell's equations reduce to:

$$\frac{\partial E_z}{\partial y} = -\mu \frac{\partial H_x}{\partial t} \tag{2.14}$$

$$-\frac{\partial E_z}{\partial x} = -\mu \frac{\partial H_y}{\partial t} \tag{2.15}$$

$$\frac{\partial H_y}{\partial x} - \frac{\partial H_x}{\partial y} = \varepsilon \frac{\partial E_z}{\partial t} \tag{2.16}$$

Differentiating equation (2.14) and (2.15) with respect to y and x respectively, adding the resulting equation and combining with equation (2.16) eliminates the magnetic field component to give (2.17), which is the wave equation for 2-D propagation in rectangular form.

$$\frac{\partial^2 E_z}{\partial x^2} + \frac{\partial^2 E_z}{\partial y^2} = \mu\, \varepsilon \frac{\partial^2 E_z}{\partial t^2} \tag{2.17}$$

In order to represent the Maxwell's equations according to Huygens's principle, both space and time are divided into finite discrete elementary units [80]. The length between two consecutive nodes is called *discrete length/ discrete space-step* as shown in Fig. 2.5. The discrete length is denoted Δx, Δy or Δz depending on the direction of interest as illustrated in Fig. 2.5.

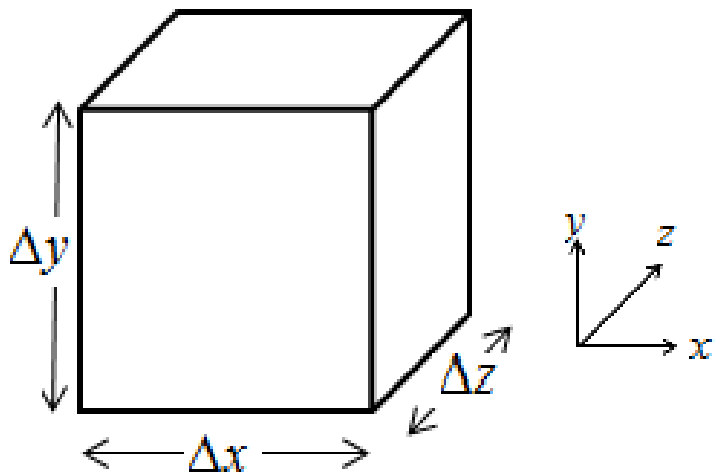

Fig. 2.5: Discrete length in TLM node.

For general use, it is usual to simply refer to the discrete length as Δl and this is obtained by finding the minimum value among Δl_x, Δl_y and Δl_z , which are functions of Δx, Δy and Δz and are given as:

$$\Delta l_x = \frac{\Delta y \Delta z}{\Delta x}$$

$$\Delta l_y = \frac{\Delta x \Delta z}{\Delta y} \tag{2.18}$$

$$\Delta l_z = \frac{\Delta x \Delta y}{\Delta z}$$

The electrical components of a single shunt node are as shown in Fig. 2.6. Assuming an equal small space-step in all propagation directions i.e.$\Delta l \rightarrow 0$, then the differential equation describing the circuit quantities may be expressed as:

$$\frac{\partial V_z}{\partial y} = -L \frac{\partial I_y}{\partial t} \tag{2.19}$$

$$-\frac{\partial V_z}{\partial x} = -L \frac{\partial I_x}{\partial t} \tag{2.20}$$

$$\frac{\partial I_y}{\partial y} + \frac{\partial I_x}{\partial x} = -2C \frac{\partial V_z}{\partial t} \tag{2.21}$$

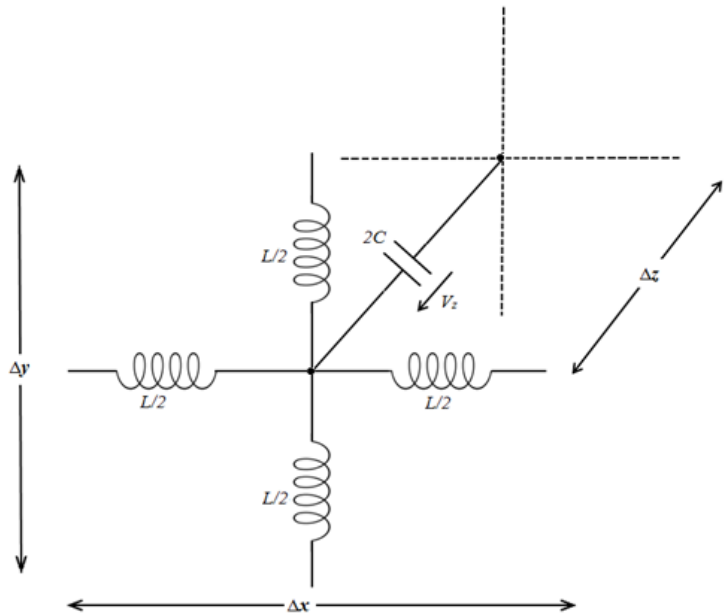

Fig. 2.6: Shunt 2D TLM node

Differentiating equation (2.19) and (2.20) with respect to y and x respectively, adding the resulting equations and combining it with equation (2.21) eliminates the current terms and gives (2.22)

$$\frac{\partial^2 V_z}{\partial x^2} + \frac{\partial^2 V_z}{\partial y^2} = 2LC\frac{\partial^2 V_z}{\partial t^2} \tag{2.22}$$

Equation (2.21) is isomorphic to (2.16) and (2.22) is isomorphic to (2.17). When the equations are compared the following equivalences are established:

- the electric field component (E) maps unto the electric potential (V) to give

$$E_z = -\frac{V_z}{\Delta l} \tag{2.23}$$

- magnetic field component (H) maps unto the nodal current (I) to give

$$H_y = -\frac{I_x}{\Delta l} \tag{2.24}$$

$$H_x = -\frac{I_y}{\Delta l} \tag{2.25}$$

- the permeability (μ) maps unto inductance (L) to give:

$$L = \mu \Delta l \tag{2.26}$$

- and permittivity (ε) maps unto capacitance (C) to give:

$$2C = \varepsilon \Delta l \tag{2.27}$$

Solutions to the Maxwell's equations and their analogies to the TLM parameters, for the series configuration shown in Fig. 2.7 are obtained by following the same procedure as with the shunt TLM configuration.

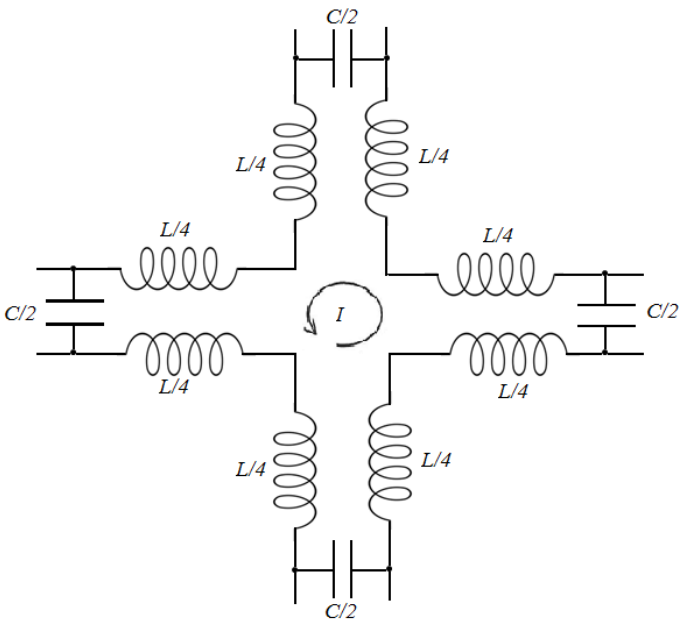

Fig. 2.7: Series 2D TLM node.

The non-zero field components are E_x, E_y and H_z. Maxwell's equations then reduce to:

$$\frac{\partial H_z}{\partial y} = \varepsilon \frac{\partial E_x}{\partial t} \tag{2.28}$$

$$-\frac{\partial H_z}{\partial x} = \varepsilon \frac{\partial E_y}{\partial t} \tag{2.29}$$

$$\frac{\partial E_y}{\partial x} - \frac{\partial E_x}{\partial y} = -\mu \frac{\partial H_x}{\partial t} \tag{2.30}$$

and the mapping equations are:

$$\frac{\partial I_y}{\partial z} = -C\frac{\partial V_x}{\partial t} \tag{2.31}$$

$$\frac{\partial I_y}{\partial x} = -C\frac{\partial V_z}{\partial t} \tag{2.32}$$

$$\frac{\partial V_x}{\partial z} + \frac{\partial V_z}{\partial x} = -2L\frac{\partial I_y}{\partial t} \tag{2.33}$$

The mapping of (2.30) into (2.33) results in the magnetic field component (H_z) as given in (2.34) and the inductance (L) in (2.36). (2.28) and (2.29) maps unto (2.31) and (2.32) respectively to give the electric field components given in (2.35) and the capacitance (C) as shown in (2.36)

$$H_z = -\frac{I_z}{\Delta l} \tag{2.34}$$

$$\begin{aligned} E_x &= -\frac{V_x}{\Delta l} \\ E_y &= -\frac{V_y}{\Delta l} \end{aligned} \tag{2.35}$$

$$2L = \mu\Delta l \tag{2.36}$$

$$C = \varepsilon\Delta l \tag{2.37}$$

2.2.3 DERIVATION OF TLM NODE PARAMETERS

The relationship between Maxwell's equations and the parameters of the TLM was established in Section 2.3.2. In this Section, the procedure for determining the TLM parameters is discussed.

For a 3D TLM node, there are parameter variations in three dimensions and the total capacitance, *C* of the node given in (2.27) can be expressed as (2.38):

$$C = \begin{bmatrix} C_x \\ C_y \\ C_z \end{bmatrix} \tag{2.38}$$

where C_x , C_y and C_z are the capacitance values for the *x*, *y*, and *z* dimensions expressed as (2.39) [16]

$$C_x = \varepsilon_x \Delta l_x\,;\;\; C_y = \varepsilon_y \Delta l_y;\;\; C_z = \varepsilon_z \Delta l_z \tag{2.39}$$

In the same manner, the total inductance of the node, *L* given in (2.26) can be expressed as (2.40):

$$L = \begin{bmatrix} L_x \\ L_y \\ L_z \end{bmatrix} \tag{2.40}$$

where L_x , L_y and L_z are the inductance values for the *x*, *y*, and *z* dimensions expressed as (2.41) [16]:

$$L_x = \mu_x \Delta l_x;\;\; L_y = \mu_y \Delta l_y;\;\; L_z = \mu_z \Delta l_z \tag{2.41}$$

In the TLM mesh, the time it takes for the pulse to travel the node distance (Δx, Δy or Δz) and arrive back at the centre of the nodes is called the time-step (Δt). During the scatter-connect procedure of the TLM scheme, some of the scatter pulses propagate forward to connect with the adjacent nodes while some reflect back to the originating node within this constant propagation time, Δt. It is essential that all pulses, transmitting or reflecting, arrive back at the centre of nodes at the same time. This requirement is termed *synchronism* and it is very crucial to the stability of the TLM scheme. In order to fulfil this requirement, it is important to know the velocity of propagation along the link lines and determine an appropriate value of Δt. The procedure for determining this will be discussed later in this Chapter.

Up to this point, equal space-step (Δl) assumption in all directions has been made but this may not be applicable in practice because inhomogeneous and lossy materials are used for various purposes. Numerical problems containing materials with relative permittivity and relative permeability greater than 1 ($\varepsilon_r > 1,\ \mu_r > 1$) vary the speed of waves and the space-step has to be adjusted accordingly in order to maintain synchronism in the scatter-connect procedure of the TLM scheme. Some problems require that the simulation space be modelled with meshes of various node sizes. Thus, special methods for handling irregular and non–uniform nodes, while maintaining synchronism in the scatter-connect procedure of the TLM, become necessary. One of the approaches for doing this is the introduction of stubs.

The stub works in such a way as to increase the local permittivity and permeability without affecting the synchronism in the circuit. When dealing with inhomogeneous materials or non-cuboid nodes, stubs are added to the nodes to account for variability in the permeability and/or permittivity of the medium [81]. They are also added in order to account for losses in the medium and to correct for variation in distances travel by pulse when

travelling through a mesh of non-cubic node. The capacitive stub, also known as open-circuit stub, models additional permittivity by increasing the capacitance and it generally applies in shunt-connected networks. It is achieved by maintaining an open-circuit at one end of the transmission line section implying a reflection coefficient of 1. The inductive stub models additional permeability in series-connected networks by increasing the inductance and this is achieved by short-circuiting one end of the transmission line section. A reflection coefficient of -1 applies. To maintain synchronism, they are designed such that a pulse propagates from the node centre to the stub termination in half the discretised time ($\Delta t/_2$) in order to ensure that any pulse incident on a stub returns back to the node at time, Δt. As shown in Fig. 2.8, the scattered pulse at **B** takes time Δt to arrive at junction **A** while the pulse scattered into the stub at node **A** takes time $\Delta t/_2$ to arrive at the junction, meaning the two pulses arrive at node junction **A** at the same time before the scattering procedure is repeated.

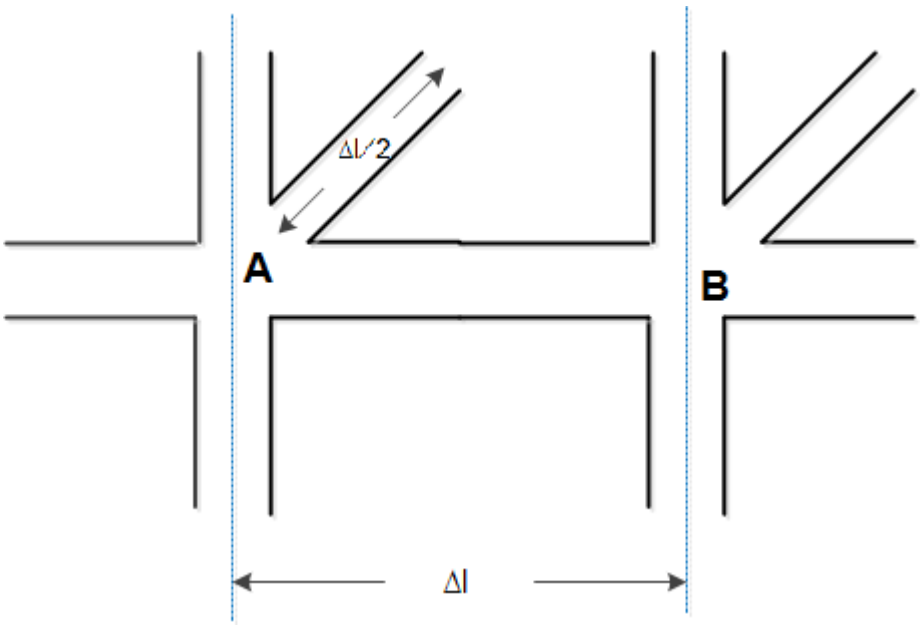

Fig. 2.8: Stub application in TLM.

Equations (2.39) and (2.41) are essential to the proper modelling of any TLM node irrespective of the combination of link lines and stubs it is made up of. For example, the total capacitance modelled by the SCN node in one direction is represented by the distributed capacitances of the transmission lines and stub polarised in that direction. This means that the total capacitance modelled by an SCN in the z-direction (C_z) is represented by the distributed capacitance of the z-polarised transmission lines of length Δx and Δy plus the capacitance of the open-circuit stub in the z-direction (C_{oz}), expressed as (2.42):

$$C_z = C_{xz}\Delta x + C_{yz}\Delta y + C_{oz} \tag{2.42}$$

The total capacitance equation for the other directions can be expressed as (2.43) - (2.44):

$$C_x = C_{zx}\Delta z + C_{yx}\Delta y + C_{ox} \tag{2.43}$$

$$C_y = C_{xy}\Delta x + C_{zy}\Delta z + C_{oy} \tag{2.44}$$

In the same way, the total inductance modelled by the SCN in the z-direction (L_z) is represented by the distributed capacitance of the z-polarised transmission lines of length Δx and Δy and the inductance of the short-circuit stub in the z-direction (L_{sz}) as (2.45):

$$L_z = L_{xy}\Delta x + L_{yx}\Delta y + L_{sz} \tag{2.45}$$

Total inductance equations for the other directions can also be expressed as (2.46) - (2.47):

$$L_x = L_{yz}\Delta y + L_{zy}\Delta z + L_{sx} \tag{2.46}$$

$$L_y = L_{xz}\Delta x + L_{zx}\Delta z + L_{sy} \tag{2.47}$$

Equations (2.48) - (2.53) represent the correct modelling of the simulated medium using any type of the 3D node and these are obtained by substituting (2.42) - (2.44) in (2.39) and (2.45) - (2.47) in (2.41)

$$C_{xz}\Delta x + C_{yz}\Delta y + C_{oz} = \varepsilon_x \Delta l_x \tag{2.48}$$

$$C_{xy}\Delta x + C_{zy}\Delta z + C_{oy} = \varepsilon_y \Delta l_y \tag{2.49}$$

$$C_{xz}\Delta x + C_{yz}\Delta y + C_{oz} = \varepsilon_z \Delta l_z \tag{2.50}$$

$$L_{xy}\Delta x + L_{yx}\Delta y + L_{sz} = \mu_x \Delta l_x \tag{2.51}$$

$$L_{yz}\Delta y + L_{zy}\Delta z + L_{sx} = \mu_y \Delta l_y \tag{2.52}$$

$$L_{xz}\Delta x + L_{zx}\Delta z + L_{sy} = \mu_z \Delta l_z \tag{2.53}$$

As earlier mentioned, the value of Δt in the TLM scheme is related to the velocity of propagation along the link lines. The velocity of propagation along specific transmission link lines is a function of the distributed capacitance and inductance in that direction. It can be calculated as the ratio of the node distance to the time-step, i.e. the velocity of propagation along *x*-directed, *z*-polarised link line, for instance, is given by (2.54) and (2.55):

$$v_{xz} = \frac{1}{\sqrt{L_{xz}C_{xz}}} \tag{2.54}$$

$$v_{xz} = \frac{\Delta x}{\Delta t} \tag{2.55}$$

Combining (2.54) and (2.55), time synchronism can be enforced on the link line *xz* as (2.56):

$$\Delta t = \frac{\Delta x}{v_{xz}} = \Delta x\sqrt{L_{xz}C_{xz}} \tag{2.56}$$

Similarly, the time-step for the other link line can be calculated as (2.57) - (2.61):

$$\Delta t = \frac{\Delta x}{v_{xy}} = \Delta x\sqrt{L_{xy}C_{xy}} \tag{2.57}$$

$$\Delta t = \frac{\Delta y}{v_{yx}} = \Delta y\sqrt{L_{yx}C_{yx}} \tag{2.58}$$

$$\Delta t = \frac{\Delta y}{v_{yz}} = \Delta y\sqrt{L_{yz}C_{yz}} \tag{2.59}$$

$$\Delta t = \frac{\Delta z}{v_{zx}} = \Delta z\sqrt{L_{zx}C_{zx}} \tag{2.60}$$

$$\Delta t = \frac{\Delta z}{v_{zy}} = \Delta z\sqrt{L_{zy}C_{zy}} \tag{2.61}$$

Other important parameters in TLM are the characteristic impedances (Z) and admittances (Y) of the link lines. The characteristic impedance of an x-directed, *z*-polarised link line is given as (2.62):

$$Z_{xz} = \sqrt{\frac{L_{xz}}{C_{xz}}} = \frac{1}{Y_{xz}} \tag{2.62}$$

The relationship between Δt, Y_{xz} and Z_{xz} can be obtained by combining (2.56) and (2.62) as in (2.63) and (2.64). Similar equations can be obtained for the other five link lines.

$$Z_{xz} = \sqrt{\frac{L_{xz}\Delta x}{\Delta t}} \tag{2.63}$$

and

$$Y_{xz} = \sqrt{\frac{C_{xz}\Delta x}{\Delta t}} \tag{2.64}$$

In conventional TLM nodes, it is required that the link lines have the characteristic impedance of the background medium [82], usually assumed to be free-space. The impedance and admittance of the free space are calculated as (2.65):

$$\begin{aligned} Z_0 &= \sqrt{\mu_0/\varepsilon_0} \\ Y_0 &= 1/Z_0 \end{aligned} \tag{2.65}$$

The characteristic admittance of a capacitive stub, Y_{oq} is given as (2.66) and the characteristic impedance of an inductive stub, Z_{sq} is given as (2.67) [83]

$$Y_{oq} = \frac{2C_{oq}}{\Delta t} \tag{2.66}$$

$$Z_{sq} = \frac{2L_{sq}}{\Delta t} \tag{2.67}$$

where subscript o and s signify open-circuit stub and short-circuit stub respectively and q represents the coordinate axis. C_{oq} is the stub capacitance and L_{sq} is the stub inductance

The description of the physical property of the medium is achieved by a combination of its parameters - the capacitance (2.48) - (2.50), the inductance (2.51) - (2.53) and the conditions for time synchronism (2.56 - 2.61). The combination of these three parameters gives (2.68) - (2.73):

$$\left(Z_{xy} + Z_{yx} + Z_{sz}\right)/2 = \mu_z \frac{\Delta x \Delta y}{\Delta z \Delta t} \tag{2.68}$$

$$\left(Z_{yz} + Z_{zy} + Z_{sx}\right)/2 = \mu_x \frac{\Delta y \Delta z}{\Delta x \Delta t} \tag{2.69}$$

$$\left(Z_{xz} + Z_{zx} + Z_{sy}\right)/2 = \mu_y \frac{\Delta x \Delta z}{\Delta y \Delta t} \tag{2.70}$$

$$\left(Y_{xz} + Y_{yz} + Y_{oz}\right)/2 = \varepsilon_z \frac{\Delta x \Delta y}{\Delta z \Delta t} \tag{2.71}$$

$$\left(Y_{xy} + Y_{zy} + Y_{oy}\right)/2 = \varepsilon_y \frac{\Delta x \Delta z}{\Delta y \Delta t} \tag{2.72}$$

$$\left(Y_{yx} + Y_{zx} + Y_{ox}\right)/2 = \varepsilon_x \frac{\Delta y \Delta z}{\Delta x \Delta t} \tag{2.73}$$

Link and stub parameters ($\boldsymbol{Y}_{oq}$ and $\boldsymbol{Z}_{sq}$) can be obtained using either (2.68) – (2.73) or (2.48) - (2.53). By imposing the constraint of having free-space as the background medium [82], the impedance of the link lines become the impedance of free space and (2.68) - (2.73) can be simplified to obtain Y_{oq} and Z_{sq} as (2.74) - (2.75):

$$\boldsymbol{Y}_{oq} = 2Y_0\left(\frac{\varepsilon_{rq}\Delta l_q}{c\Delta t} - 2\right) \tag{2.74}$$

$$\boldsymbol{Z}_{sq} = 2Z_0\left(\frac{\mu_{rq}\Delta l_q}{c\Delta t} - 2\right) \tag{2.75}$$

In an application where only a slice of the model is required, meaning that 2D TLM will be more efficient for the simulation, there is a little change to the calculation of the link line impedance. The impedance of link lines for 2D-TLM is $Z_0\sqrt{2} = \sqrt{2\mu_0/\varepsilon_0}$. This constraint changes the stub equations (2.74) and (2.75) to (2.76) and (2.77):

$$\boldsymbol{Y}_{oq} = 2Y_0\left(\frac{\varepsilon_{rq}\Delta l_q}{c\Delta t} - \sqrt{2}\right) \tag{2.76}$$

$$\boldsymbol{Z}_{sq} = 2Z_0\left(\frac{\mu_{rq}\Delta l_q}{c\Delta t} - \sqrt{2}\right) \tag{2.77}$$

It is important to note is that in practical problems, the modelling space is not loss free and the effect of these losses may need to be accounted for in the TLM formulations. Stubs of infinite lengths can be inserted at the scattering junction of node to represent these losses [75]. A stub that serves as a lossy element does not reflect any pulse but dissipates all of the energy that enters it. In this way, it models the dissipation of energy without tampering with the velocity of wave propagation. In 2D networks, a shunt conductance, G gives electric losses by modelling electric conductivity while series resistance, R gives magnetic losses in series 2D network by modelling the magnetic conductivity. In an SCN network, six additional stubs are required, one shunt conductance, G_q and one series resistance, R_q for each of the three directions. They are given as (2.78) and (2.79):

$$G_q = \sigma_{eq} \Delta l_q \tag{2.78}$$

$$R_q = \sigma_{mq} \Delta l_q \tag{2.79}$$

where σ_{eq} signifies electric conductivities and σ_{mq} magnetic conductivities respectively in q coordinate axis.

In summary, when modelling materials with arbitrary permittivity and permeability or using graded mesh (i.e. use of discretisation nodes of arbitrary aspect ratio), open and short-circuit stubs are added to the conventional TLM [53]. Six stubs are added to the SCN node to account for the irregularity in mesh and material properties and another six to account for losses in the node. A node with stubs is usually referred to as a stub-loaded SCN. However, some disadvantages associated with the addition of the stubs include more demand for storage capacity, more dispersion and the necessity to keep the time-step small in order to avoid introducing stubs

with negative impedance, which bring about instabilities in the TLM scheme [84].

Other approaches have been developed to address the issue of non-uniform grids and changes in permittivity and permeability when modelling homogenous media in TLM. These methods involve changing the characteristic impedances of the link lines. One example of this method is the Symmetrical Super-Condensed Node (SSCN) [85]. Stubs are not required in the implementation of the SSCN [86]. Permittivity and permeability of the simulated medium are modelled into the link lines as inductances and capacitances, making the characteristic impedance of the six link lines at each node to be different to one another. One problem with SSCN is the requirement to model reflection/transmission processes at the boundaries between distinct node regions to account for the differences in link line impedances. In some cases, both the application of stubs and modification of link line impedance are combined to model an inhomogeneous medium as in Hybrid SCN, HSCN [67] [74], [87]. HSCN has two configurations, type 1 HSCN and type 2 HSCN. Type 1 HSCN is a TLM node whereby all inductances are modelled by the link lines and hence there is no need for inductive stubs. Type 2 HSCN may be implemented where all capacitances are modelled by the link lines and there are no capacitive stubs. The HSCN does not require as much storage space as stub-loaded SCN for general problems. It has better dispersion properties and can be operated with larger time-steps compared to the stub-loaded SCN [24].

2.3 IMPLEMENTATION OF THE TLM ALGORITHM

The derivation of the TLM node parameters has been established in Section 2.2. In this Section, the procedure for the implementation of the TLM algorithm will be discussed.

In 1690, Huygens stated that each point on the wave-front acts as an isotopic spherical radiator and the superposition of all the elementary point radiators forms a new wave-front [57]. This is the mechanism by which wave-front propagates and it is the method adopted in the formulation of the TLM procedure.

Solving electromagnetic problems with TLM involves populating the entire problem space with a grid of transmission lines in each direction and launching an excitation at a node of choice depending on the nature of the problem [58]**.** The pulse reflected from a node impinges on another node adjacent to it and sets up a spherical wave. Every voltage pulse that arrives at a particular transmission line is regarded as an incident voltage and is represented with the superscript *i* while the scattered/reflected voltage travelling away from the node is represented with the superscript *r*. The pulse propagates and scatters on the entire grid of lines that make up the modelling medium. The procedure by which TLM models the EM field propagation in the modelling space is termed the *scatter-connect procedure* [7], [88]. Before describing the scatter-connect procedure in detail in the next Section, it is important to first define some useful notations.

Voltages leaving or arriving at the ports of the node are called *port voltages*. They are named using a three-letter subscript convention proposed by Trenkic et al [85]. The first letter of the subscript represents the direction of the propagation, the second represent the position of the voltage pulse relative to the centre of the node (positive, *p* or negative, *n* side of the coordinate axis) and the third letter indicates the direction of polarisation of

the voltage pulse. Using dummy indices i and j, we can write a general notation for voltage pulses at the node as V_{inj} and V_{ipj}. The voltage V_{inj} then represents a voltage pulse on the negative side of the node along an i-directed, j-polarised transmission line and V_{ipj} is the voltage on the positive side of the same line. For the twelve link line voltages of the SCN, these dummy indices should be replaced by x, y, z, where $i, j \in \{x, y, z\}$ and $i \neq j$. For example, the port voltage V_{xnz} represents an x-directed voltage pulse, located on the negative/left side of the node-centre and polarised in the z-direction. To differentiate between the reflected and the incident voltages at the port, a superscript letter r or i is added to the voltage such as V_{xny}^{i} and V_{xny}^{r}. The notations for the link line currents follow the same principle as the link voltages.

2.3.1 SCATTER-CONNECT PROCEDURE IN 2D TLM

A 2D TLM node consists of two intersecting transmission lines of equal lengths and characteristic impedance, Z_0. The intersection of the lines forms a node with four ports. When a pulse of 1V is launched on one of the 4 ports to excite the node as shown in Fig. 2.9, it travels to the intersecting junction between the lines. The pulse scatters at the junction and follows all available channels. The energy at the excited node is conserved and the incident pulse spreads isotropically from the node junction to become incident on adjacent nodes.

In a shunt configuration, the link lines are arranged in parallel. The 1V incidence pulse entering from one of the four ports into the node sees three link lines in parallel. At the junction, the effective impedance Z_L seen by the incident pulse is $Z_L = Z_0/3$. The reflection coefficient, Γ is calculated as

$$\Gamma = (Z_L - Z_0)/(Z_L + Z_0) = -0.5 \tag{2.80}$$

and the transmission coefficient, τ is

$$\tau = 2Z_L/(Z_L + Z_0) = 0.5 \tag{2.81}$$

The incident pulse generates four new pulses at the junction – three transmitted and 1 reflected as shown in Fig. 2.9. The four new pulses form a spherical wave of 0.5V in each direction depicting Huygens principle in a discrete way. The 0.5V pulse is transmitted to each of the link lines and the -0.5V scattered pulse combines with the incident pulse to form 0.5V pulse, which causes the continuity around the node to be maintained. The scattered pulses travel through the link lines to the adjacent nodes and become the incident pulses on these nodes. As it arrives at the adjacent node, it sets up a secondary radiation as shown in Fig. 2.10. It is this principle of scatter and connect that characterises the TLM procedure.

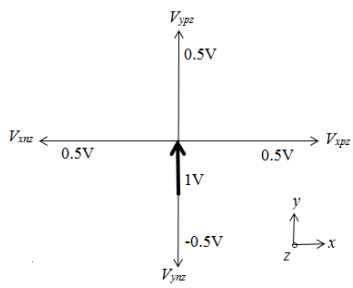

Fig. 2.9: Voltage scattering at the incident node of a 2D TLM.

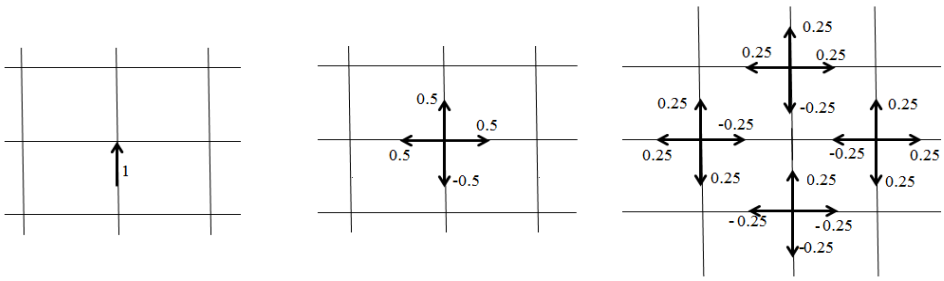

Fig. 2.10: The scatter-connect procedure in 2D TLM.

Equations guiding the scattering procedure of the TLM nodes are obtained using the Thevenin's equivalent circuit models for the shunt and series nodes shown in Fig. 2.11 and Fig. 2.12 respectively.

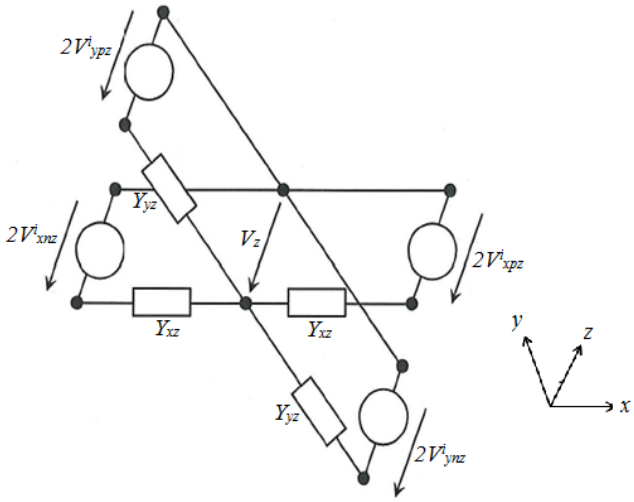

Fig. 2.11: Thevenin equivalent circuit for the 2D shunt TLM node after Flint [89].

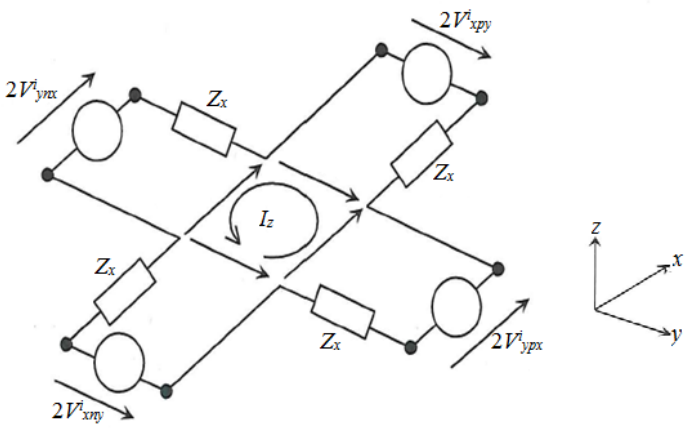

Fig. 2.12: Thevenin equivalent circuit for the 2D series TLM node after Flint [89].

In 2D TLM, equations relating the input and output voltages for nodes with equal discrete lengths in all dimensions are expressed in matrix as [3]:

$$V^r = SV^i \tag{2.82}$$

where V^i is given as:

$$V^i = \begin{bmatrix} V^i_{xnz} \\ V^i_{xpz} \\ V^i_{ynz} \\ V^i_{ypz} \end{bmatrix} \tag{2.83}$$

V^r as:

$$V^r = \begin{bmatrix} V^r_{xnz} \\ V^r_{xpz} \\ V^r_{ynz} \\ V^r_{ypz} \end{bmatrix} \tag{2.84}$$

and S is the scattering matrix. For the shunt 2D TLM, S is expressed as:

$$S = 0.5 \begin{bmatrix} -1 & 1 & 1 & 1 \\ 1 & -1 & 1 & 1 \\ 1 & 1 & -1 & 1 \\ 1 & 1 & 1 & -1 \end{bmatrix} \tag{2.85}$$

and for the series 2D TLM, S is expressed as:

$$S = 0.5 \begin{bmatrix} 1 & 1 & 1 & -1 \\ 1 & 1 & -1 & 1 \\ 1 & -1 & 1 & 1 \\ -1 & 1 & 1 & 1 \end{bmatrix} \tag{2.86}$$

Equations (2.82) - (2.86) were implemented in the developed solver to obtain reflected voltages at the node of the 2D model.

The reflected/scattered voltages are connected to the adjacent nodes and they are scattered again at the junction of the next node. The connection between nodes in a typical 2D TLM mesh is shown in Fig. 2.13 and the connection is guided by [3] :

$$
\begin{aligned}
V_{xpz}^{i}(x,y,z) &= V_{xnz}^{r}(x+1,y,z) \\
V_{xnz}^{i}(x+1,y,z) &= V_{xpz}^{r}(x,y,z) \\
V_{ypz}^{i}(x,y,z) &= V_{ynz}^{r}(x,y+1,z) \\
V_{ynz}^{i}(x,y+1,z) &= V_{ypz}^{r}(x,y,z)
\end{aligned}
\tag{2.87}
$$

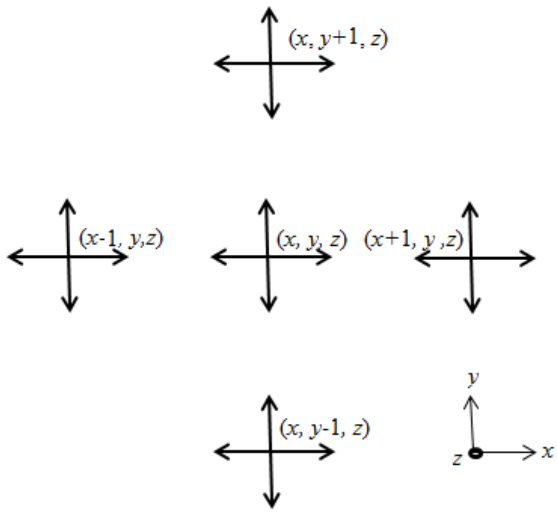

Fig. 2.13: Connection process on a 2D TLM mesh.

The field components in the mesh are calculated for the shunt node as:

$$
\begin{aligned}
E_z &= -\frac{V_z}{\Delta l} = -\frac{0.5\left(V_{xpz}+V_{xnz}+V_{ypz}+V_{ynz}\right)}{\Delta l} \\
H_y &= -\frac{I_x}{\Delta l} = -\frac{\left(V_{xnz}-V_{xpz}\right)}{Z_{tl}\Delta l}
\end{aligned}
\tag{2.88}
$$

$$H_x = -\frac{I_y}{\Delta l} = -\frac{\left(V_{ypz} - V_{ynz}\right)}{Z_{tl}\Delta l}$$

and for the series node:

$$H_z = -\frac{I_z}{\Delta l} = -\frac{0.5\left(V_{ynz} - V_{xnz} - V_{ypz} + V_{xpz}\right)}{Z_{tl}\Delta l}$$

$$E_x = -\frac{V_x}{\Delta l} = \frac{\left(V_{ynz} + V_{ypz}\right)}{\Delta l} \tag{2.89}$$

$$E_y = -\frac{V_y}{\Delta l} = \frac{\left(V_{xnz} + V_{xpz}\right)}{\Delta l}$$

2.3.2 SCATTER AND CONNECT PROCEDURE IN 3D SYMMETRICAL CONDENSED NODE TLM

The 3D SCN model [90] follows the same scattering and connecting procedure as that of the 2D. It is however more complex in that the link at the junction is a virtual connection. The 3D node combines the series and shunt modes of the 2D TLM nodes.

In a 3D workspace, there are six intersecting transmission lines interconnected in such a way that each node face has two corresponding orthogonal ports thereby giving rise to twelve ports per node. The 3D SCN node structure is as shown in Fig. 2.14. The field polarisations are represented by the voltages at these orthogonal ports and appropriate summation of the port voltages at the nodes results in appropriate E and H field components [91]. Parameters of the cuboid-shaped TLM node with material properties μ and ε and arbitrary dimensions Δx, Δy and Δz, can be derived using the system of equations described in this Section.

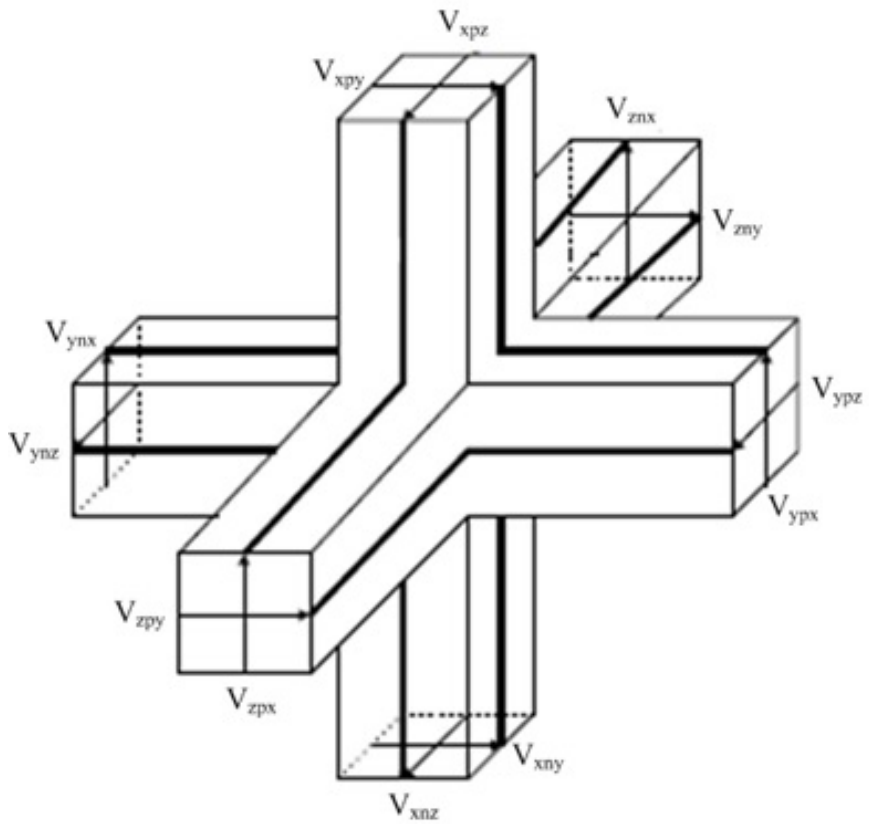

Fig. 2.14: Three-Dimensional SCN node after Johns [2].

2.3.3 DERIVATION OF TLM NODE PARAMETERS

The relationship between the Maxwell's equations and the parameters of the TLM has been established in Section 2.3.2. In this Section, the procedure for determining the TLM parameters is discussed.

For a 3D TLM node, there are parameter variations in three dimensions and the total capacitance, *C* of the node given in (2.27) can be expressed as:

$$C = \begin{bmatrix} C_x \\ C_y \\ C_z \end{bmatrix} \tag{2.90}$$

where C_x , C_y and C_z are the capacitance values for the *x*, *y*, and *z* dimensions expressed as [16]

$$C_x = \varepsilon_x \Delta l_x\,;\;\; C_y = \varepsilon_y \Delta l_y;\;\; C_z = \varepsilon_z \Delta l_z \tag{2.91}$$

In the same manner, the total inductance of the node, L given in (2.26) can be expressed as:

$$L = \begin{bmatrix} L_x \\ L_y \\ L_z \end{bmatrix} \tag{2.92}$$

where L_x , L_y and L_z are the inductance values for the *x*, *y*, and *z* dimensions expressed as [16]:

$$L_x = \mu_x \Delta l_x;\;\; L_y = \mu_y \Delta l_y;\;\; L_z = \mu_z \Delta l_z \tag{2.93}$$

In the TLM mesh, the time it takes for the pulse to travel the node distance (Δx, Δy or Δz) and arrive back at the centre of the nodes is called the time-step (Δt). During the scatter-connect procedure of the TLM scheme, some of the scatter pulses propagate forward to connect with the adjacent nodes while some reflect back to the originating node within this constant propagation time, Δt. It is essential that all pulses, transmitting or reflecting, arrive back at the centre of nodes at the same time. This requirement is termed *synchronism* and it is very crucial to the stability of the TLM scheme. In order to fulfil this requirement, it is important to know the velocity of propagation along the link lines and determine an appropriate value of Δt. The procedure for determining the value of Δt will be discussed later in this Chapter.

Up to this point, equal space-step (Δl) assumption in all directions has been made but this may not be applicable in practice because inhomogeneous and lossy materials are used for various purposes. Numerical problems containing materials with relative permittivity and relative permeability greater than 1 ($\varepsilon_r > 1,\ \mu_r > 1$) vary the speed of waves and the space-step has to be adjusted accordingly in order to maintain synchronism in the scatter-connect procedure of the TLM scheme. Some problems required that the simulation space be modelled with meshes of various node sizes. Thus, special methods for handling irregular and non–uniform nodes, while maintaining synchronism in the scatter-connect procedure of the TLM, become necessary. One of the approaches for doing this is the introduction of stubs.

The stub works in such a way as to increase the local permittivity and permeability without affecting the synchronism in the circuit. When dealing with inhomogeneous materials or non-cuboid nodes, stubs are added to the nodes to account for variability in the permeability and/or permittivity of the medium [81]. They are also added in order to account for losses in the medium and to correct for variation in distances travel by pulse when travelling through a mesh of non-cubic node. The capacitive stub, also known as open-circuit stub, models additional permittivity by increasing the capacitance and it generally applies in shunt-connected networks. It is achieved by maintaining an open-circuit at one end of the transmission line section implying a reflection coefficient of 1. The inductive stub models additional permeability in series-connected networks by increasing the inductance and this is achieved by short-circuiting one end of the transmission line section. A reflection coefficient of -1 applies. To maintain synchronism, they are designed such that a pulse propagates from the node centre to the stub termination in half the discretised time ($\Delta t/2$) in order to ensure that any pulse incident on a stub returns back to the node at time, Δt.

Equations (2.39) and (2.41) are essential to the proper modelling of any TLM node irrespective of the combination of link lines and stubs it is made up of. For example, the total capacitance modelled by SCN node in one direction is represented by the distributed capacitances of the transmission lines and stub polarised in that direction. This means that the total capacitance modelled by an SCN in the z-direction (C_z) is represented by the distributed capacitance of the z-polarised transmission lines of length Δx and Δy plus the capacitance of the open-circuit stub in the z-direction (C_{oz}), expressed as

$$C_z = C_{xz}\Delta x + C_{yz}\Delta y + C_{oz} \tag{2.94}$$

The total capacitance equation for the other directions can be expressed as:

$$C_x = C_{zx}\Delta z + C_{yx}\Delta y + C_{ox} \tag{2.95}$$

$$C_y = C_{xy}\Delta x + C_{zy}\Delta z + C_{oy} \tag{2.96}$$

In the same way, the total inductance modelled by SCN in the z-direction (L_z) is represented by the distributed capacitance of the z -polarised transmission lines of length Δx and Δy and the inductance of the short-circuit stub in the z-direction (L_{sz}) as:

$$L_z = L_{xy}\Delta x + L_{yx}\Delta y + L_{sz} \tag{2.97}$$

Total inductance equations for the other directions can also be expressed as:

$$L_x = L_{yz}\Delta y + L_{zy}\Delta z + L_{sx} \tag{2.98}$$

$$L_y = L_{xz}\Delta x + L_{zx}\Delta z + L_{sy} \tag{2.99}$$

Equations (2.48) - (2.53) represent the correct modelling of the simulated medium using any type of the 3D node and these are obtained by substituting (2.42) - (2.44) in (2.39) and (2.45) - (2.47) in (2.41)

$$C_{xz}\Delta x + C_{yz}\Delta y + C_{oz} = \varepsilon_x \Delta l_x \tag{2.100}$$

$$C_{xy}\Delta x + C_{zy}\Delta z + C_{oy} = \varepsilon_y \Delta l_y \tag{2.101}$$

$$C_{xz}\Delta x + C_{yz}\Delta y + C_{oz} = \varepsilon_z \Delta l_z \tag{2.102}$$

$$L_{xy}\Delta x + L_{yx}\Delta y + L_{sz} = \mu_x \Delta l_x \tag{2.103}$$

$$L_{yz}\Delta y + L_{zy}\Delta z + L_{sx} = \mu_y \Delta l_y \tag{2.104}$$

$$L_{xz}\Delta x + L_{zx}\Delta z + L_{sy} = \mu_z \Delta l_z \tag{2.105}$$

As earlier mentioned, the value of Δt in the TLM scheme is related to the velocity of propagation along the link lines. The velocity of propagation along specific transmission link lines is a function of the distributed capacitance and inductance in that direction. It can be calculated as the ratio of the node distance to the time-step, i.e. the velocity of propagation along *x*-directed, *z*-polarised link line, for instance, is given by (2.54) and (2.55):

$$v_{xz} = \frac{1}{\sqrt{L_{xz}C_{xz}}} \tag{2.106}$$

$$v_{xz} = \frac{\Delta x}{\Delta t} \tag{2.107}$$

Combining (2.54) and (2.55), time synchronism can be enforced on the link line *xz* as:

$$\Delta t = \frac{\Delta x}{v_{xz}} = \Delta x\sqrt{L_{xz}C_{xz}} \tag{2.108}$$

Similarly, the time-step for the other link line can be calculated as:

$$\Delta t = \frac{\Delta x}{v_{xy}} = \Delta x\sqrt{L_{xy}C_{xy}} \tag{2.109}$$

$$\Delta t = \frac{\Delta y}{v_{yx}} = \Delta y\sqrt{L_{yx}C_{yx}} \tag{2.110}$$

$$\Delta t = \frac{\Delta y}{v_{yz}} = \Delta y\sqrt{L_{yz}C_{yz}} \tag{2.111}$$

$$\Delta t = \frac{\Delta z}{v_{zx}} = \Delta z\sqrt{L_{zx}C_{zx}} \tag{2.112}$$

$$\Delta t = \frac{\Delta z}{v_{zy}} = \Delta z\sqrt{L_{zy}C_{zy}} \tag{2.113}$$

Other important parameters in TLM are the characteristic impedances (Z) and admittances (Y) of the link lines. The characteristic impedance of an x-directed, *z*-polarised link line is given as:

$$Z_{xz} = \sqrt{\frac{L_{xz}}{C_{xz}}} = \frac{1}{Y_{xz}} \tag{2.114}$$

The relationship between Δt, Y_{xz} and Z_{xz} can be obtained by combining (2.56) and (2.62) as in (2.63) and (2.64). Similar equations can be obtained for the other five link lines.

$$Z_{xz} = \sqrt{\frac{L_{xz}\Delta x}{\Delta t}} \tag{2.115}$$

and

$$Y_{xz} = \sqrt{\frac{C_{xz}\Delta x}{\Delta t}} \tag{2.116}$$

In conventional TLM nodes, it is required that the link lines have the characteristic impedance of the background medium [82], usually assumed to be free-space. The impedance and admittance of the free space are calculated as:

$$\begin{aligned} Z_0 &= \sqrt{\mu_0/\varepsilon_0} \\ Y_0 &= 1/Z_0 \end{aligned} \tag{2.117}$$

The characteristic admittance of a capacitive stub, $\boldsymbol{Y}_{oq}$ is given as (2.66) and the characteristic impedance of an inductive stub, $\boldsymbol{Z}_{sq}$ is given as [83]

$$\boldsymbol{Y}_{oq} = \frac{2C_{oq}}{\Delta t} \tag{2.118}$$

$$\boldsymbol{Z}_{sq} = \frac{2L_{sq}}{\Delta t} \tag{2.119}$$

where subscript o and s signify open-circuit stubs and short-circuit stubs respectively and q represents the coordinate axis. C_{oq} is the stub capacitance and L_{sq} is the stub inductance.

The description of the physical property of the medium is achieved by a combination of its parameters - the capacitance (2.48) - (2.50), the inductance (2.51) - (2.53) and the conditions for time synchronism (2.56 - 2.61). The combination of these three parameters gives:

$$\left(Z_{xy} + Z_{yx} + Z_{sz}\right)/2 = \mu_z \frac{\Delta x \Delta y}{\Delta z \Delta t} \tag{2.120}$$

$$\left(Z_{yz} + Z_{zy} + Z_{sx}\right)/2 = \mu_x \frac{\Delta y \Delta z}{\Delta x \Delta t} \tag{2.121}$$

$$\left(Z_{xz} + Z_{zx} + Z_{sy}\right)/2 = \mu_y \frac{\Delta x \Delta z}{\Delta y \Delta t} \tag{2.122}$$

$$\left(Y_{xz} + Y_{yz} + Y_{oz}\right)/2 = \varepsilon_z \frac{\Delta x \Delta y}{\Delta z \Delta t} \tag{2.123}$$

$$\left(Y_{xy} + Y_{zy} + Y_{oy}\right)/2 = \varepsilon_y \frac{\Delta x \Delta z}{\Delta y \Delta t} \tag{2.124}$$

$$\left(Y_{yx} + Y_{zx} + Y_{ox}\right)/2 = \varepsilon_x \frac{\Delta y \Delta z}{\Delta x \Delta t} \tag{2.125}$$

Link and stub parameters ($\boldsymbol{Y}_{oq}$ and $\boldsymbol{Z}_{sq}$) can be obtained using either (2.68) - 2.73) or (2.48) - (2.53). By imposing the constraint of having free-space as the background medium [82], the impedance of the link lines become the impedance of free space and (2.68) - (2.73) can be simplified to obtain $\boldsymbol{Y}_{oq}$ and $\boldsymbol{Z}_{sq}$ as:

$$\boldsymbol{Y}_{oq} = 2Y_0\left(\frac{\varepsilon_{rq}\Delta l_q}{c\Delta t} - 2\right) \tag{2.126}$$

$$\boldsymbol{Z}_{sq} = 2Z_0\left(\frac{\mu_{rq}\Delta l_q}{c\Delta t} - 2\right) \tag{2.127}$$

In an application where only a slice of the model is required, meaning that 2D TLM will be more efficient for the simulation, there is a little change to the calculation of the link line impedance. The impedance of link lines for the 2D TLM is $Z_0\sqrt{2} = \sqrt{2\mu_0/\varepsilon_0}$. This constraint changes the stub equations (2.74) and (2.75) to:

$$\boldsymbol{Y}_{oq} = 2Y_0\left(\frac{\varepsilon_{rq}\Delta l_q}{c\Delta t} - \sqrt{2}\right) \tag{2.128}$$

$$\boldsymbol{Z}_{sq} = 2Z_0\left(\frac{\mu_{rq}\Delta l_q}{c\Delta t} - \sqrt{2}\right) \tag{2.129}$$

It is important to note that in practical problems, the modelling space is not loss free and the effect of these losses may need to be accounted for in the TLM formulations. Stubs of infinite lengths can be inserted at the scattering junction of node to represent these losses [75]. A stub that serves as a lossy element does not reflect any pulse but dissipates all of the energy that gets to it. In this way, it models the dissipation of energy without tampering with the velocity of wave propagation. In 2D networks, a shunt conductance, G gives electric losses by modelling electric conductivity while series resistance, R gives magnetic losses in series 2D network by modelling the magnetic conductivity. In SCN network, six additional stubs are required, one shunt conductance, G_q and one series resistance, R_q for each of the three directions.

$$G_q = \sigma_{eq} \Delta l_q \tag{2.130}$$

$$R_q = \sigma_{mq} \Delta l_q \tag{2.131}$$

where σ_{eq} signifies electric conductivities and σ_{mq} magnetic conductivities respectively in q coordinate axis.

In summary, when modelling materials with arbitrary permittivity and permeability or using graded mesh (i.e. use of discretisation nodes of arbitrary aspect ratio), open and short-circuit stubs are added to the conventional TLM [53]. Six stubs are added to the SCN node to account for the irregularity in mesh and material properties and another six to account for losses in the node. A node with stubs is usually referred to as a stub-loaded SCN. However, some disadvantages associated with the addition of the stubs include more demand for storage capacity, more dispersion and the necessity to keep the time-step small in order to avoid introducing stubs

with negative impedance, which bring about instabilities in the TLM scheme [84].

Other approaches have been developed to address the issue of non-uniform grids and changes in permittivity and permeability when modelling homogenous media in TLM. These methods involve changing the characteristic impedances of the link lines. One example of this method is the Symmetrical Super-Condensed Node (SSCN) [85]. Stubs are not required in the implementation of the SSCN [86]. Permittivity and permeability of the simulated medium are modelled into the link lines as inductances and capacitances, making the characteristic impedance of the six link lines at each node to be different to one another. One problem with SSCN is the requirement to model reflection/transmission processes at the boundaries between distinct node regions to account for the differences in link line impedances. In some cases, both the application of stubs and modification of link line impedance are combined to model an inhomogeneous medium as in Hybrid SCN, HSCN [67] [74], [87]. HSCN has two configurations, type 1 HSCN and type 2 HSCN. Type 1 HSCN is a TLM node whereby all inductances are modelled by the link lines and hence there is no need for inductive stubs. Type 2 HSCN may be implemented where all capacitances are modelled by the link lines and there are no capacitive stubs. The HSCN does not require as much storage space as stub-loaded SCN for general problems. It has better dispersion properties and can be operated with larger time-steps compared to the stub-loaded SCN [24].

2.3.4 DISPERSION IN TLM

TLM, being a numerical method, is dispersive because of spatial discretisation and it is a fundamental requirement that a suitable number of nodes is used for the model [92]–[94]. The dispersive behaviour is due to the fact that the time it takes for a pulse to propagate along the mesh axis at

0^0 is not the same as the time required for the pulse to travel across the mesh diagonal path (45^0), meaning that its propagation characteristic is anisotropic as shown in Fig. 2.15.

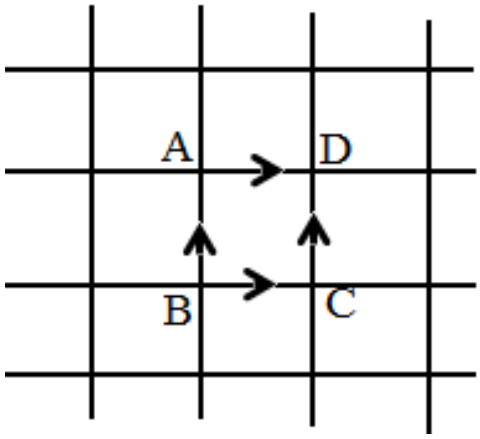

Fig. 2.15: Dispersion in TLM mesh.

If the time taken for a pulse to move from point B in the mesh to point D diagonally (BD) is *t*, then it will take the same pulse time 2*t* to reach the same point D if it travels through the axial path BAD or BCD in the mesh. In the case of the diagonal propagation, the TLM mesh propagation velocity (u_{TLM}) is given as [3]:

$$u_{TLM} = \frac{distance}{time} = \frac{\sqrt{2\Delta l}}{2\Delta t} = \frac{c}{\sqrt{2}}$$

For the axial path (0^0),

$$u_{TLM} = \frac{c\pi\left(\frac{\Delta l}{\lambda_0}\right)}{sin^{-1}\left[\sqrt{2}\, sin\left(\pi\frac{\Delta l}{\lambda_0}\right)\right]}$$

Where λ_0 is the free space wavelength

The dispersion reduces with increase in the number of nodes/ λ as depicted by the curves in Fig. 2.16.

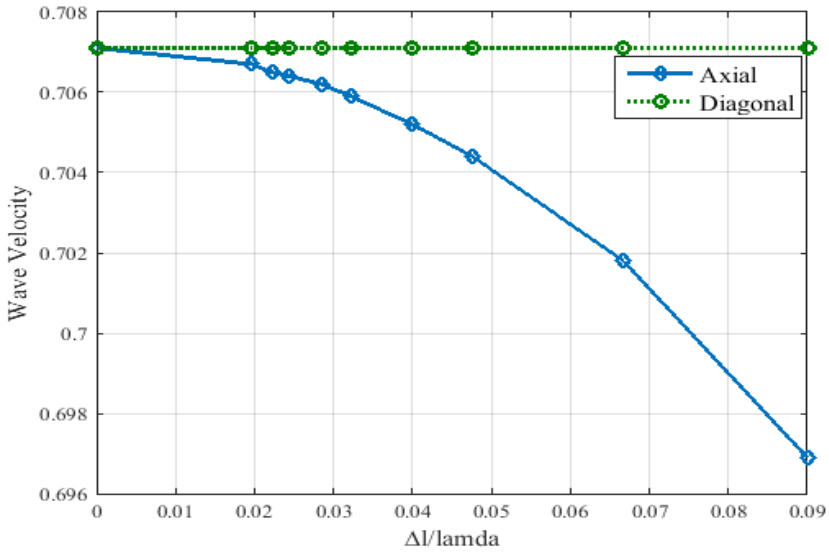

Fig. 2.16: Dispersion curve for TLM.

According to Hoefer [43], if maximum acceptable error for a model is 1%, the ratio of length discretisation to that of the wavelength ($\Delta l/\lambda$) should be smaller than 0.075, for all frequency of interest. Therefore, assuming the maximum velocity error acceptable at the highest frequency of interest is known, the dispersion curve can be used in determining the discretisation length, Δl for simulation.

2.4 BOUNDARY APPLICATION IN TLM

As earlier mentioned in Section 2.1, external boundaries are needed at the mesh edge. Therefore, boundaries are applied to restrict the computational domain in numerical modelling. To model boundaries in TLM, appropriate impulse reflection coefficients are introduced in the network and accounted for by altering the scatter-connect procedure in the TLM algorithm as in [95]

$$_{n+1}V_m^i(p,q,r) = \rho_n V_m^r(p,q,r) \tag{2.132}$$

where ρ is the reflection coefficient of the boundaries with values ranging from -1 to +1 (i.e. $-1 \leq \rho \leq= 1$), n is the iteration counter, m is the node number, and p, q and r are the coordinate indicators.

There are three conventional types of boundaries that could be used in the TLM: the open-circuit boundary, the short-circuit boundary and the matched boundary. In a shunt-connected 2D TLM in which the voltage simulates an electric field, a short and open-circuit boundary simulates an electric wall and a magnetic wall respectively. They are perfect reflecting walls of either zero impedance (electric wall) or infinite impedance (magnetic wall). In an open-circuit boundary, the pulse is reflected back into the physical problem with a reflection coefficient of 1. It is normally referred to as a perfect magnetic wall. The concept is such that pulses arriving at the boundary are reflected back in phase and with equal magnitude. In a short-circuit boundary, a reflection coefficient of -1 is simulated. The short-circuit boundary can be inserted at the node or between nodes. In a matched boundary, the pulse is reflected back by the reflection coefficient

$$\Gamma = \frac{Z_s - Z_l}{Z_s + Z_l} \tag{2.133}$$

where Z_s is the surface impedance of the boundary and Z_l is the characteristic impedance of the mesh line.

For antenna and unbounded field problems, modelling of the free space boundaries in an accurate way is very important in order to maintain result accuracy while maximising the simulation time and memory storage [96]. In these cases, Absorbing (or Artificial) Boundary Condition (ABC) [97]–[99] or Perfectly Matched Layers (PML) [86], [100], [101] are employed. PML is a non-physical absorber created adjacent to the outer boundary nodes, with impedance that is non-related to the angle of incidence and the frequency of the outgoing waves [102].

Conventionally, boundaries are implemented halfway between two nodes in order to maintain the synchronism in the mesh [16], [103]. Therefore, the pulse gets to the boundary at half time-step ($2.5\Delta t$) and returns to the node at the end of the time-step. However, TLM has the ability to accommodate various boundary conditions [104] and there has been several novel approaches to boundary placements in TLM. A new approach to boundary implementation was presented by Chen et al. [105], where the boundary was placed across the nodes instead of halfway between them. This arrangement is made in such a way that the boundary wall coincides with a row of nodes thereby removing the need for the mesh parameter Δl to be the integer fraction of the structure dimension, a required condition when the boundary is halfway between nodes. The new boundary procedure is purely numerical, unlike the conventional method. It is performed at discrete node locations along the boundary. German [106] presented infinitesimally adjustable boundaries in symmetrical node TLM simulation. Muller [107] introduced the technique of arbitrary boundary positioning in the TLM network using a recursive algorithm which replaces the boundary reflection coefficient while leaving the impulse scattering matrix intact. Porter and Dawson suggested the use of asymmetric boundary to avoid distortion of the wave front due to

discontinuity of the plane wave at the boundary [108] and James et al proposed an absorbing boundary for plane wave where pulses are swapped between opposite boundaries [109].

2.5 CONCLUSIONS

TLM is a useful numerical tool in solving electromagnetic (EM) problems. TLM simulations represent models of the electromagnetic wave propagating through a network of discrete transmission lines connected at scattering junctions. In this Chapter, the fundamentals of TLM scheme including a brief history of TLM and an introduction to the analogies of TLM to Maxwell's equations in rectangular coordinate have been discussed. The rigorous derivations of the rectangular TLM parameters and the formulations of TLM algorithm for both 2D and 3D electric waves are also presented. Common terminologies used in TLM are defined in this Chapter and the concepts of stub application and boundaries application are also discussed.

This Chapter will serve as the foundation on which other aspects of this thesis are built. An electromagnetic solver (TLS), based on the discussed TLM algorithm, was developed using MATLAB. To test the effectiveness of the TLS, a set of canonical problems were solved by the code. The details of these models and the simulated results are discussed in Chapter 3.

CHAPTER 3

VALIDATION OF THE RECTANGULAR TLM METHOD FOR CUBOID AND CYLINDRICAL MICROWAVE CAVITIES

In this Chapter, rectangular meshes are used to validate the 3D TLM method in the context of microwave cavities serving as benchmark for the model. A brief introduction to microwave cavities is presented in this Section and equations discussed in here for analytical calculation of the cavity resonant frequencies will be useful as basis for comparison of simulated results in Section 3.2.

3.1 MICROWAVE CAVITIES

Microwave cavities are waveguides (a form of transmission line) made out of hollow metallic structures with a closed fixed cross-sectioned area within which a guided wave propagates. An example of such a structure is shown in Fig. 3.1. These cavities can be filled with materials of various permittivity, ε and permeability, μ properties depending on the required application. In a microwave cavity, waves reflect back at the wall boundaries forming standing waves. These standing waves form modes that are either transverse magnetic (TM) or transverse electric (TE) in the cavity and each of these modes have distinct operating frequencies, from which they begin to propagate, commonly referred to as its cut-off frequency, f_c. At this

frequency, the mode characteristics of the cavities are determined by the cross-section of the waveguide and the type of material in it.

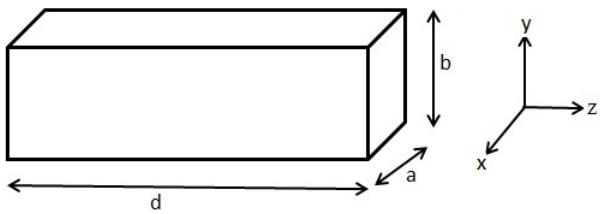

Fig. 3.1: The rectangular cavity.

The cut-off frequency of rectangular microwave cavity is analytically calculated as [110], [111]:

$$f_{mnl} = \frac{1}{2\sqrt{\mu\varepsilon}}\sqrt{\left(\frac{m}{a}\right)^2 + \left(\frac{n}{b}\right)^2 + \left(\frac{l}{d}\right)^2} \tag{3.1}$$

where a, b and d are the dimension of the cavity in the x, y and z direction respectively; m, n, and l represent the cavity mode signifying the number of variations in the standing wave pattern in the x, y, and z direction; $\varepsilon = \varepsilon_r\varepsilon_0$ is the absolute permittivity of the medium of propagation; $\mu = \mu_r\mu_0$ is the absolute permeability of the medium of propagation; ε_r and μ_r are the relative permittivity and relative permeability of the material content of the cavity respectively; ε_0 and μ_0 are the permittivity and permeability of free space.

For propagation in free space, ε_r = 1 and μ_r = 1. Substituting ε_r, μ_r = 1 in (3.1) reduced the equation to:

$$f_{mnl} = \frac{c}{2}\sqrt{\left(\frac{m}{a}\right)^2 + \left(\frac{n}{b}\right)^2 + \left(\frac{l}{d}\right)^2} \tag{3.2}$$

where $c = \frac{1}{\sqrt{\varepsilon_0 \mu_0}}$ is the velocity of propagation in free space; ε_0 is the relative permittivity of free space; and μ_0 is the relative permeability of free space.

If the transmission line is assumed to be infinitely long, the length (d) is assumed to tend to infinity $(d \to \infty)$ and so can be ignored in the calculation. This assumption reduces the problem to a 2D form and (3.2) can be further simplified to (3.3). The same assumption applies when variation in z-direction is not required in a 3D structure.

$$f_{mn} = \frac{c}{2}\sqrt{\left(\frac{m}{a}\right)^2 + \left(\frac{n}{b}\right)^2} \tag{3.3}$$

The resonant frequency of cylindrical cavity resonator is given as [110]:

$$f_{nml} = \frac{1}{2\pi\sqrt{\mu\varepsilon}}\sqrt{\left(\frac{P_{nm}}{r}\right)^2 + \left(\frac{l\pi}{d}\right)^2} \tag{3.4}$$

where μ is the absolute permittivity; ε is the absolute permeability; d is the height of the cylindrical cavity resonator and the indices n, m, l describe the mode. m refers to the number of full-period variations of the field along the circumferential direction, n is the number of half-period variations of the field in the radial direction and l is the number of half-period variations in

z-direction and Pnm are roots of the Bessel functions given in Table 3.1 [110], [111]:

Table 3.1: Roots of the Bessel function

n	P_{n1}	P_{n2}	P_{n3}
0	2.405	5.520	8.654
1	3.832	7.016	10.174
2	5.135	8.417	11.620

The fundamental equations discussed in Section 3.1 will be used to analytically calculate the expected results for cavity simulations in Sections 3.2 and 3.3.

3.2 SIMULATION OF THE RECTANGULAR MICROWAVE CAVITY RESONATOR USING RECTANGULAR TLM METHOD

In this Section, rectangular microwave cavities are simulated using the developed TLS solver. The TLM methods employed are the shunt 2D TLM node and the SCN TLM operated in 2D mode. The simulated resonant cavity has an arbitrary cross-sectional area of 100 mm x 100 mm. The cut-off frequencies for possible modes in this cavity are calculated using (3.3), where a = 100 mm and b = 100 mm. The structure was meshed and excited by an impulse of 1V applied at the centre of the mesh and the output was taken as the vertical component of the electric field (Ez) at the point of excitation. The Discrete Fourier Transform (DFT) was employed to convert the obtained time-domain results to their frequency-domain forms [44].

Generally, the choice of the discrete length (Δl) of the nodes in all direction in the simulation space depends on the highest frequency of interest. It is recommended that $\lambda > 10\Delta l$ in order to minimise dispersion error [32]. Therefore, the dispersion cut-off frequency for the modelled square cavity is calculated as:

$$f_{c_{tlm}} = \frac{v_{tlm}}{\lambda_m} \tag{3.5}$$

where v_{tlm} is the velocity of wave in TLM and λ_m is the modelled wavelength in meters.

The cavity is filled with air, which means $v_{tlm} = c \cong 3 \times 10^8\ ms^{-1}$. At 10 nodes per wavelength, for a cavity of 100 mm:

$$f_{c_{tlm}} = \frac{3 \times 10^8}{0.1} = 3GHz \tag{3.6}$$

The dispersion cut-off frequency is 3 GHz at this level of discretisation, which means that any results beyond this frequency are prone to high dispersion error. In order to accommodate more modes within the dispersion cut-off limit of the modelled cavities, the mesh used for this simulation is 21 nodes per λ. The dispersion cut-off frequency then becomes 6.25 GHz.

3.2.1 SIMULATION OF RECTANGULAR CAVITY USING 2D SHUNT TLM NODE METHOD

The first model considered in this Section was simulated using the 2D shunt TLM node. The cavity was represented by mesh of 441 nodes. Nodes at the edges of the cavity were terminated by an electric wall ($\Gamma = -1$) in all dimensions. The mesh was excited by an impulse voltage of 1V at node (11,11,1) and the electric field simulated was observed at the same node where the mesh was excited. The simulation was done with 4096 time steps/iterations. The normalised electric field simulated by TLS is as shown in Fig. 3.2. The distribution of the TM110 mode in the simulated cavity at 2.121 GHz after 4096 iterations is shown in Fig. 3.3. The results are normalised to the highest electric field magnitude in the simulation. A similar cavity was simulated using the CST Microstripes solver, which uses 3D TLM method, for validation purposes. Results for both simulations are compared in Table 3.2.

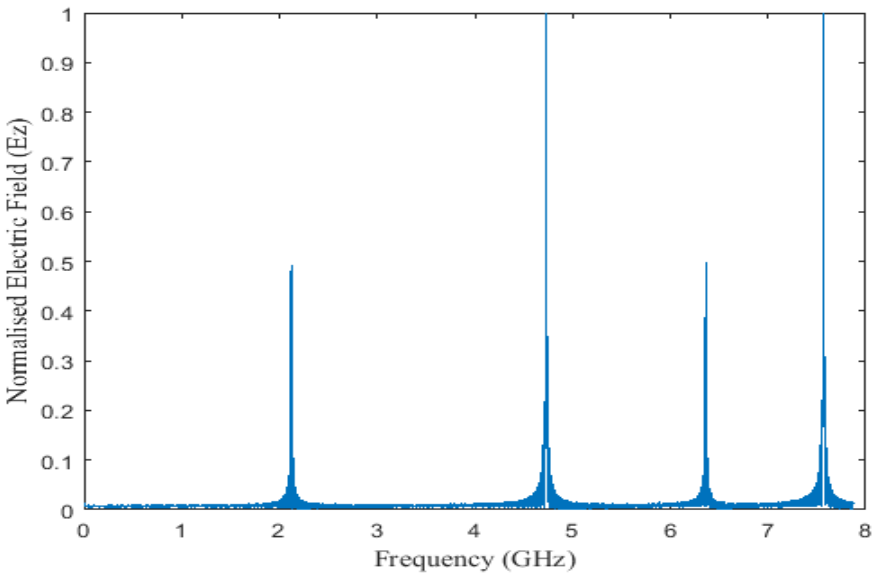

Fig. 3.2: The normalised simulated resonant frequency for a 100 mm x 100 mm cavity modelled with a shunt 2D TLM after 4096 iterations.

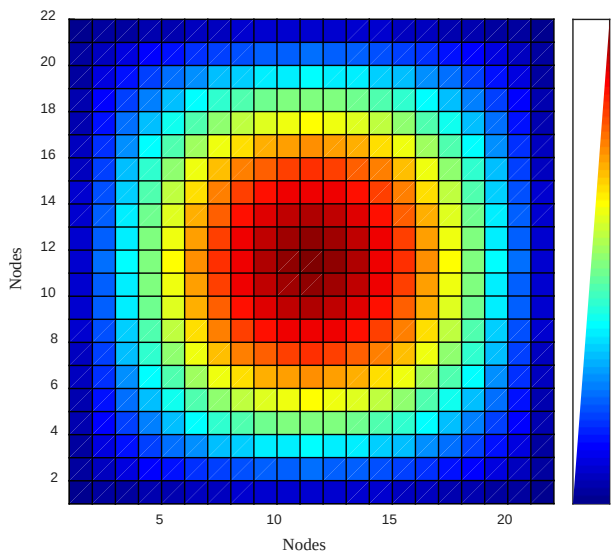

Fig. 3.3: The normalised simulated electric field distribution of the TM110 mode for a 100 mm x 100 mm cavity modelled with 2D shunt TLM (2.121 GHz) after 4096 iterations.

Table 3.2: Comparison of the analytically generated resonant frequencies to the simulated using shunt 2D TLM and CST

Modes	Analytical Results (GHz)	Simulated Results	
		Shunt 2D TLM (GHz)	CST (GHz)
TM110	2.120	2.121	2.120
TM220	4.243	Not excited	Not excited
TM330	6.364	6.364	6.355
TM440	8.485	7.568	7.642

The normalised electric field simulated by the shunt node of the TLS compared well with the analytical results and the mode distribution pattern in the simulated cavity was also as expected from theory. The simulated results using the TLS solver also agreed with the simulated results from the CST. These results show that the TLS solver has been correctly implemented and the level of accuracy obtained in the simulated result shows the effectiveness of the solver in modelling the cavity.

However, it was observed that TM220 was not excited. A resonance theoretically not expected occurred at 4.74 GHz as shown in Fig. 3.2. Since the method and position of excitation affects the type of modes excited in a cavity, the position or type of excitation used in this simulation could be responsible for the absence of TM220 and the excitation of the other mode at 4.74 GHz that was not initially predicted for the cavity simulated cavity type. This occurrence of a mode at 4.74 GHz resonance was common to both the shunt node and the CST simulations.

Checking the effect of dispersion on the simulated results, it was observed that results are not significantly affected by dispersion error up to the calculated 6.25 GHz TLM dispersion cut-off frequency for the cavity at 21 nodes per λ. As can be seen in Table 3.2 the results of both the TLS solver and CST compared well with the analytical results up to 6.364 GHz, slightly higher than the calculated dispersion cut-off frequency. The disparity in the simulated results above 6.364 GHz in comparison to the analytical results can therefore be accounted for by the numerical dispersion effect of TLM. This effect can be clearly seen on the results of the TM440 mode of the cavity, which falls in the frequency range higher than the 10 $nodes/\lambda$ limit. Therefore, it is very important that any result beyond the dispersion cut-off frequency be treated with caution because of the dispersion error.

3.2.2 SIMULATION OF RECTANGULAR CAVITY USING THE SYMMETRICAL CONDENSED NODE (SCN) TLM

In the Section 3.1.1, a cavity of arbitrary dimension 100 mm x 100 mm was simulated using the shunt 2D TLM nodes of the TLS solver and the simulated results were compared with the analytical results and the results obtained from CST. Here in this Section, the same cavity is modelled using the SCN nodes of the TLS solver in order to compare the output of the two simulated results produced by the two methods.

In the SCN model of the cavity, the *z*-axis cavity was modelled by one node and electric boundary applied on the faces of the node since variation of the electric field along the cylinder height (*z*-direction) is not required. Electric boundaries were applied on other edges of the cavity as well. The cavity was excited at node (11, 11, 1) of the 21 x 21 x 1 mesh with an impulse voltage of 1V and the field was observed at the same node where the cavity was excited. The simulated resonant frequency is shown in Fig. 3.4. All

results are normalised to the highest electric field (E_z) magnitude in the simulations.

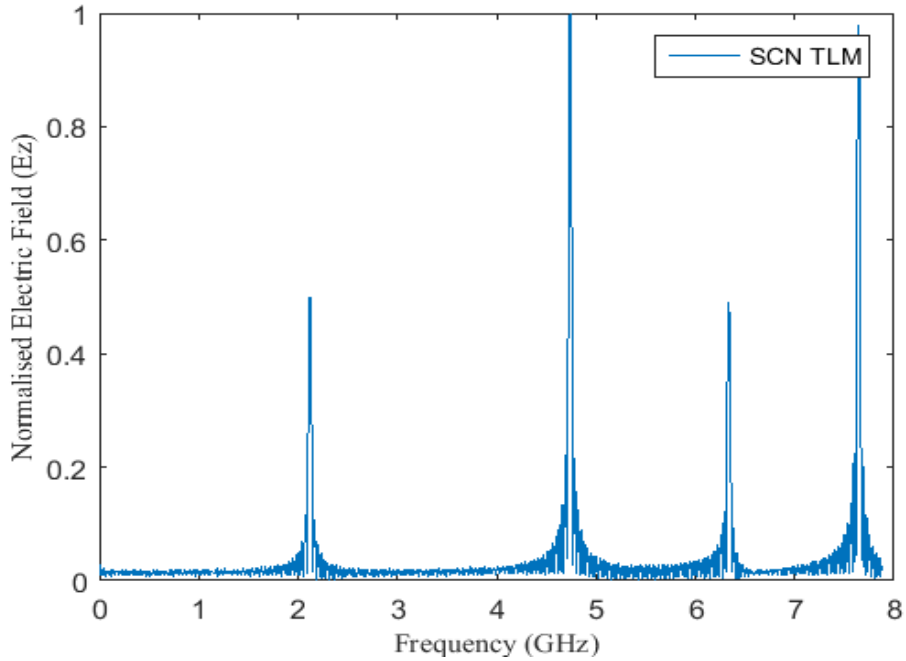

Fig. 3.4: The normalised simulated resonant frequency for a 100 mm x 100 mm cavity modelled with SCN TLM.

Apart from the occurrence of a resonance at 4.74 GHz and suppression of mode TM220, the agreement of all the simulated results within the dispersion limit compared with the analytical expectations is accurate with less than 0.1% error as shown in Table 3.3. As in the shunt model, the effect of dispersion error is more significant in the resonant frequency of TM440 because its value is above the acceptable dispersion cut-off frequency of the simulated cavity. The electric field distributions for the first three modes are shown in Table 3.4.

Table 3.3: Simulated resonant frequencies using the analytic, the shunt TLM, SCN TLM and CST methods

Modes	Analytical Results (GHz)	Simulated Results	
		SCN TLM (GHz)	CST (GHz)
TM110	2.120	2.121	2.120
TM 220	4.243	-	-
TM 330	6.364	6.360	6.355
TM 440	8.485	7.649	7.642

Table 3.4: Normalised simulated electric field distributions for a 100 mm x 100 mm cavity modelled with SCN TLM after 8192 iterations.

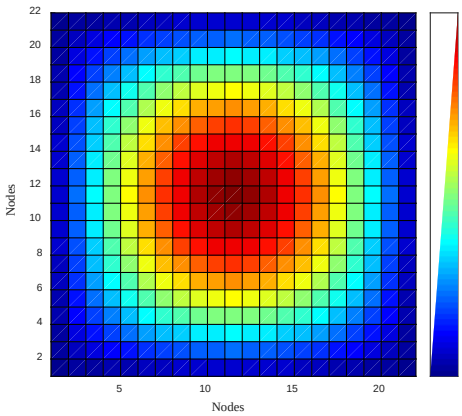	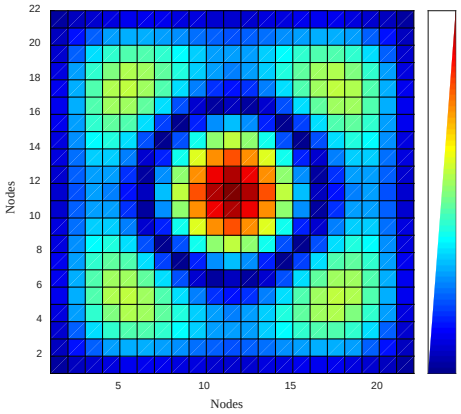
Mode 1 (TM110) at 2.12 GHz	Mode 2 at 4.74 GHz
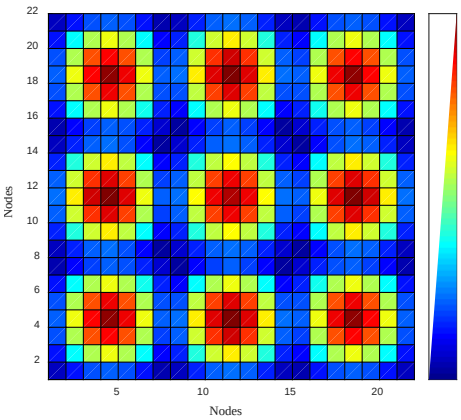	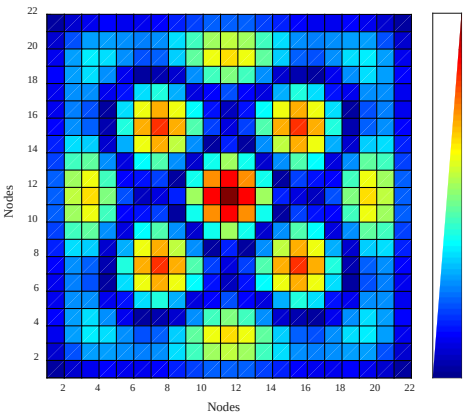
Mode 3 (TM330) at 6.36 GHz	Mode 4 (TM440) at 7.649 GHz

3.2.3 Comparing the Shunt 2D TLM and the SCN TLM

The shunt and the SCN TLM methods have been applied to the modelling of cavity in Section 3.2.1 and 3.2.2 respectively. In this Section a short comparison between the two methods is presented. Considering the effectiveness of the two methods in simulating the rectangular microwave

cavity with respect to the accuracy of the result, it was observed that the two models produced similar results with acceptable levels of accuracy. The small difference between the results for these two methods occurred outside the dispersion cut-off frequency limit as shown in Fig. 3.5. The implementation of 2D Shunt is simpler as fewer variables are required in the simulation compared to the SCN as discussed in Chapter 2.

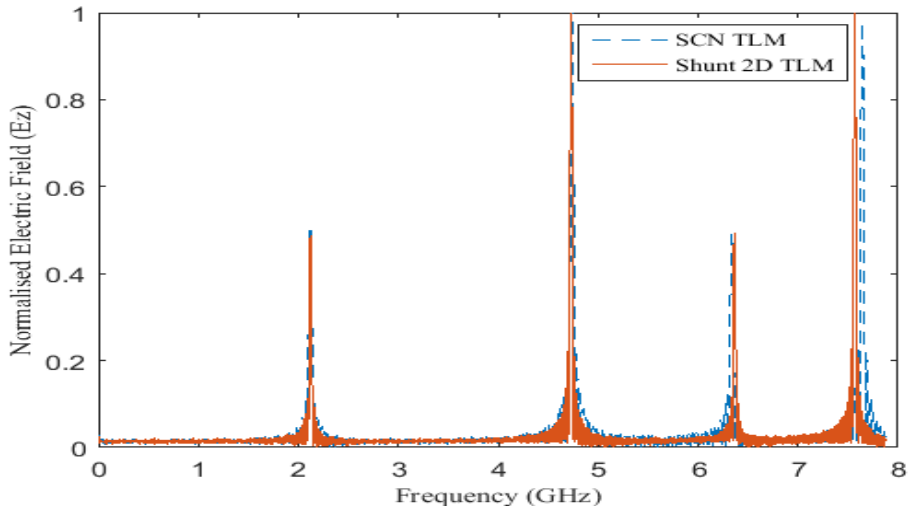

Fig. 3.5: Comparison of the normalised simulated electric fields with resonant frequency for a 100 mm x 100 mm cavity modelled with SCN TLM and shunt TLM.

From Fig. 3.5, TM22 is observed to be suppressed by the two models but another mode was excited at 4.74 GHz. A common node (11,11,1) was chosen for the excitation of the two meshes and it could be deduced that some of the expected modes were not excited or were suppressed, as is the case with TM220, due to the position or type of excitation rather than the particular method used. The excitation of another mode, that was not initially planned for, as in the case at the 4.74 GHz frequency, was also common to both methods.

The choice between the two methods thus depends on the problem being considered and the level of simplicity required. However, although the resonant frequency of the cavity is determined by the radius of the cavity and not by its length, a 2D model will only generate modes that have no variations along the cavity height. This implies that in order to get all the possible modes in the cavity, a 3D model is required, which makes the SCN model a preferred option over the 2D shunt TLM. Moreover, characteristics of propagation in two dimensions can be predicted in 3D SCN mesh while only one direction can be achieved per iteration when working with a 2D TLM model [112].

For the rest of this thesis, the focus in reference to the rectangular TLM will be on the SCN method.

3.3 SIMULATION OF THE CIRCULAR MICROWAVE CAVITY RESONATOR USING A RECTANGULAR TLM METHOD

When modelling with rectangular TLM mesh, the surfaces of a curved boundaries or boundaries that are not conforming to the mesh are normally approximated to fit the mesh [41], [113]. The approximated boundaries have a staircase effect at the edge and are referred to as staircase approximations. According to Sewell et al. [7], the staircase approximation to curved boundaries results in the misrepresentation of the area of geometry in question and this poses several problems in the results of the model. For example, staircase approximations in modelling of circular resonators produce an irregular boundary creating spurious resonances and shifts of resonant frequencies from the expected values. In this Section, a cylindrical cavity is simulated using the rectangular TLM to verify this staircase error and lay a foundation for the work done in the Sections that follow.

The resonant frequencies excited in a cavity depend on the dimensions and the material contained in the cavity. In this example, the radius, r of the simulated circular cavity was 50 mm and the height was 100 mm as shown in Fig. 3.6. The cavity content was air, that is ε_r = 1 and μ_r= 1.

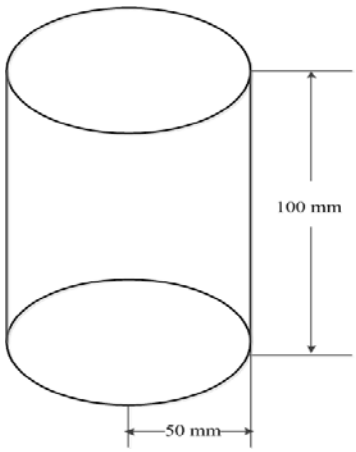

Fig. 3.6: The simulated air-filled cavity.

Since the simulated cavity is cylindrical in shape, the principle of cylindrical cavity resonator was used in calculating the resonant frequency. The resonant frequency was calculated using equation (3.4). In the TLS solver, the cross section of the cavity was mapped onto 21x21x1 nodes and a short circuit boundary was inserted at the nodes nearest to the perimeter of the cylinder. The variation in the *z*-direction was not considered, therefore, the simulation is conducted as a 2D model on the *x*-*y* plane only. The normalised electric field generated for the cavity after 4096 time steps are shown in Fig. 3.7. Fig. 3.8 shows the field distribution simulated for mode TM110 of the cavity at the 2.21 GHz resonant frequency.

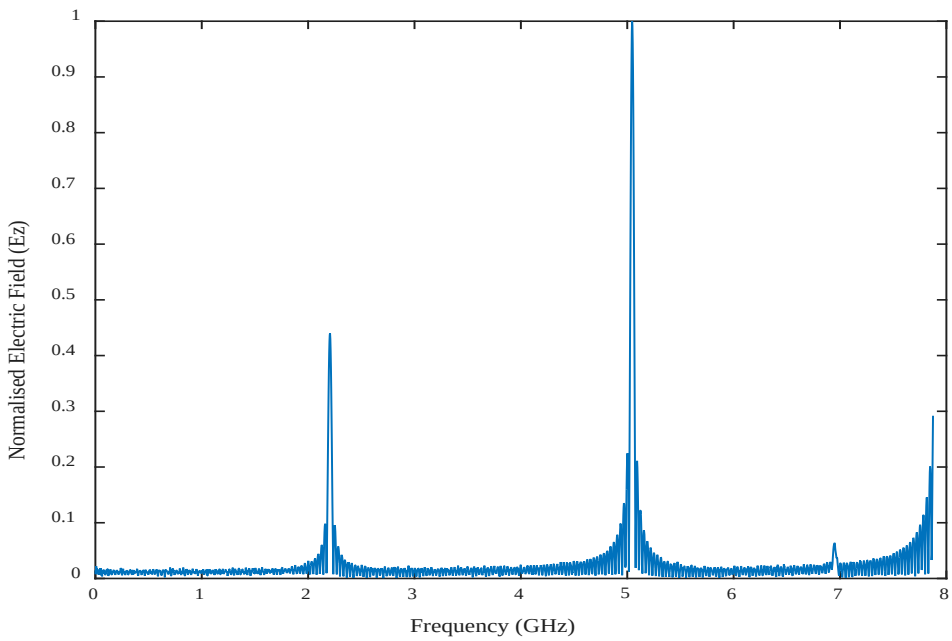

Fig. 3.7: The normalised simulated resonant frequency for a 50 mm radius circular cavity modelled with 21x21x1 nodes after 4096 iterations.

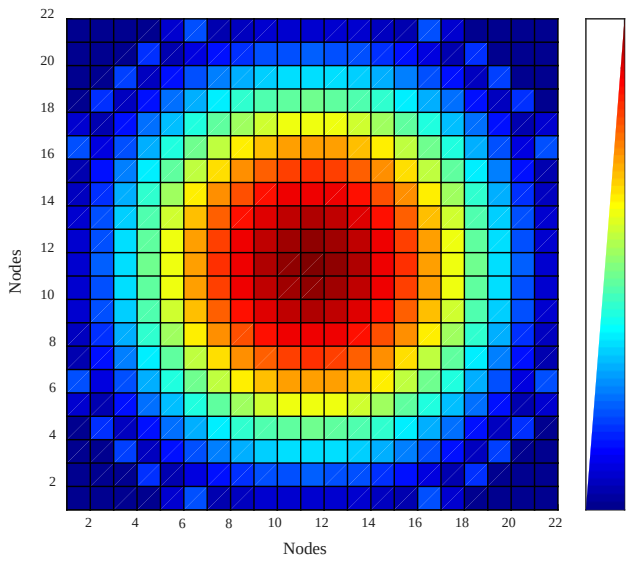

Fig. 3.8: The normalised simulated TM010 mode for a 50 mm radius circular cavity modelled with 21x21x1 SCN nodes at 2.21 GHz after 4096 iterations.

The simulated resonant frequencies are compared with the analytically generated results in Table 3.5 and it is accurate to an approximately 3% error. There is a shift in the simulated resonant frequencies, which makes it lower for TM010 and higher for TM030 compared to the analytical expectations and this makes it difficult to associate the resonance to theoretically expected corresponding mode for the modelled cavity.

Table 3.5: The modes in the simulated circular cavity using rectangular TLM are:

Modes	Analytical Results (GHz)	Simulated Results (GHz)
TM010	2.295	2.209
TM030	4.900	5.050

Another problem with the staircase approximation is the possibility of spurious modes occurring. The two simulated resonances were placed beside their closest possible analytical value in Table 3.5 but any of the two simulated frequencies may well be mere spurious modes as a result of irregularities in the boundary placement. Spurious modes do occur in the TLM model as in most numerical methods [114] but they occur at high frequencies that are well beyond the cut-off frequency of the TLM mesh ($\Delta l \approx \lambda/10$). The problem with spurious modes, however, is that they propagate with intense dispersion as a result of their high resonant frequencies and sometimes they have relatively high magnitudes and propagate without attenuation through the cavity. They are generated by physical or temporal discontinuities in the modelled structure/system [115]. The way around these spurious modes is to either avoid spatial discontinuities or to process the excitation signal using a low-pass or band limiting filter [116]. Since the spatial discontinuity cannot be avoided in the staircase approximated boundary, spurious mode can be reduced by applying a finer mesh [13].

The effect of the mesh's grading on the simulated results obtained for the modelled cavity was examined by comparing the simulated results for different mesh grades. Regrading the mesh affected Δt and consequently the number of iterations had to be modified accordingly in order to compare the variations in the mesh accurately. The requirement for greater time for pulses in the finer mesh to attain steady state was taken into account. The time required for each mesh size to attain steady state was calculated separately. The discrete time step and the number of iterations for the first simulation were set as Δt_1 and N_1 respectively. Number of time steps required for subsequent mesh operations, N_i was then obtained using (3.5) [72].

$$N_i = \frac{N_1 \Delta t_1}{\Delta t_i} \tag{3.7}$$

where Δt_i is the discrete time step for the new mesh and i= 1, 2, 3 ….n. n is the last mesh considered, which in this case is 5.

The simulated resonant frequencies for different mesh sizes and the calculated number of iterations used for each simulation are as shown in Table 3.6. The mode distributions for 3 different mesh sizes are shown in Table 3.7.

Table 3.6: Comparison of the results for different discretization mesh sizes

i	Number of nodes	Number of iterations, N_i	Frequency (GHz)
1	121 (11 × 11 nodes)	4096	2.151
2	225 (15 × 15 nodes)	5586	2.190
3	441 (21 × 21 nodes)	7820	2.205
4	1225 (35 × 35 nodes)	11543	2.234
5	2601 (51 × 51 nodes)	18991	2.247
Analytic = 2.295 GHz			

In this example, a finer mesh has been applied to every part of the modelled structure to achieve better results. The results show that the finer the mesh, the closer the results to the analytical expectations. With finer mesh, the staircase approximation edge improved in its adjustment to the curved boundary of the circular cavity and the field distribution becomes smoother around the approximated edge of the cavity. The progressive improvement in the accuracy of the simulated result, compared to the analytical result,

with increasing mesh size is shown in Fig. 3.9. This accuracy, however, comes at the expense of storage space and simulation time.

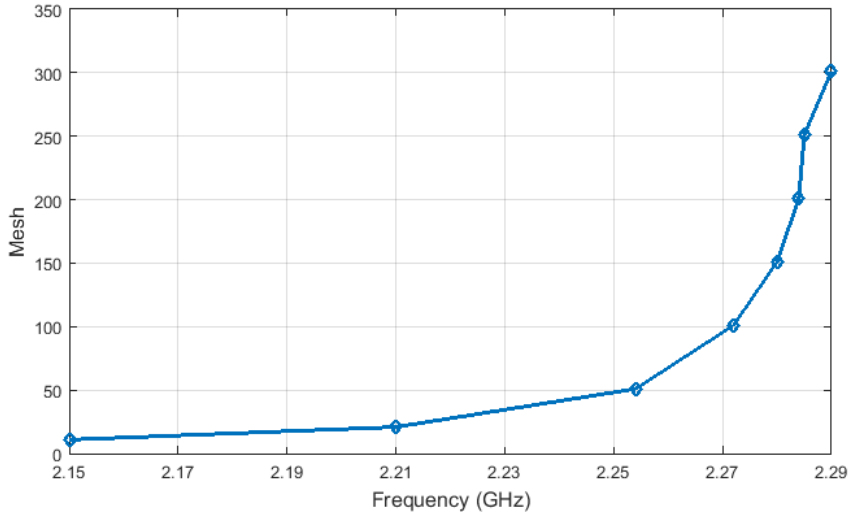

Fig. 3.9: Effect of using finer rectangular mesh for cylindrical cavity simulation with N mesh indicating $N \times N$ nodes.

Conventionally, geometrical conformity is catered for by the use of graded mesh, such that a finer mesh is used around the curved walls of the structure/object in comparison with the non-curved parts of the object being modelled [70]. Graded mesh uses less storage space. Another approach well known is the mesh adaptation method where a mesh that can fit the boundary more accurately, such as triangular and tetrahedral meshes, are applied around the curved walls [14], [15]. Al Mukhtar and Sitch [16] were the first to develop the polar meshes for a lossless TLM model with axial symmetry, which paved the way for further research into curvilinear mesh development [16]–[19], [71]. The use of curvilinear meshes such as cylindrical TLM in which curved meshes are used instead of a linear mesh allow for closer conformity of the mesh structure to the original modelled object. The procedure used in developing the cylindrical TLM part of the TLS and results of simulation examples are presented in Chapter 4.

Table 3.7: The normalised simulated TM010 mode for a 50 mm radius circular cavity modelled using SCN TLM

Modes	Frequency GHz)	Electric field distribution in the simulated cavity
11x11 Nodes	2.15	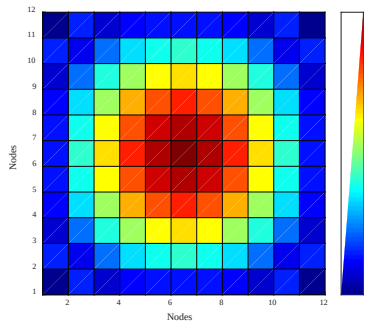
21x21 Nodes	2.21	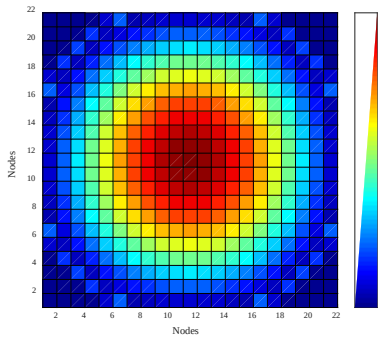
51x51 Nodes	2.25	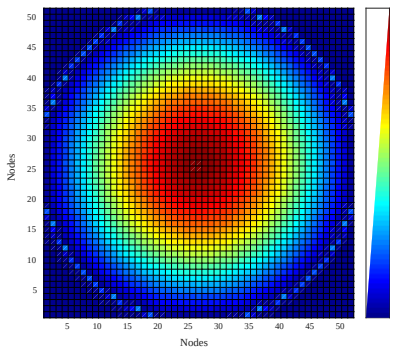
The analytical frequency = 2.29 GHz		

3.4 CONCLUSIONS

This Chapter is focused on the simulations of canonical problems with known theoretical solutions with the intention to validate the rectangular part of the solver developed for this thesis based on the TLM algorithm. The theoretical background of the rectangular TLM mesh and the algorithm procedures used in developing the TLS were discussed in Chapter 2. The report of electromagnetic simulation of some canonical problems using 2D and 3D was presented. The presented results proved that the solver is capable of simulating practical EM problems. The simulation results generated by the TLS for 2D and the 3D TLM are compared to that of the analytical results for validation purpose. The simulated results of the TLS were also compared with the simulated results of an existing modelling tool, CST, for the validation of the newly developed solver.

The effect of stair-cased approximation on curved boundaries when modelling with rectangular TLM mesh is highlighted. It was observed that the results obtained when the rectangular mesh was applied to model the circular cavity are less accurate compared to the analytical results. The application of finer mesh improved the results but the error was still present and the improvement in the accuracy of the obtained results was achieved by sacrificing time and computation resources. Since accuracy is very essential when it comes to modelling of axisymmetric radiating structures, the use of cylindrical TLM mesh in the place of rectangular mesh is investigated in Chapter 4.

CHAPTER 4

DEVELOPMENT OF CYLINDRICAL TRANSMISSION LINE SOLVER

In Chapter 2, an electromagnetic (EM) solver (TLS) was developed based on the TLM method. The solver includes both the rectangular and the cylindrical mesh. The theoretical background of rectangular TLM and its algorithm have been discussed in Chapter 2. The simulation results for cuboid and cylindrical microwave cavities modelled using TLS' rectangular TLM mesh were also presented. The aim of this Chapter is to create a bridge in the gap between the theoretical foundations of cylindrical TLM and its applications. The focus is to theoretically establish the cylindrical TLM node scheme by presenting its analogies to Maxwell's equations and explaining its implementation algorithm. Simulation results of modelled examples will also be presented to evaluate the effectiveness of the cylindrical TLM mesh EM problems with curved edges and to validate the accurate implementation of the mesh in TLS.

When modelling with a rectangular TLM, curved boundaries are approximated to fit the object and this approximation results in a staircase finish along the curved edges as discussed in Chapter 3. Results of the circular cavity simulated using the rectangular mesh showed a high level of error when compared with the analytic solutions. Curvilinear mesh methods [16]–[19], [71], such as cylindrical TLM, have curved link lines that can be fitted better with curved surfaces.

However, there have been underlying challenges in implementing the cylindrical TLM, making it less popular than its rectangular counterpart despite its better efficiency in dealing with curved boundaries. The foremost of these challenges is that there are very few publications on the use of the cylindrical TLM mesh and rigorous analysis of the fundamental relationship of the cylindrical TLM model to Maxwell's equations is not available in the literature. This Chapter aims to bridge this gap by presenting a rigorous analysis of the relationship between the cylindrical TLM and Maxwell's equations.

4.1 THEORY OF CYLINDRICAL TLM MESH

In this Section, the theory of cylindrical TLM will be presented. Maxwell's equations in cylindrical form, their analogies to the cylindrical TLM nodes parameters and how synchronism is achieved in cylindrical TLM will be described.

4.1.1 MAXWELL'S EQUATIONS IN CYLINDRICAL FORM

The relationship of Maxwell's equations to the cylindrical TLM model is similar to that of rectangular TLM except for the difference in geometry. Maxwell's equations have already been given in Section 2.3.1 of Chapter 2. As with rectangular coordinates, Maxwell's equations can be expressed in cylindrical coordinates. To achieve this, the components x, y, z have to be replaced by r, θ, z. For example, a point in the cylindrical coordinate can be expressed as in Fig. 4.1. Components r, θ, z are the radial, circumferential and axial components of the cylindrical coordinate system respectively.

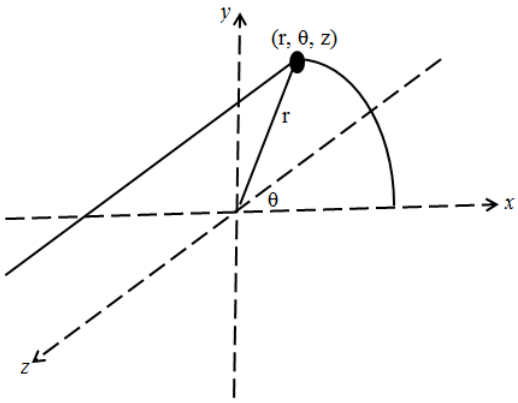

Fig. 4.1: Cylindrical coordinates.

In cylindrical coordinates, Maxwell's curl equations (2.1) can be expressed as in (4.1) - (4.3), (2.2) as (4.4) - (4.6), (2.3) as (4.7) and (2.4) as (4.8).

$$\frac{\partial H_z}{r\partial\theta} - \frac{\partial H_\theta}{\partial z} = J_r + \frac{\partial D_r}{\partial t} \tag{4.1}$$

$$\frac{\partial H_r}{\partial z} - \frac{\partial H_z}{\partial r} = J_\theta + \frac{\partial D_\theta}{\partial t} \tag{4.2}$$

$$\frac{\partial H_\theta}{\partial r} - \frac{\partial H_r}{r\partial\theta} = J_z + \frac{\partial D_z}{\partial t} \tag{4.3}$$

$$\frac{\partial E_z}{r\partial\theta} - \frac{\partial E_\theta}{\partial z} = -\frac{\partial B_r}{\partial t} \tag{4.4}$$

$$\frac{\partial E_r}{\partial z} - \frac{\partial E_z}{\partial r} = -\frac{\partial B_\theta}{\partial t} \tag{4.5}$$

$$\frac{\partial E_\theta}{\partial r} - \frac{\partial E_r}{r\partial\theta} = -\frac{\partial B_z}{\partial t} \tag{4.6}$$

$$\frac{\partial E_r}{\partial r} + \frac{\partial E_\theta}{r\partial\theta} + \frac{\partial E_z}{\partial z} = \rho \tag{4.7}$$

$$\frac{\partial H_r}{\partial r} + \frac{\partial H_\theta}{r\partial\theta} + \frac{\partial H_z}{\partial z} = 0 \tag{4.8}$$

As in the rectangular node, the cylindrical node is broken into series and shunt parts for clarity. In the series part, the electric fields, E_r, E_θ and the magnetic field, H_z are the non-zero fields and Maxwell's equations in cylindrical form reduce to (4.9) – (4.11) using $D = \varepsilon E$

$$\frac{\partial H_z}{r\partial\theta} = \varepsilon\frac{\partial E_r}{\partial t} \tag{4.9}$$

$$-\frac{\partial H_z}{\partial r} = \varepsilon\frac{\partial E_\theta}{\partial t} \tag{4.10}$$

$$\frac{\partial E_\theta}{\partial r} - \frac{\partial E_r}{r\partial\theta} = -\mu\frac{\partial H_z}{\partial t} \tag{4.11}$$

Subtracting the differential (4.9) with respect to θ and that of (4.10) with respect to r gives (4.12). Inserting (4.11) into (4.12) results in the wave equation as given in (4.13)

$$\frac{\partial^2 H_z}{r^2\partial\theta^2} + \frac{\partial^2 H_z}{\partial r^2} = -\varepsilon\frac{\partial}{\partial t}\left(\frac{-\partial E_r}{r\partial\theta} + \frac{\partial E_\theta}{\partial r}\right) \tag{4.12}$$

$$\frac{\partial^2 H_z}{r^2\partial\theta^2} + \frac{\partial^2 H_z}{\partial r^2} = \varepsilon\mu\frac{\partial^2 H_z}{\partial t^2} \tag{4.13}$$

In the shunt part, magnetic fields H_r, H_θ and the electric field, E_z are the non-zero fields and Maxwell's equations in cylindrical form reduce to (4.14) - (4.16)

$$\frac{\partial E_z}{r\partial\theta} = -\mu\frac{\partial H_r}{\partial t} \tag{4.14}$$

$$-\frac{\partial E_z}{\partial r} = -\mu\frac{\partial H_\theta}{\partial t} \tag{4.15}$$

$$\frac{\partial H_\theta}{\partial r} - \frac{\partial H_r}{r\partial\theta} = \varepsilon\frac{\partial E_z}{\partial t} \tag{4.16}$$

Following the same procedure as in the series part, by differentiating (4.14) with respect to θ and (4.15) with respect to r and combining the results gives

$$\frac{\partial^2 E_z}{\partial r^2} + \frac{\partial^2 E_z}{r^2\partial\theta^2} = -\mu\left(\frac{\partial^2 H_\theta}{\partial t\partial r} + \frac{\partial^2 H_r}{r\partial t\partial\theta}\right) \tag{4.17}$$

Inserting equation (4.16) into (4.17) gives another wave equation:

$$\frac{\partial^2 E_z}{\partial r^2} + \frac{\partial^2 E_z}{r^2\partial\theta^2} = \mu\varepsilon\frac{\partial^2 E_z}{\partial t^2} \tag{4.18}$$

The two wave equations, (4.13) and (4.18), describe the behaviour of an EM wave in a lossy medium.

4.1.2 ANALOGIES OF MAXWELL'S EQUATIONS TO CYLINDRICAL TLM

To understand the analogy between the E and H fields and the electric circuit parameters modelled by the TLM, a section of a long transmission line is considered as shown in .4.2. As the discrete length, $\partial l \rightarrow 0$, the infinitesimal sign ∂ is replaced by Δ, which is a finite value for numerical solution and the voltage and current of the circuit can be deduced using Kirchhoff's laws as:

$$-\frac{dv}{dr}\Delta l = L\frac{di}{dt}$$
$$-\frac{di}{dr}\Delta l = C\frac{dv}{dt} + \frac{V}{R} \tag{4.19}$$

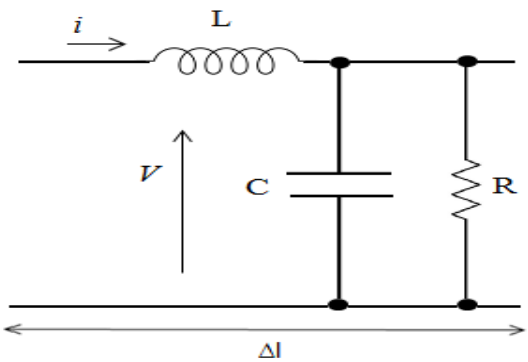

Fig. 4.2: Electrical components of a transmission line.

If the same steps followed in obtaining (4.13) and (4.18) are repeated, similar equations in circuit form are obtained in terms of current and voltage. By comparing the circuit equations obtained from the Kirchhoff's laws for a discrete transmission line with the wave equations, an analogy between the two can be deduced.

As mentioned in Chapter 2, the basic building block for the TLM algorithm is the 2D model in shunt and the series configurations. To simplify the

analysis, the 3D cylindrical TLM node can be broken into series and shunt 2D nodes. In a series model, two transmission lines are connected in such a way that the current flows through two inductors, 2*L* and across one capacitor, *C*. The current equations for the inductors and across the capacitor are given by:

$$\frac{\Delta E_r}{r\partial\theta} - \frac{\Delta E_\theta}{\partial r} = 2L\frac{\partial I}{\partial t} \tag{4.20}$$

$$\frac{\partial I}{\partial r} = C\Delta r\frac{\partial V}{\partial t} \tag{4.21}$$

The resistor *R* is not considered in this equation because it is normally modelled as a lossy stub in the TLM node (see details in Chapter 2, Section 2.2.3).

Assuming the current is flowing in the *z*-direction, the amount of current, I_z that flows in the finite space step, Δz, gives the magnetic field, H_z:

$$H_z = I_z/\Delta z \tag{4.22}$$

Substituting for *I* in (4.20) gives

$$\frac{\Delta E_r}{r\partial\theta} - \frac{\Delta E_\theta}{\partial r} = 2L\frac{\partial H_z}{\partial t} \tag{4.23}$$

The inductance per unit length along *z* can be deduced by comparing (4.23) with (4.11) as:

$$L = \mu \Delta z \tag{4.24}$$

Substituting H_z for I in (4.21) also gives

$$\frac{\partial H_z}{\partial r} = C \frac{\partial E_\theta}{\partial t} \tag{4.25}$$

and by comparing equation (4.25) with (4.10), the capacitance per unit length along z can be deduced as:

$$C = \varepsilon \Delta z \tag{4.26}$$

All the parameters of the medium can be obtained by comparing similar pairs of circuit related equations and wave-related equations as shown below. It is possible to establish a mapping between the components of the magnetic field, H and nodal current, I; components of electric field, E and electric potential, V; permeability, μ and inductance, L and permittivity, ε and capacitance, C.

$$-\frac{\partial H_z}{r\partial \theta} = \varepsilon \frac{\partial E_r}{\partial t} \leftrightarrow \frac{\partial I_z}{\partial z} = -C_r \frac{\partial V_r}{\partial t} \tag{4.27}$$

$$\frac{\partial H_z}{\partial r} = \varepsilon \frac{\partial E_\theta}{\partial t} \leftrightarrow \frac{\partial I_z}{\partial r} = -C_\theta \frac{\partial V_\theta}{\partial t} \tag{4.28}$$

$$\frac{\partial E_\theta}{\partial r} - \frac{\partial E_r}{r\partial \theta} = -\mu \frac{\partial H_z}{\partial t} \leftrightarrow \frac{\partial V_\theta}{\partial r} - \frac{\partial V_r}{rd\theta} = 2L \frac{\partial I_z}{\partial t} \tag{4.29}$$

The circuit equivalent equations for electric fields E_r and E_θ are also given as

$$E_r = -\frac{V_r}{\Delta r}; E_\theta = -\frac{V_\theta}{r\Delta\theta} \tag{4.30}$$

Similarly in the shunt TLM node, the current flows across two capacitors and through one inductor and obtain

$$\frac{\partial E_z}{r\partial\theta} = -\mu\frac{\partial H_r}{\partial t} \leftrightarrow \frac{\partial V_z}{\partial\theta}\Delta r = -L_r\frac{\partial I_r}{\partial t} \tag{4.31}$$

$$-\frac{\partial E_z}{\partial r} = -\mu\frac{\partial H_\theta}{\partial t} \leftrightarrow \frac{\partial V_z}{\partial r} = -L_\theta\frac{\partial I_\theta}{\partial t} \tag{4.32}$$

$$\frac{\partial H_\theta}{\partial r} - \frac{\partial H_r}{r\partial\theta} = \varepsilon\frac{\partial E_z}{\partial t} \leftrightarrow \frac{\partial I_r}{r\partial\theta} + \frac{\partial I_\theta}{\partial r} = -2C\frac{\partial E_z}{\partial t} \tag{4.33}$$

The circuit equivalent for fields components at the shunt node are

$$E_z = -\frac{V_z}{\Delta z}; H_\theta = \frac{I_r}{r\Delta\theta}; H_r = -\frac{I_\theta}{\Delta r} \tag{4.34}$$

It is worthy of note that equations (4.11) and (4.18) are similar to the $\nabla \times E = -\mu\frac{\partial H}{\partial t}$ and $\nabla \times H = \varepsilon\frac{\partial E}{\partial t}$ in rectangular coordinates except for the geometry related parameter $1/r$ in the cylindrical coordinate system. This additional parameter results from the variation in discrete length along the theta dimension outwardly from the centre of the cylinder.

4.1.3 SYNCHRONISM IN CYLINDRICAL TLM NODE

The increase in length on the theta dimension of the cylindrical node described by the additional geometric parameter $1/r$ means that there would be lack of synchronism in the scatter-connect procedure of the node since pulses along the theta dimension has a longer distance to travel before connection at any time Δt. In order to ensure synchronism of pulses between nodes in the cylindrical TLM mesh, the parameter $1/r$ has to be included in the TLM formulations. This is achieved by introducing extra inductance and capacitance in the form of closed and open stubs respectively into the node. For a 3D cylindrical node, there are parameter variations in r, θ and z directions and the total capacitance, C of the node given in (4.26) can be expressed as:

$$C = \begin{bmatrix} C_r \\ C_\theta \\ C_z \end{bmatrix} \tag{4.35}$$

where C_r , C_θ and C_z are the capacitance value for the three dimension $r, \theta,$ and z. The total capacitance modelled by a cylindrical node in a particular direction, for example, is represented by the distributed capacitance of the transmission lines and stub polarised in that direction and it is obtained as [16] :

$$\begin{aligned} C_r &= \varepsilon_r \Delta l_r + C_{or} = C_{zr}\Delta z + C_{\theta r}\Delta T + C_{or} \\ C_\theta &= \varepsilon_\theta \Delta l_\theta + C_{o\theta} = C_{r\theta}\Delta r + C_{z\theta}\Delta z + C_{o\theta} \\ C_z &= \varepsilon_z \Delta l_z + C_{oz} = C_{rz}\Delta r + C_{\theta z}\Delta T + C_{oz} \end{aligned} \tag{4.36}$$

where $\Delta l_r = \frac{\Delta T \Delta z}{\Delta r}$, $\Delta l_\theta = \frac{\Delta r \Delta z}{\Delta T}$ and $\Delta l_z = \frac{\Delta r \Delta T}{\Delta z}$; subscript '$o$'signifies open circuit stub and $\Delta T = h\Delta\theta$ and h = node index number from the cylinder centre.

In the same manner, the total inductance of the node, L given in (4.24) can be expressed as:

$$L = \begin{bmatrix} L_r \\ L_\theta \\ L_z \end{bmatrix} \tag{4.37}$$

where L_r , L_θ and L_z are the inductance value for the three dimension $r, \theta,$ and z obtained from [16]:

$$\begin{aligned} L_r &= \mu_r \Delta l_r + L_{sr} = L_{\theta z}\Delta T + L_{z\theta}\Delta z + L_{sr} \\ L_\theta &= \mu_\theta \Delta l_\theta + L_{s\theta} = L_{rz}\Delta r + L_{zr}\Delta z + L_{s\theta} \\ L_z &= \mu_z \Delta l_z + L_{sz} = L_{r\theta}\Delta r + L_{\theta r}\Delta y + L_{sz} \end{aligned} \tag{4.38}$$

where subscript 's' signifies short circuit stub.

For proper modelling of any cylindrical TLM node, (4.35) and (4.38) are essential. The velocity of propagation along *i*-directed, *j*-polarised link line, for a cylindrical node is given as

$$v_{ij} = \frac{\Delta i}{\Delta t} \tag{4.39}$$

where $i \neq j$ and

$$\Delta t = \Delta i \sqrt{L_{ij} C_{ij}} \tag{4.40}$$

The characteristic impedance of an *i*-directed, *j*-polarised link line is given as:

$$Z_{ij} = \sqrt{\frac{L_{ij}}{C_{ij}}} = \frac{1}{Y_{ij}} \tag{4.41}$$

The relationship between Δt and Y_{ij} and Z_{ij} can be obtained by combining (4.39) and (4.41) to give (4.42).

$$Z_{ij} = \sqrt{\frac{L_{ij}\Delta i}{\Delta t}};\ Y_{ij} = \sqrt{\frac{C_{ij}\Delta i}{\Delta t}} \tag{4.42}$$

The characteristic admittance of a capacitive stub, Y_{oq} and the characteristic impedance of an inductive stub, Z_{sq} are given in (4.43)

$$Y_{oq} = \frac{2C_{oq}}{\Delta t};\ Z_{sq} = \frac{2L_{sq}}{\Delta t} \tag{4.43}$$

where subscript 'o'and 's'signify open circuit stub and short circuit stubs respectively and 'q' represent the coordinate axis. C is the stub capacitance and L, the stub inductance.

The description of the physical property of the medium is achieved by the combination of its parameters - the capacitance in (4.36) the inductance in

(4.38) and the conditions for time synchronism (4.39). The combination of the 3 parameters produced:

$$Z_{ij} + Z_{ji} + Z_{sk}/2 = \mu_k \frac{\Delta i(h\Delta j)}{\Delta k \Delta t} \tag{4.44}$$

where $i, j, k = r, \theta, z$ and h = index number of the node counting from the centre of the cylinder indicating the node location**.**

4.2 IMPLEMENTATION OF THE CYLINDRICAL TLM ALGORITHM

Having established the theory of cylindrical TLM mesh in the previous Section, the next to be considered in this Section is the implementation of its algorithm. The scatter-connect procedure in the cylindrical TLM is the same as in the SCN TLM discussed in Chapter 2 except that in cylindrical TLM, the discretized spatial lengths are not equal on all direction because there is a gradual increase in the discretized length along the circumference of the cylinder as shown in Fig. 4.3. To accommodate the requirements for synchronism and connectivity in a variable mesh such as cylindrical TLM, it is necessary to add stubs to the node [81]. The geometry of the cylinder is included in the calculation of stubs' values to cater for the changes in the angular discrete length outwardly from the centre.

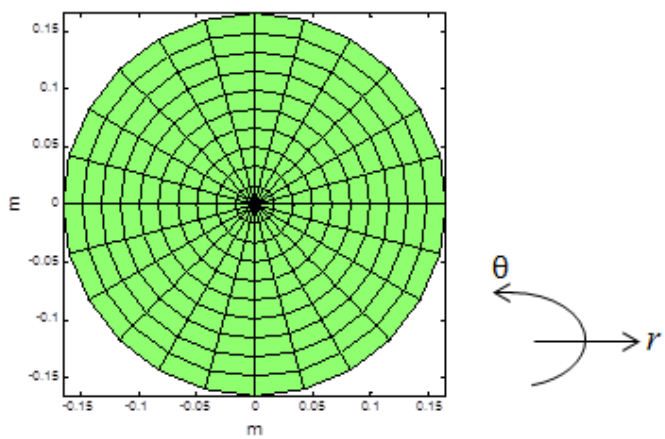

Fig. 4.3: An example of a cylindrical TLM mesh in $r\theta$ view.

A typical cylindrical node is as shown in Fig. 4.4. The nomenclature of the link lines follows the same format as that of the cubic mesh. The first letter in the subscript group represents the direction of the propagation, the second represents the position of the voltage pulse relative to the centre of the node (positive (p) or negative (n) side of the coordinate axis) and the third letter indicates the polarisation of the voltage pulse. This means the port

voltage$V_{rn\theta}^{i}$, for example, represents an r-directed voltage pulse, located on the negative side of the node-centre and polarised in the θ-direction. The superscript letter, i, in this case, indicates that the voltage is incident at the port. If it was a reflected voltage, it is represented by a superscript letter, r, instead.

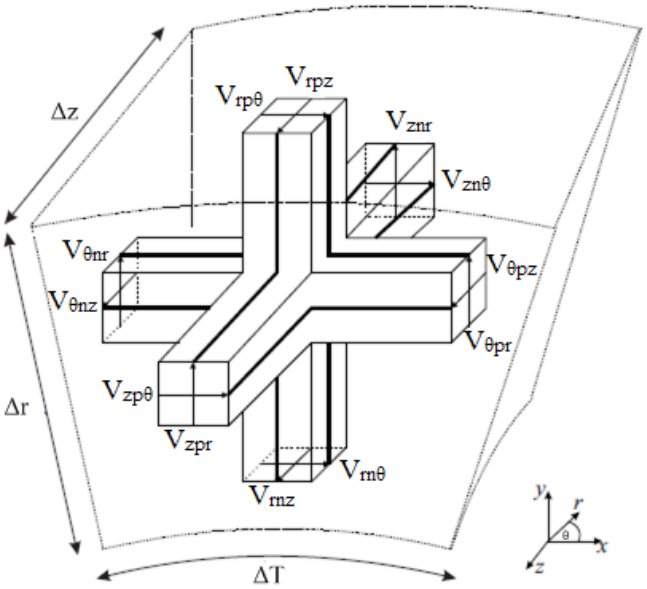

Fig. 4.4: A cylindrical TLM node after Ruddle et al [2].

The scattering procedure using indices i, j, k can be written in a compact form as [32]:

$$V_{inj}^{r} = V_j \pm I_k Z_{inj} - V_{ipj}^{r} + h_{ij} \tag{4.45}$$

$$V_{ipj}^{r} = V_j \mp I_k Z_{ipj} - V_{inj}^{r} + h_{ij} \tag{4.46}$$

where the lower signs apply for indices $(i, j, k) \in \{(r, \theta, z), (\theta, z, r), (z, r, \theta)\}$ and the upper signs apply for indices

$(i,j,k) \in \{(r,z,\theta),(\theta,r,z),(z,\theta,r)\}$, V_j is the equivalent voltage in the j-direction and it is calculated as:

$$V_j = \frac{2\left(V_{knj}^i Y_{knj} + V_{kpj}^i Y_{kpj} + V_{inj}^i Y_{inj} + V_{ipj}^i Y_{ipj} + Y_{oj} V_{oj}^i\right)}{Y_{knj} + Y_{kpj} + Y_{inj} + Y_{ipj} + Y_{oj} + G_j} \tag{4.47}$$

where Y_{oj} is the normalised admittance of the stub and G_j is the conductance stub associated with electric losses in j-direction.

I_k is the equivalent current given as:

$$I_k = 2\frac{\left(V_{ipk}^i - V_{ink}^i + V_{jnk}^i - V_{jpk}^i - V_{sk}^i\right)}{Z_{ink} + Z_{ipk} + Z_{jnk} + Z_{jpk} + Z_{sk} + R_k} \tag{4.48}$$

where Z_{sk} is the normalised impedance of the stub in j-direction and R_k is the resistance stub associated with magnetic losses in j-direction.

Factor h_{ij} is given as:

$$h_{ij} = \frac{Z_{inj} - Z_{ipj}}{Z_{inj} + Z_{ipj}}\left(V_{inj}^i - V_{ipj}^i\right) \tag{4.49}$$

In the solver developed for this thesis, the link impedances and admittances are normalised to the impedance and admittance of free space respectively. Thus, the total current at each of the nodes are calculated as:

$$I_r = 2\frac{\left(V_{\theta pz}^i + V_{zn\theta}^i - V_{zp\theta}^i - V_{\theta nz}^i + V_{sr}^i\right)}{4 + Z_{sr} + R_r} \tag{4.50}$$

$$I_\theta = \frac{2\left(V_{rnz}^i + V_{zpr}^i - V_{znr}^i - V_{rpz}^i + V_{st}^i\right)}{4 + Z_{s\theta} + R_\theta}$$

$$I_z = \frac{2\left(V_{\theta nr}^i + V_{rp\theta}^i - V_{\theta pr}^i - V_{rn\theta}^i + V_{sz}^i\right)}{4 + Z_{sz} + R_z}$$

and the total equivalent voltages at the nodes can be calculated as:

$$V_r = 2\frac{V_{\theta nr}^i + V_{\theta pr}^i + V_{znr}^i + V_{zpr}^i + Y_{or}V_{or}^i}{4 + Y_{or} + G_{or}}$$

$$V_\theta = 2\frac{V_{rn\theta}^i + V_{rp\theta}^i + V_{zn\theta}^i + V_{zp\theta}^i + Y_{o\theta}V_{o\theta}^i}{4 + Y_{o\theta} + G_{o\theta}} \tag{4.51}$$

$$V_z = 2\frac{V_{rnz}^i + V_{rpz}^i + V_{\theta nz}^i + V_{\theta pz}^i + Y_{oz}V_{oz}^i}{4 + Y_{oz} + G_{oz}}$$

The electric field and the magnetic field components are calculated as:

$$E_r = \frac{V_r}{\Delta r}; E_\theta = \frac{V_\theta}{\Delta T}; E_z = \frac{V_z}{\Delta z}$$

$$H_r = \frac{I_r}{\Delta r}; H_\theta = \frac{I_\theta}{\Delta T}; H_z = \frac{I_z}{\Delta z} \tag{4.52}$$

and the admittance and impedance stubs are calculated as:

$$Y_{or} = (2\varepsilon_r \Delta T \Delta z/\Delta r\, c\Delta t) - 4; \quad Z_{sr} = (2\mu_r \Delta T \Delta z/\Delta r c\Delta t) - 4$$

$$Y_{o\theta} = (2\varepsilon_r \Delta r \Delta z/\Delta T c\Delta t) - 4; \quad Z_{s\theta} = (2\mu_r \Delta r \Delta z/\Delta T\, c\Delta t) - 4 \tag{4.53}$$

$$Y_{oz} = (2\varepsilon_r \Delta T \Delta r/\Delta z\, c\Delta t) - 4; \quad Z_{sz} = (2\mu_r \Delta T \Delta r/\Delta z c\Delta t) - 4$$

where Δr, ΔT, and Δz are the unit cell dimension (discretized length) along the radial, angular and z-dimension respectively. c the wave velocity in vacuum and ε_r and μ_r are the relative permittivity and permeability of the medium respectively. Assuming the model background is vacuum, the stubs are normalised to the impedance of free space, Z_0 = 377Ω. The value of ΔT depends on the azimuthal angle and the distance of the node from the centre of the cylinder. It is calculated as:

$$\Delta T = r_n \Delta\theta \tag{4.54}$$

where $\Delta\theta$ is the azimuthal discrete angle and r_n is the node distance from the origin in meter given as:

$$r_n = (0.5(i\Delta r + (i+1)\Delta r) \tag{4.55}$$

where i is the radial index.

$G_r, G_\theta, G_z, R_r, R_\theta$ and R_z are additional six stubs added to the node to take into account possible losses in modelling of inhomogenous, anisotropic media and are given by (4.56). Energy scattered into any of these stubs is absorbed and not reflected back into the node because the stubs are assumed to be infinitely long or terminated in their own characteristic impedance. The loss stubs are calculated as:

$$G_r = Z_0\sigma_e\Delta T\Delta z/\Delta r\,; \quad R_r = \sigma_m\Delta T\Delta z/Z_0\Delta r$$

$$G_\theta = Z_0\sigma_e\Delta r\Delta z/\Delta T\,; \quad R_\theta = \sigma_m\Delta r\Delta z/Z_0\Delta T \tag{4.56}$$

$$G_z = Z_0\sigma_e\Delta T\Delta r/\Delta z\,; \quad R_z = \sigma_m\Delta T\Delta r/Z_0\Delta z$$

The voltages scattered into the link lines are connected to adjacent nodes using [117]:

$$V^i_{rpz}(r,t,z) = V^r_{rnz}(r+1,t,z);\;\; V^i_{rnz}(r+1,t,z) = V^r_{rpz}(r,t,z)$$

$$V^i_{\theta pz}(r,t,z) = V^r_{\theta nz}(r,t+1,z);\;\; V^i_{\theta nz}(r,t+1,z) = V^r_{\theta pz}(r,t,z)$$

$$V^i_{rp\theta}(r,t,z) = V^r_{rn\theta}(r+1,t,z);\;\; V^i_{rn\theta}(r+1,t,z) = V^r_{rp\theta}(r,t,z)$$

$$V^i_{\theta pr}(r,t,z) = V^r_{\theta nr}(r,t+1,z);\;\; V^i_{\theta nr}(r,t+1,z) = V^r_{\theta pr}(r,t,z) \tag{4.57}$$

$$V^i_{zp\theta}(r,t,z) = V^r_{zn\theta}(r,t,z+1);\;\; V^i_{zn\theta}(r,t,z+1) = V^r_{zp\theta}(r,t,z)$$

$$V^i_{zpr}(r,t,z) = V^r_{znr}(r,t,z+1);\;\; V^i_{znr}(r,t,z+1) = V^r_{zpr}(r,t,z)$$

4.3 IMPLEMENTATION OF CENTRE BOUNDARY IN CYLINDRICAL TLM METHOD

When solving electromagnetic problem in cylindrical coordinates using TLM, modelling of the space on the centre axis has been known to pose a challenge. The challenge is that the type of boundary used for the cylinder centre termination could affect simulation results. It is important to give special attention to the accurate modelling of this centre point in order to avoid error in the simulations [118] **.**

Modelling the centre of the cylindrical cavity using cylindrical TLM mesh can be achieved in two ways. The first approach is to place a magnetic boundary at the centre of the cylinder and the second is to terminate the centre of the cylinder with an electric wall, equivalent to placing a thin wire at the centre of the cylinder. Using an electric wall termination is based on the fact that there is no cross talk between nodes in TLM mesh and there is no communication across the centre of the cylinder from one side of the symmetry to the other. Thus, it is expected that the voltage at the centre of the cylinder should be equal to zero i.e. $V_{(r=0)} = 0$. This is possible in the EM wave simulation when the centre boundary is described as a coaxial system with an infinitely thin central conductor at $r = 0$. This means the centre is described with a reflection coefficient, $\Gamma = -1$. This method works well with a coaxial cavity model. However, in the case of an air-filled cavity, the centre of the cylinder is assumed to have zero voltage. This means that the impedance is assumed to be infinite and $\Gamma = 1$ [11]. Therefore, to model the centre of the air-filled cavity correctly, it is better to treat the centre boundary as a magnetic wall. The choice between the two methods depends on the type of model being considered.

4.4 VALIDATION OF THE DEVELOPED CYLINDRICAL TLM SOLVER

In Section 3.3, it was noted that the staircase approximation of the curved boundary affected the accuracy of the resonant frequency of the simulated electric field when rectangular mesh was applied to the model. In this Section, the cylindrical TLM mesh is applied to the modelling of circular cavity to verify the efficiency of the cylindrical mesh in modelling the circular cavity compared to the rectangular mesh. The resonant frequency of cylindrical cavity was analytically calculated using equation (3.4) discussed in Section 3.1 of Chapter 3.

4.4.1 SIMULATION OF AIR-FILLED CYLINDRICAL CAVITY MODEL AND SIMULATED RESULTS

The same cavity modelled in Section 3.3 of Chapter 3 (Fig. 3.7) is repeated here in this Section. The decision to use the same example was based on the need to facilitate easy comparison of results obtained from the rectangular model to the results of the cylindrical model. The simulated cavity has a radius of 50 mm and height of 100 mm. The cavity was represented by a mesh of (10 x 60 x 10) nodes for a dispersion frequency limit of 6 GHz. However, since the variation in z-direction is not being considered, a 2D slice on the z-axis is sufficient for the required model, meaning that only (10x60x1) nodes are required for the model.

The structure was excited by an impulse voltage of 1V applied at node (6, 1, 1) in the mesh and the output was taken at the same node as the vertical component of the electric field (E_z). The centre of the cavity was modelled as a magnetic wall and simulations was done with 16382 time steps. The resonant frequencies for the simulated cavity are shown in Fig. 4.5. The simulated resonant frequencies are compared with the analytically generated results in Table 4.1 and are found to have good agreement. The simulated

modes TM 010 and TM 020 as shown in Fig. 4.6 and Fig. 4.7 also correspond to the simulated resonant frequencies as theoretically expected.

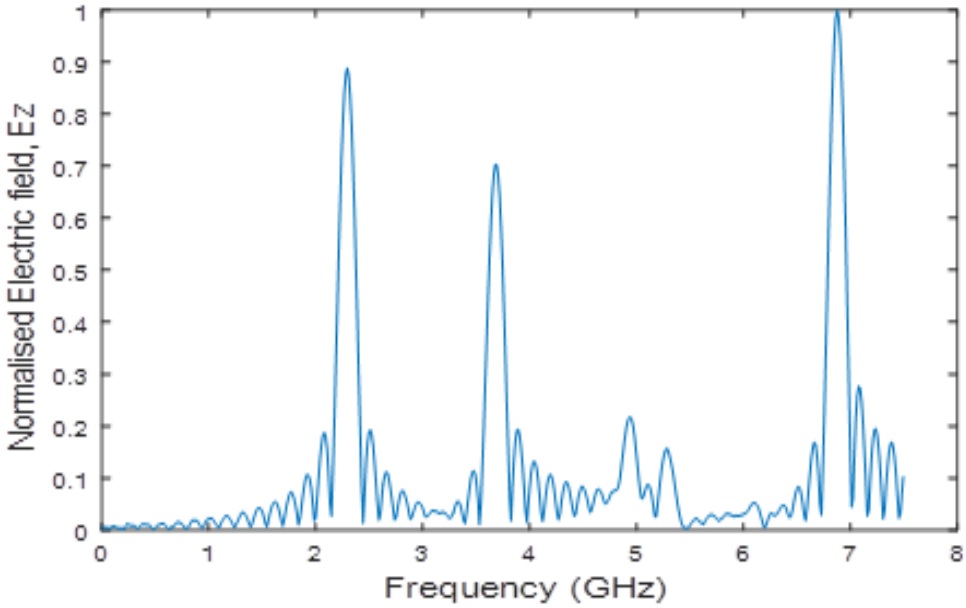

Fig. 4.5: The simulated frequency response for the air-filled cavity.

Table 4.1: The simulated and analytical resonant frequencies for the empty cylindrical cavity

Modes	Analytical (GHz)	Simulated (GHz)
TM 010	2.295	2.297
TM 020	3.657	3.666
TM 030	4.901	4.929
TM 110	5.268	5.278
TM 120	6.6948	6.876

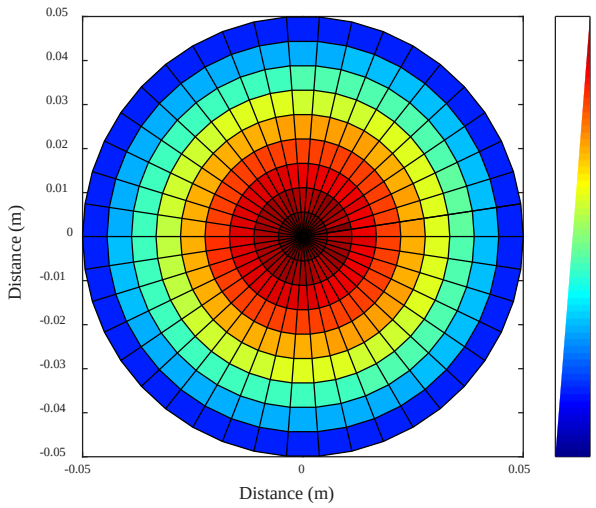

Fig. 4.6: The simulated mode (TM 010) for a circular cavity of 50 mm radius at 2.297 GHz with magnetic wall centre termination after 16384 iterations.

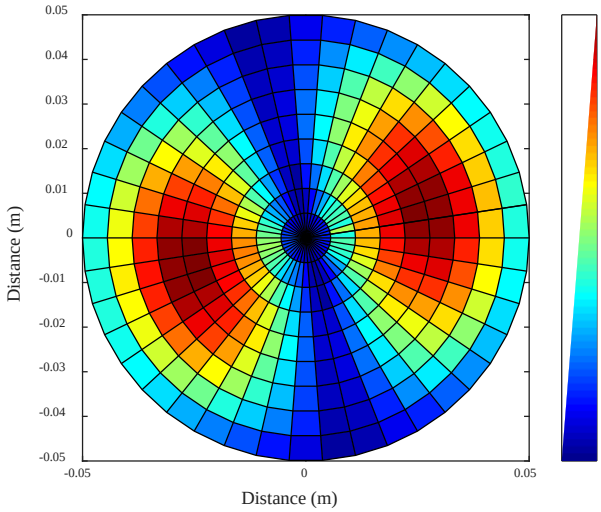

Fig. 4.7: The simulated mode (TM 110) for a circular cavity of 50 mm radius at 3.666 GHz with magnetic wall centre termination after 16384 iterations.

Considering the correlation of the cylindrical mesh to the modelled cavity shape, the mesh mapped accurately with the cavity structure and the mode distribution was spread smoothly through the mesh. This is an improvement over the uneven distribution of the field experienced with the use of the rectangular mesh as a result of staircase approximations.

These results not only shows that the cylindrical TLM mesh is in principle better suited to the modelling of curved boundaries than the rectangular mesh, they also demonstrate that the developed solver TLS has been correctly implemented and can be confidently applied to the modelling of the radiating structure, which is the aim of this research. Unlike the rectangular mesh, the symmetry about the centre axis of the cylindrical mesh can be employed in such a way that only one layer of nodes in the theta dimension is applied to simulate the cavity. This will result in a substantial saving in time and memory required for the simulation procedures.

To further validate the cylindrical TLM solver TLS, a coaxial cavity was simulated in Section 4.4.2 and the result compared to the same model simulated in CST. A dielectric loaded cavity was also simulated and results compared to the published results in Section 4.4.3.

4.4.2 Simulation of Coaxial Cavity Model and Simulated Results

A coaxial cavity of 50 mm outer radius and an inner thin wire of radius 2 mm were simulated. The centre wire running from the top to the bottom of the cavity was position at the centre of the cavity as shown in Fig. 4.8. Only a slice on the *z*-axis, taken as the length along the height of the cavity, was considered meaning there are only mode variation in the r and θ dimensions and not in the z dimension. The cavity was meshed with $r \times \theta \times z = 25 \times 63 \times 1$ nodes such that the smallest cell coincided with the radius of the

inner wire. The dispersion frequency limit for this mesh was approximately 6.14 GHz.

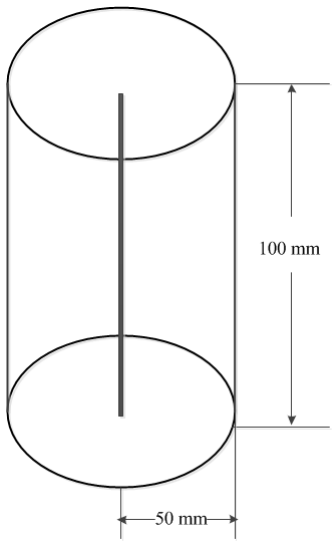

Fig. 4.8: The simulated coaxial cavity with an inner wire of 2 mm at the centre.Two methods were attempted for the modelling of the inner wire. In the first attempt, the node representing the wire was modelled as a short node represented with a reflection coefficient $\Gamma = -1$ and the second attempt was just to model the wire as copper with electric conductivity = $5.8 \times 10^7\ \mathrm{Sm}^{-1}$. The centre and the outer walls of the cavity were modelled as an electric wall. The cavity was excited with 1V impulse voltage at (12,1,1) and the electric field observed at the same node.

As shown in Table 4.2, TLS produced the same simulation results for both models and the simulated results of the CST was only shifted by 0.01 GHz when the wire was modelled with copper compared to when it was modelled as a short circuited node. It can then be deduced from the results that the two methods produced the same results and the choice of one over the other depends on the need or choice of individual.

Table 4.2: The simulated resonant frequencies for the coaxial cavity with inner conductor simulated as short circuit nodes compared with the one simulated as copper material

TLS (GHz)		CST (GHz)	
Copper	Short circuit	Copper	Short circuit
2.88	2.88	2.89	2.88
3.68	3.68	3.65	3.64
4.91	4.91	4.86	4.85

The mode distributions for the first three modes simulated with TLS are compared with the mode simulated with CST in Table 4.3.

The simulated resonant frequencies for the coaxial cavity are higher than the simulated frequencies in the modelled air-filled cavity but the mode distribution is similar except for the effect of the inner wire can be seen at the centre of the mesh. Although the field's distribution obtained in the cavity modelled with the hexahedral mesh was observed to be better than the distribution obtained with the use of rectangular mesh where staircase effect could be vividly seen; the distributions were still not as smooth as the ones obtained from the cylindrical mesh. This further confirms that the boundary is well mapped into the mesh of the cylindrical TLM compared to its parallelepiped counterpart. The stability of TLS in the presence of the wire also confirmed that the stubs were well implemented in the developed solver giving a better confidence of its suitability for the modelling of axisymmetric radiating structures.

Table 4.3: The simulated results generated from the TLS code compared with the CST simulation for a coaxial cavity

Cylindrical TLM Simulation	CST simulation
2.88 GHz 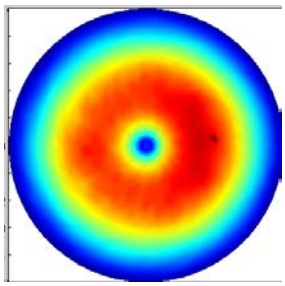	2.88 GHz 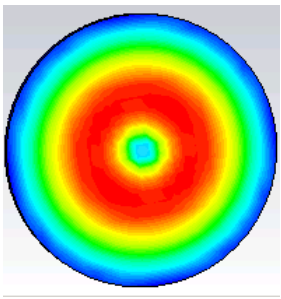
3.68 GHz 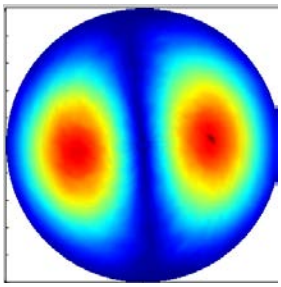	3.64 GHz 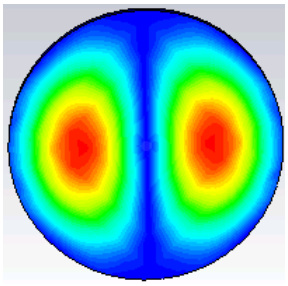
4.91 GHz 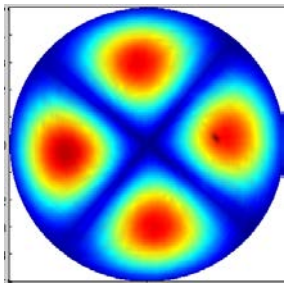	4.85 GHz 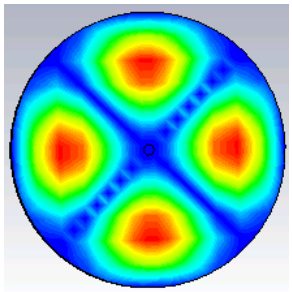

4.4.3 SIMULATION OF DIELECTRIC LOADED CYLINDRICAL CAVITY AND SIMULATED RESULTS

In this Section, the effects of loading a microwave cylindrical cavity with radial dielectric rod using the cylindrical TLM modelling method are discussed. The dielectric-loaded cylindrical cavity problem presented in [120] was simulated using the developed cylindrical TLM solver, TLS. The simulated results are compared with the published results.

Perturbation method [121], [122] where dielectric/metallic rod is inserted into the cavity is the most common practice to alter the resonant frequency of the cavity. With this method, the resonant frequency of the cavity can be controlled by the material properties of the inserted rod or by adjusting its level of penetration into the cavity [123]. Dielectric loaded cavities are a special type of resonator and have found applications in microwave filters for satellite and mobile communication as a result of their small size, low loss and temperature stability [124], [125]. These applications have attracted further research and there is a significant number of publications reporting the numerical calculation of resonant frequencies of canonical metallic cavities loaded with dielectric resonators [126]–[132].

The radius of the cavity described by Chan and Reader is 40 mm and the height is 75 mm [120]. The schematic diagram of the simulated cavity is as shown in Fig. 4.9. The analytical resonant frequency for the dominant mode (TM 010) of the cylindrical cavity, before dielectric loading, is 2.871 GHz. The cavity was excited such that only the TM modes were generated and the simulated frequency for TM 010 using the cylindrical TLM solver is 2.874 GHz as shown in Fig. 4.10. Having confirmed the result of the solver for the unloaded cavity is satisfactory, the first mode of the cavity is set as the point of reference for all other results.

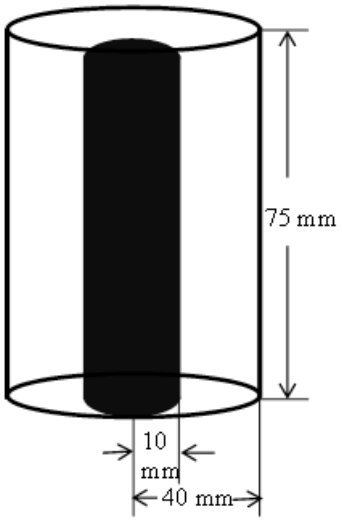

Fig. 4.9: Simulated dielectric loaded cylindrical cavity.

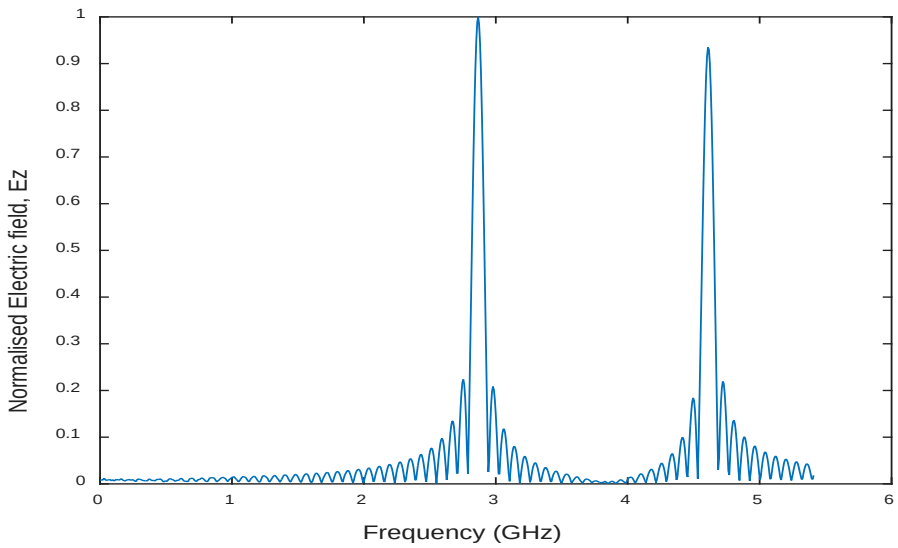

Fig. 4.10: Simulated resonant frequency for the unloaded cylindrical cavity.

The loading dielectric rod was coaxially positioned at the centre of the cylindrical cavity. It was 10 mm in diameter with permittivity, ε_r = 25. The distribution of the permittivity in the coaxially dielectric-loaded cavity is anisotropic in nature unlike the air-filled cavity, which has evenly distributed permittivity at every point in the cavity. In the dielectric-loaded

case, there are two materials of different permittivity values inside the cavity – air ($\varepsilon_r = 1$) and the dielectric material ($\varepsilon_r = 25$). As earlier mentioned in Section 3.2 of Chapter 3, it is generally recommended that Δl should be less than $1/10$ of the shortest wavelength in order to reduce dispersion error [32] in TLM models. Therefore, for accurate implementation of the dielectric loaded-cavity, the permittivity difference in the cavity should be taken into account when dealing with the space discretisation to ensure that the dispersion constraint of at least 10 nodes per wavelength at the maximum frequency of interest is satisfied at every part of the modelling space [39]. This means that the dielectric material with higher relative permittivity value requires corresponding smaller nodes. Number of nodes in the dielectric layer, N_d is calculated as [18]:

$$N_d = N_a/\sqrt{\varepsilon_r} \tag{4.58}$$

where N_a is the number of nodes in the air

The dispersion cut-off frequency calculated for the cavity was 6 GHz. Simulated results for the dielectric loaded cavity are shown in Table 4.4. The results are accurate within a 1 % error within the mesh dispersion limit when compared to the analytical results. The results also compared well with the simulated results published in [120] and [18] for the same problem.

Table 4.4: Comparison of the analytical results with the simulated results for the cavity loaded with dielectric rod

	Resonant Frequency (GHz)			
Mode	Analytical	Chow [120]	Jukovic [18]	Simulated (TLS)
TM010	1.0189	1.0190	1.0396	1.0100
TM020	3.5702	3.5740	3.5592	3.5560
TM030	4.9917	4.9930	Not published	5.0950
TM040	6.8346	6.8460	Not published	7.0370

4.4.4 EFFICIENCY OF CYLINDRICAL MESH COMPARED WITH THE RECTANGULAR MESH

In Section 3.3, it was seen that the staircase approximation of curved boundaries affected the accuracy of the resonant frequency of the simulated electric fields when rectangular mesh was applied to the modelling of circular cavity. The staircase error does not occur in the cylindrical TLM model as discussed in Section 4.4.1 and in the absence of staircase errors, cylindrical TLM mesh yielded results with better accuracy. The purpose of this Section is to further verify the efficiency of the two models - rectangular and cylindrical mesh - in modelling of the circular cavity.

The first comparison was made on the efficiency of the time steps and the second on the total number of operations involved in the execution of each of the model. Table 4.9 summarises the simulated results obtained for the dominant mode of the cavity (TM010) using the two meshes. For accurate comparison, an equivalent number of iterations used in the rectangular mesh was derived as [72]:

$$N_{cub} = \frac{N_{cyl}\Delta t_{cyl}}{\Delta t_{cub}} \tag{4.59}$$

where Δt_{cub} and Δt_{cyl} are the discrete time step in rectangular and cylindrical models respectively, while N_{cub} and N_{cyl} are the number of iterations in rectangular and cylindrical models respectively.

To compare the execution time for the two methods, using equal number of iterations, the number of operations, N_{op} for each of the model is calculated from the mesh dimension, number of iterations (N_{cyl} and N_{cub}) and the number of performed operations in the execution of model, P. For the cylindrical model, N_{op} is given as [72]:

$$N_{op} = N_r \times N_\theta \times N_z \times N_{cyl} \times P \tag{4.60}$$

and for the rectangular model, N_{op} is given as:

$$N_{op} = N_x \times N_y \times N_z \times N_{cub} \times P \tag{4.61}$$

where N_r, N_θ, N_x, N_y and N_z are the number of nodes in r,θ, x, y and z respectively. N_z = 1 for both models.

Three simulations were considered. The first simulation was conducted using 121 rectangular nodes. An odd number was selected to ensure that the symmetry of the cavity from one side to the other was not compromised. To achieve this, one node was set as the centre of the cavity while the remaining was evenly distributed along the diameter of the cavity. The second simulation was conducted using 120 cylindrical nodes in order to get the number of the nodes used for the cylindrical mesh as close to the

rectangular mesh as possible. The third simulation was conducted with a more coarse cylindrical mesh than the one used in the second simulation to check how it affects the results. In this third example, only 60 cylindrical nodes were used. The simulated resonant frequencies for the cavity and the mode distribution in the cavity are as shown in Fig. 4.11, Fig. 4.12. The results obtained from using the two methods are compared in Table 4.5.

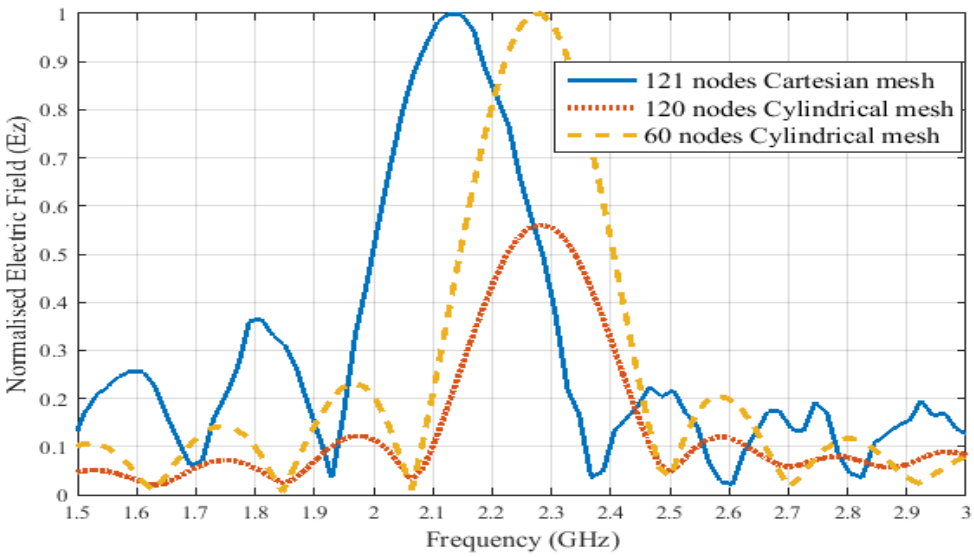

Fig. 4.11: The simulated normalised electric field for the cavity (analytical frequency = 2.295 GHz).

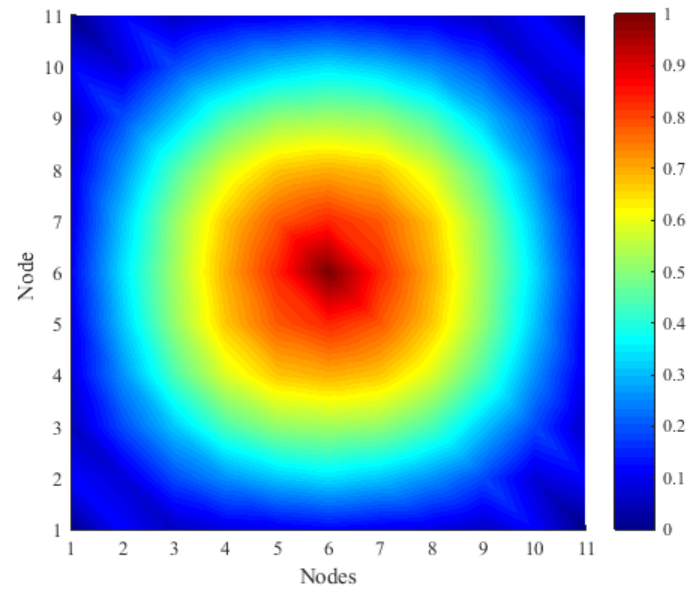

Cartesian TLM ($x \times y$ = 11×11 nodes)

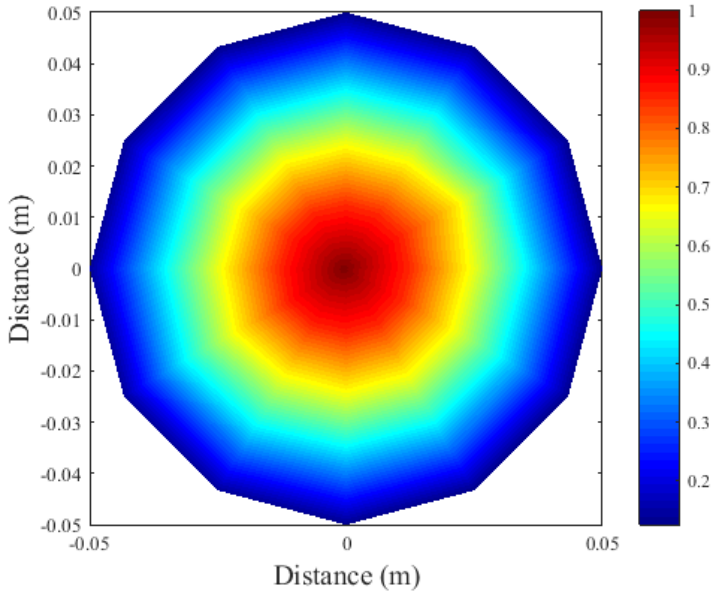

Cylindrical TLM ($r \times \theta$ = 5×12 nodes)

Fig. 4.12: The normalised simulated TM010 mode for the circular cavity using 120 cylindrical nodes and 121 rectangular nodes.

Table 4.5: Comparison of simulated results of using rectangular mesh, cylindrical mesh and coarse cylindrical mesh for the simulation of circular cavity.

	Cartesian TLM	Cylindrical TLM	Cylindrical TLM
Nodes	121 ($x \times y$ = 11×11 nodes)	120 ($r \times \theta$ = 5×12 nodes)	60 ($r \times \theta$ = 5×6 nodes)
discrete time step	1.5×10^{-11}	4.3633×10^{-12}	3.5368×10^{-12}
Number of iterations	298	2048	2526
Frequency (GHz)	2.13	2.282	2.282
Error in result (%)	6.98	0.39	0.39
Analytical frequency = 2.295 GHz			

The discrete time step used in the execution of the rectangular TLM procedure for the mesh of 121 nodes was 1.5×10^{-11} and the number of iterations, N_{cub} was 298 while the time step used in the execution of the cylindrical mesh procedure for the mesh of 120 nodes was 4.3633×10^{-12} and the required number of iterations, N_{cyl} was 2048. It was observed that the $N_{cyl} = 6.87 \times N_{cub}$, meaning that the number of iterations is higher in the cylindrical TLM model compared to its rectangular TLM counterpart.

However, assuming the same number of iterations N, the calculated $N_{op} = 121Np$, $120Np$ and $60Np$ for the 121 nodes, 120 nodes, and the 60 nodes mesh respectively. That is, the number of operations required in the implementation of the cylindrical mesh is lower compared to the rectangular

mesh. This means that the overall execution time is reduced in the cylindrical model.

As shown in Table 4.5, the improvement in results obtained by modelling with the cylindrical mesh is appreciable and was also achieved with fewer nodes compared with the rectangular mesh. In the simulated example, the error in the results obtained using 121 nodes rectangular mesh was 6.98 times higher than the error generated using 120 nodes cylindrical mesh. Compared to the same model simulated with a more coarse cylindrical mesh of 60 nodes, 4.3633e-12 discrete time step, 1024 iterations; the error from 121 nodes rectangular mesh was still 6.98 times higher. These results show that a cylindrical mesh of 60 nodes is sufficient for the accurate simulation of the cavity, which prove that the cylindrical mesh allows for savings in the time and storage resources.

To further verify this claim, new simulations were run in both rectangular and cylindrical TLM with the aim to achieve the same level of accuracy. The results are as shown in Table 4.6. Comparing the results obtained using the two methods, the difference in the number of nodes required to obtain the same level of accuracy in rectangular TLM is 377.50 times higher as in the cylindrical TLM and the corresponding simulation time in the rectangular TLM significantly higher. The storage space taken by the rectangular mesh is also 47.2 times larger compared to the cylindrical mesh. This shows that there is an enormous savings in term of computing time and storage resources when using the cylindrical TLM mesh.

Table 4.6: Comparison the simulated results for the circular cavity using rectangular mesh and cylindrical mesh at the same level of accuracy.

	Cartesian TLM	Cylindrical TLM
Nodes	90601 ($x \times y$ = 301×301 nodes)	240 ($r \times \theta$ = 10×12 nodes)
Discrete time step	1.5614×10^{-14}	1.0908×10^{-12}
Number of iterations	16302	8192
Frequency (GHz)	2.290	2.291
Simulation time (s)	108035	87.16
Storage space	23.6 MB	500 KB
Error in result (%) = 0.17, Analytical frequency = 2.295 GHz		

In addition, symmetry application is another point where the cylindrical mesh has upper hand over the rectangular mesh. For the rectangular TLM application, the minimum section that can be simulated when applying the rule of symmetry is a quarter of the cylindrical cavity whereas it is possible to simulate the cavity with a thin mesh slice in cylindrical TLM and attain exactly the same result as when the whole mesh is used for the simulation. For example, using a single slice $r \times \theta \times z = 5 \times 1 \times 1$ mesh produced the same result as using the full plane mesh of $r \times \theta \times z = 5 \times 12 \times 1$ mesh reducing the simulation time from 54.49s to 14.24s.

4.5 CONCLUSIONS

An electromagnetic TLM solver TLS developed in MATLAB was applied to the modelling of different canonical problems: a rectangular cavity, an air-filled circular cavity, a coaxial cavity and a dielectric loaded cavity. The simulated results are in good agreement with the analytical expectations. Simulated results also compared well with the results obtained form an existing solver and with results obtained from the literature.

The analysis of the rectangular resonant cavity was carried out using the 2D shunt TLM and SCN TLM methods. To verify the accuracy of the TLM, the simulated results were compared with the analytical results and the results of the commercial electromagnetic simulator, CST and it was found to be accurate with an error of less than 0.1% for the considered example.

For the circular cavity model, the resonant frequencies were obtained from the characteristic equation discussed in Chapter 3 (3.2) and were used as benchmark for the simulated results. In modelling of the circular resonator, both rectangular mesh and cylindrical mesh models were considered. The two methods did not produce the same results. In the case of rectangular model, the staircase approximation affected the accuracy of the results by shifting the simulated resonances down compared with the analytical expectations. Increasing the mesh size produced better results but at the expense the time, storage and a higher dispersion. Simulated results obtained from the cylindrical mesh are more accurate than those obtained using the rectangular mesh. The savings in memory and time observed when using cylindrical mesh is highly commendable when compared with the rectangular mesh simulations. Another advantage of the cylindrical mesh is in the possibility of exploiting the symmetry about the centre axis such that only one layer of nodes in the theta dimension is required for the simulation of the entire cavity. A large simulation space will be required for the

modelling of axisymmetric radiating structures that will be discussed in Chapter 5 and symmetry application will be applied to reduce the simulation time and storage memory that will be required.

In summary, by comparing the simulated results of modelling circular cavity with the rectangular and the cylindrical meshes, it has been confirmed that the cylindrical mesh is more accurate than the rectangular mesh in modelling curved boundaries. Therefore for the purpose of this thesis, the cylindrical mesh is considered a preferred choice for the simulation of axisymmetric radiating structures, which will be discussed in Chapter 5.

CHAPTER 5

THE CYLINDRICAL TRANSMISSION LINE MODELLING OF AXISYMMETRIC RADIATING STRUCTURES

In this Chapter, the modelling procedure for the axisymmetric radiating structures using the cylindrical TLM method is discussed. The cylindrical TLM mesh was discussed in Chapter 4. Before proceeding into the modelling procedures, a short introduction to a range of typical axisymmetric antenna structures - cylindrical dipole, cylindrical monopole and conical monopole antennas - is presented in Section 5.1. These radiating structures will be simulated using the cylindrical TLM mesh of the developed Transmission Line Simulator (TLS). The cylindrical TLM mesh has been chosen, over its rectangular counterpart, for the simulations of these axisymmetric radiating structures because mesh-to-structure conformity is possible with the use of cylindrical mesh and its application promises potentially more accurate results as discussed in Section 4.6.3 of Chapter 4. The simulation procedures and simulated results for these structures using the cylindrical TLM mesh are discussed in Section 5.2. Measured results from the fabricated prototype antennas are presented in Section 5.3 to validate simulated results while conclusions to this Chapter are drawn in Section 5.4.

5.1 INTRODUCTION TO THE AXISYMMETRIC RADIATING STRUCTURES

As previously mentioned, the cylindrical dipole, cylindrical monopole and conical monopole antennas are examples of structures that possess axial symmetry. In this Section, a short introduction to these structures is presented.

5.1.1 CYLINDRICAL DIPOLE AND CYLINDRICAL MONOPOLE ANTENNAS

Cylindrical dipoles and monopoles are inexpensive, simple antennas and can be made from wire. Both antennas are desirable because despite their simplicity, they can be used to achieve some degree of wideband antenna characteristics by modifying the conductor thickness. Wideband antennas are needed for applications that require coverage of a broad range of frequencies such as in television reception of all channels [20], [133].

A dipole is made of two bilaterally-symmetric, identical radiating elements separated at the centre by an insulator. The two elements are connected to a feed line, which is usually a 50-Ω impedance coaxial cable. To make the dipole resonant, its total electrical length should be half-wavelength ($\lambda/2$) of the lowest desired operating frequency. The lowest frequency at which the dipole resonates is called the *fundamental frequency* and the subsequent resonances occur at odd multiples of the fundamental frequency [20].

When one of the radiating elements of the dipole antenna is replaced by a finite conducting surface/plane termed *ground plane*, it becomes a monopole antenna, making the length of the monopole a quarter-wavelength ($\lambda/4$) at the desired fundamental frequency. When placed over a large ground plane, a quarter-wave monopole antenna excited by a source at its base displays the same radiation pattern in the region above the ground as a half-wave dipole in free space. This simply means that the conducting plane

commonly referred to as the ground plane, replaces the second conducting wire of the dipole. The ground plane behaves like the other half of the dipole and if the ground plane is sufficiently large, the monopole antenna can be as strong as the dipole in its radiation. The monopole can only radiate above the ground plane and so, the angular image of the radiation is limited to $0 \leq \theta \leq \pi/2$ compare to $0 \leq \theta \leq \pi$ in a dipole antenna. The simplicity in construction and the broadband characteristics of the monopole antenna [134] lend to its common use in portable equipment such as mobile/cellular telephone and automobiles. It is also widely used in ground-based communications systems wireless sensor networks [135]–[137].

The broadband nature of the cylindrical monopole, as that of the dipole, depends on the thickness of its diameter [20]. The thin dipole is generally considered narrowband while the thick ones are broadband. Although, large diameter dipole and/or monopole are more broadband in nature, the diameter of the radiating structure should be chosen with care because they resonate at lower frequencies than their thin counterpart. On the other hand, the radiation characteristics of dipoles are also frequency dependent. The rate at which these characteristics change as a function of frequency depends on the antenna bandwidth. For very thin dipoles/monopoles, small alterations in the frequency of operation result in large changes in its operational behaviour. In order to reduce the sensitivity of the dipole radiation characteristics as a function of frequency for a given length of wire, the ratio of the antenna length to its diameter (l/d ratio) has to be controlled. One conventional way by which its operational bandwidth can be enlarged in an acceptable way is to decrease the length to diameter ratio (l/d ratio). The sensitivity of the dipole to frequency changes reduces as the l/d ratio decreases.

5.1.2 CONICAL MONOPOLE ANTENNAS

In this Section, the conical antenna is introduced. As mentioned previously, the bandwidth of monopole antennas depends on the diameter of the radiating structure. Conical monopole antennas have large surface areas, which give them a broad bandwidth characteristic [133]. In addition to having broad bandwidth, conical antennas also have omnidirectional radiation pattern. For both military and commercial applications, there is an increasing demand for Ultra Wide band (UWB) antennas with omni-directional coverage [138]. These characteristics possessed by the conical monopole have attracted research interest to the structure [139]–[142].

A conical antenna is made up of a cone, with or without a spherical cap, and a horizontal ground plane. Ideally, the ground plane is infinitely large but in practice, it is impossible to have an infinite ground plane for the conical antenna. Therefore, the ground plane is usually built as a reflective plane of finite size. The consequence of using a finite ground plane in practice is that end reflections and standing waves are introduced, which in turn reduces the bandwidth of the antenna and introduces unwanted effects such as significant back lobes in the radiation pattern of the antenna [143], [144].

5.2 ANTENNA MODELLING USING DEVELOPED TRANSMISSION LINE SIMULATOR

In this Section, the cylindrical dipole, cylindrical monopole and conical monopole introduced in Section 5.1 are simulated using cylindrical TLM mesh. Using the cylindrical TLM solver for the simulations means that antennas are simulated in the cylindrical coordinate instead of the conventional spherical coordinate. General descriptions of the method adopted for the antenna feed and the application of the absorbing boundary will be discussed in the following Sections. Simulated results for the three antennas are also presented and discussed. Since the cylindrical dipole and cylindrical monopole antennas are similar, both are discussed in Section 5.2.1 while the conical monopole is discussed in Section 5.2.2.

5.2.1 MODELLING OF CYLINDRICAL DIPOLE AND CYLINDRICAL MONOPOLE ANTENNAS

Procedures for the simulation of the cylindrical dipole and cylindrical monopole antennas are presented here. These two antennas have their dimensions chosen in order to operate at approximately 2 GHz.

5.2.1.1 ANTENNA DIMENSIONS

The lengths of the two antennas were determined based on the wavelength λ of the desired operating frequency. For the 2 GHz operating frequency, λ = 150 mm. The length, l of the simulated dipole antenna was set to 75 mm. This length was chosen because it is a fundamental requirement that the dipole antenna be half-wavelength long ($l = \lambda/2$) in order for it to radiate [20]. Each radiating element of the dipole was 37.5 mm long in length. The diameter, d of the dipole antenna was set to 3 mm resulting in *l/d* ratio of 25. For a 2 GHz operating frequency, the required length for the monopole, $l =$

$\lambda/4 = 37.5$ mm. The monopole was positioned at the centre of a circular ground plane of 2λ diameter.

5.2.1.2 THE MESHING PROCEDURE

In the example discussed in this Section, the two antennas simulated were discretised in computational cylindrical modelling space of $200 \times 251 \times 200$. The discretization of lengths for the TLM simulation were chosen such that the largest discrete lengths conform to the 0.1λ dispersion limit [42]. These radiating structures were positioned symmetrically about the origin with their lengths directed along the z-axis in the simulation space. Radiating elements were simulated as copper with electric conductivity, $\sigma_c = 5.8 \times 10^7$ S/m. The ground plane used for the monopole was also simulated as copper.

The axisymmetric nature of the antenna and the simulation space means that one slice of θ was sufficient for the simulation. Application of the symmetry resulted in total of $200 \times 1 \times 200$ nodes for the simulation. The largest discretised length was 3.75 mm and it was determined based on the λ of the expected highest frequency within the acceptable dispersion cut-off frequency range, in this case, 8 GHz. The discretised time step for the simulation of the both dipole and monopole antennas was 1.5645×10^{-14} s.

In the simulation space, the dipole antenna was positioned in such a way that a node serving as the input port was separating the two radiating elements of the dipole. The feeding port was modelled to serve as the 50 Ω matching feed point. The detailed procedure of the port model is described in Section 5.2.1.3. The feeding node increased the total length of the antenna by 1.5 mm making the total length 76.5 mm and l/d ratio of 25.5. The simulation mesh view for the dipole in the *r*-*z* plane is as shown in Fig. 5.1 (a). Likewise, the monopole was positioned in the simulation space such that a node was separating the radiating structure from the ground plane and

this node served as the feeding node. The feeding node increased the length to 39 mm giving $l/d = 13$. The *r*-*z* view of meshes used for the dipole and the monopole are shown in Fig. 5.1. Only one slice of the simulation space was simulated because of symmetry. Thus, in order to aid the visualisation of the antenna in the mesh, the image was mirrored at the centre of symmetry on *r*. The image has also been zoomed in from its original size.

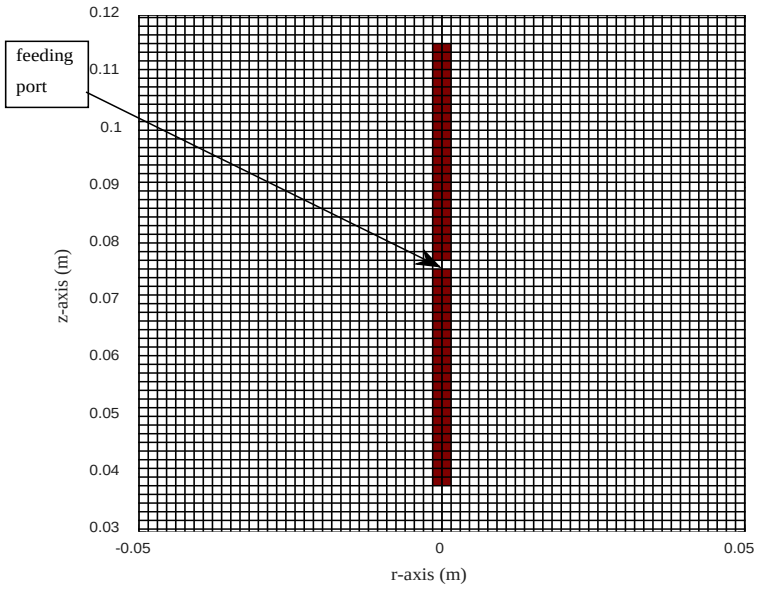

(a) Cylindrical dipole

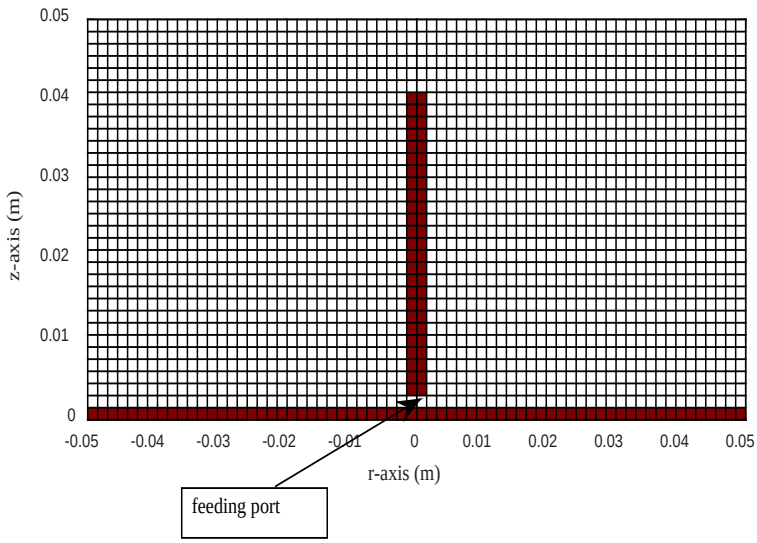

(b) Cylindrical Monopole

Fig. 5.1: Simulated (a) dipole and (b) monopole in the simulation space with the red lines indicating the copper and meshed background representing the open space.

5.2.1.3 ANTENNA EXCITATION PROCEDURE

Once the meshing procedure was completed, the antenna was excited using the procedure discussed in this Section. There are various ways by which an excitation pulse can be applied to the radiating structure in TLM [3]. Three different methods are briefly described and the novel approach adopted for excitation of the antennas in the simulations reported in this thesis is then presented.

One of the known methods for exciting antennas in TLM model is to model the feed wire/node(s) as a short circuit placed in the middle of link line(s) and then impose the incident voltage pulses on the adjacent ports. The second possible approach is to model the feed wire/node(s) as a short circuit placed in the middle of link line(s) and then induce a current by imposing a magnetic field. The third method involves connecting a voltage source with known internal impedance to the antenna. This third method is referred to as the wire-feed model and it is achieved in TLM by manipulating the capacitance and inductance of the wire node to accommodate the presence of the wire in the simulation space [145]. For the examples in this thesis, the method used in the excitation of the simulated antenna is a novel optimised version of the second method described above.

To excite the simulated antenna, the node directly between the two poles of the dipole and the node between the monopole and the ground plane was modified. The node was modified to model a 50 Ω impedance feed-wire serving as a matching node for the antenna instead of using a short node as described in the second method above. The node is termed *feed-node.* In the simulation space, the feed-node was represented in terms of its electric conductivity. This was achieved by setting the impedance, Z_w of the feed-wire, which in this case is 50 Ω to be equal to the ratio of the resistivity of the wire, ρ_w, to the cross Sectional area A_w of the wire. Using (5.1) – (5.4),

the equivalent conductivity for the 50 Ω feed-wire of length l_w and radius r_w was calculated.

$$Z_w = \frac{\rho l_w}{A_w} \tag{5.1}$$

where

$$A_w = \pi r_w^2 \tag{5.2}$$

The electric conductivity σ_w is inversely proportional to ρ_w and it is given as:

$$\sigma_w = 1/\rho_w \tag{5.3}$$

Substituting for ρ_w and A_w gives

$$\sigma_w = \frac{l_w}{A_w Z_w} = \frac{l_w}{\pi r_w^2 Z_w} \tag{5.4}$$

The optimised matching node, the feed-node, now serves as the feed-wire having 50 Ω resistance and conductivity, σ_w. Current was injected at the base of the antenna by exciting the *H*-field around the optimised node as shown in Fig. 5.2.

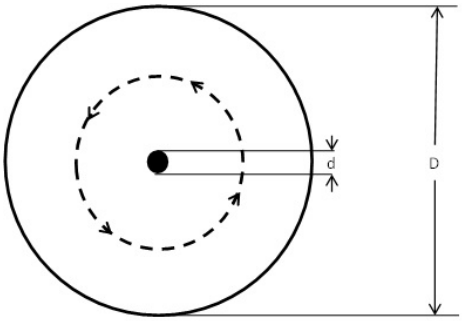

Fig. 5.2: Antenna excitation (H-field in dotted arrow, $d = 2r_w$ and D is the simulation space diameter).

The simulated results for the modelled cylindrical dipole and the monopole antennas are presented in Sections 5.2.1.1 and 5.2.1.2 respectively.

5.2.2 SIMULATED RESULTS FOR THE CYLINDRICAL MONOPOLE AND THE CYLINDRICAL DIPOLE

The simulated results for the modelled cylindrical dipole are presented in this Section. The radiation frequency of the antenna is the main antenna characteristics produced by the TLS. The electric fields in the two simulations were observed at a location adjacent to the feed point, 100 nodes away from the antenna. The electric field in the simulation space for the monopole antenna is shown in Fig. 5.3. The electric field response shows that the signal gradually dampens and tends to zero with time. These results suggest that the boundary is correctly implemented because this is the kind of response theoretically expected from a simulation space terminated by an absorbing boundary.

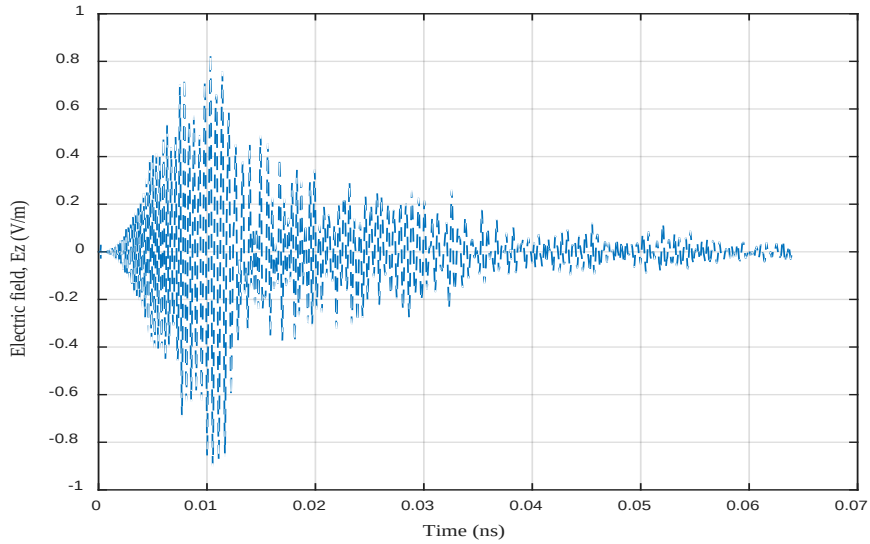

Fig. 5.3: The simulated electric field for the cylindrical monopole after 40960 iterations (observed at node r, θ, z =100, 1, 75).

For easy comparison, the magnitude of the electric field in frequency domain was normalised to the highest value in the simulation result. It can be deduced from Fig. 5.4 that the simulated radiated frequencies are as theoretically expected. There is a fundamental resonant frequency of 2 GHz for $\lambda/4$ and a secondary resonance around 6 GHz, which is an odd multiple of the fundamental frequency ($3\lambda/4$), as expected of a typical monopole. These results show that the model has been correctly implemented in TLM. However, for a monopole/dipole of 1.5 mm radius, a narrow bandwidth is theoretically expected while the bandwidths of the simulated operating frequencies are wide. In the simulation of the monopole, two approaches were considered in order to check if the position of the antenna in the simulation space affects the simulated results and to determine the best position for the radiating structure in the simulation space. The first approach was to place the radiating structure and the ground plane at the centre of the simulation space and the second approach was to place the radiating structure and the ground plane at the base of the simulation space. The results obtained for both position were found to be very close when

compared. For the remaining part of this thesis, the base position was the chosen method for all simulations.

To verify the theoretical expectation that the monopole on an infinite ground plane should radiate at the same frequency as the dipole twice its length, the frequency responses of the simulated antennas were compared as shown in Fig. 5.4. It was observed that the simulated electric field followed the same trend of radiating frequencies except for the difference in amplitude and a small shift in phase at higher frequencies.

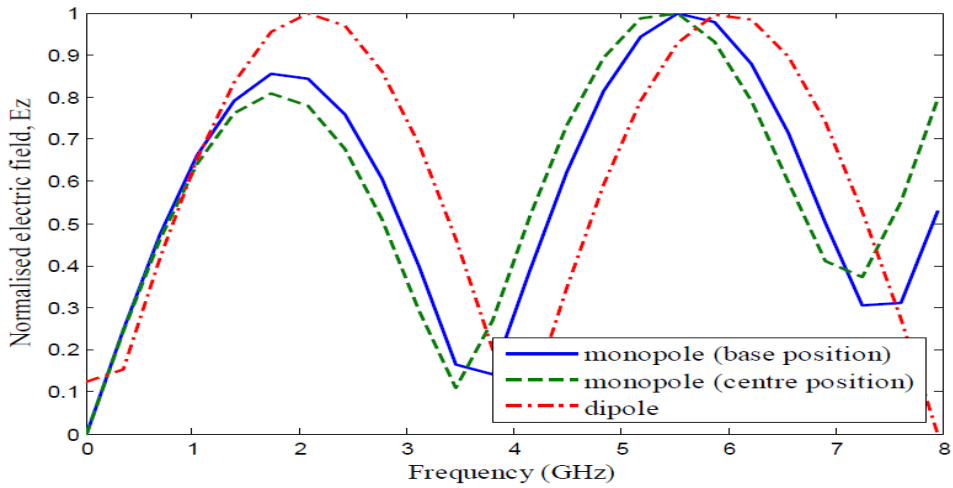

Fig. 5.4: Comparison of the normalised electric field for the cylindrical monopole and the dipole antennas after 16384 iterations.

5.2.3 Simulation of Conical Monopole Antenna and Simulated Results

For a resonant frequency of 2 GHz, the length of the cylindrical antenna was set at $\lambda/4$ = 37.5 mm and the antenna half-angle 45°. The antenna was modelled to stand on a circular ground plane of radius 1λ. Both the antenna and the ground plane were simulated as copper. The schematic diagram of the simulated cone is shown in Fig. 5.5. The conical antenna was simulated in the same computational cylindrical modelling space as the dipole and

monopole in Section 5.2.1. The simulation mesh view for the conical monopole in the *rz*-plane is as shown in Fig. 5.6. With the application of symmetry, only one slice of the cone was simulated. Therefore, in order to aid the visualisation of the cone in the mesh, the image was mirrored around the θ axis and at the centre symmetry on *r*. The image has also been zoomed in from its original size.

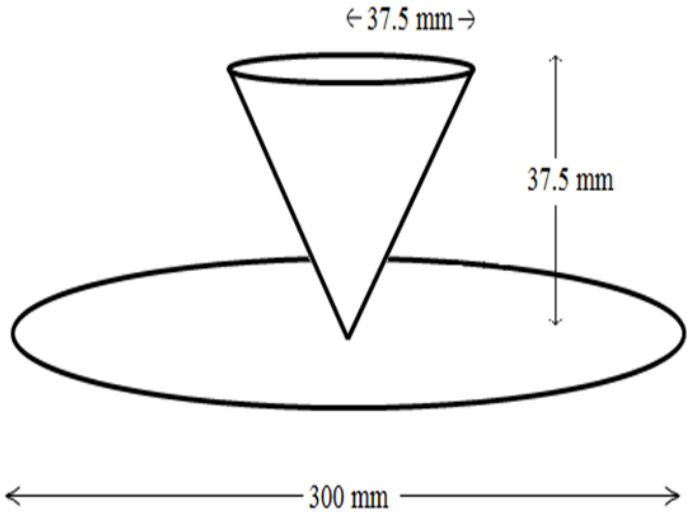

Fig. 5.5: The schematic diagram of the simulated conical monopole.

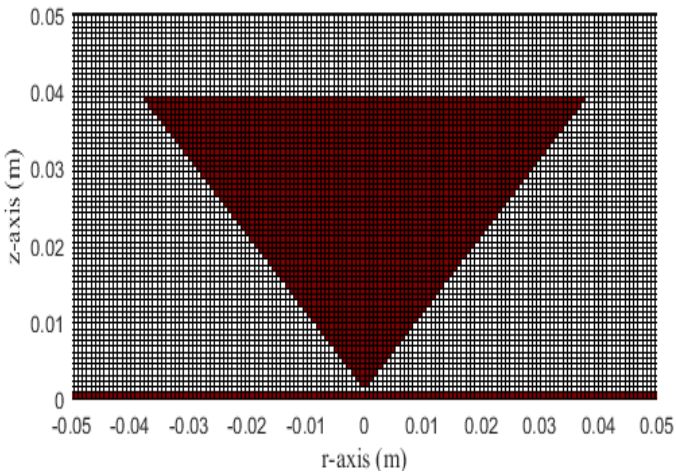

Fig. 5.6: The simulated conical monopole meshed in TLM with red indicating the copper and meshed background representing the open space.

The H-field was excited around the θ-axis as described in Section 5.2.1 and the electric field propagation is along the z-axis and absorbing boundary termination was applied to the end of the modelling space. The simulated electric field for the conical structure is shown in Fig. 5.7. It can be deduced from the figure that the simulated conical antenna has a broad bandwidth compared to the monopole and dipole output presented in Fig. 5.4.

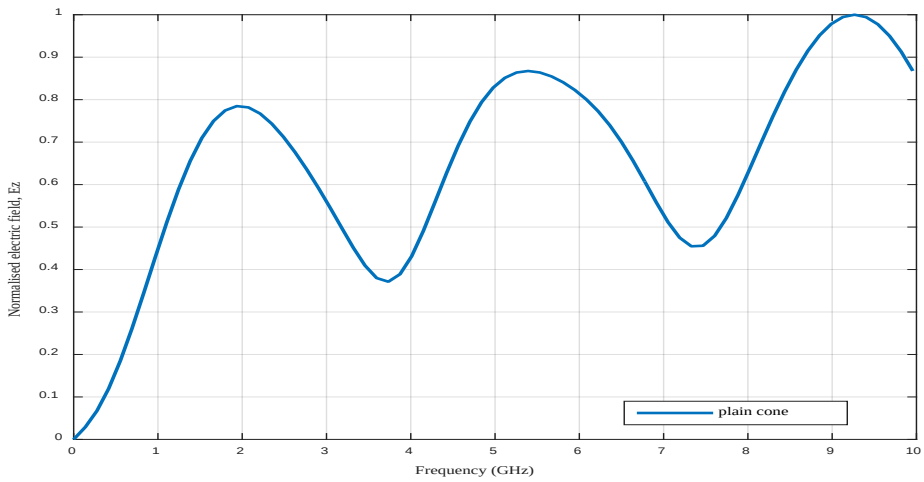

Fig. 5.7: Normalised simulated electric field for the conical antenna after 40960 iterations.

5.3 EXPERIMENTAL RESULTS AND DISCUSSIONS

Since the simulated results were closely in-line with theoretical predictions, the antennas were fabricated and measured to further validate the simulated results. In this Section, the results of these measurements made on prototype monopole antennas are discussed. The antennas were built using solid copper while the ground planes were constructed from FR4 with single-sided copper metallisation. The diameter of the ground plane for the two prototype antennas was 300 mm. Both antennas were 37.5 mm high/long. The cylindrical monopole had a 3-mm diameter while the cone had a 75 mm diameter circular base at 45° half-angle. A tiny hole was drilled to the base of the cone in order to connect the 50 Ω SMA connector. Pictures of the fabricated antennas are shown in Fig. 5.8 and Fig. 5.9.

Fig. 5.8: Picture of the fabricated prototype cylindrical monopole antenna.

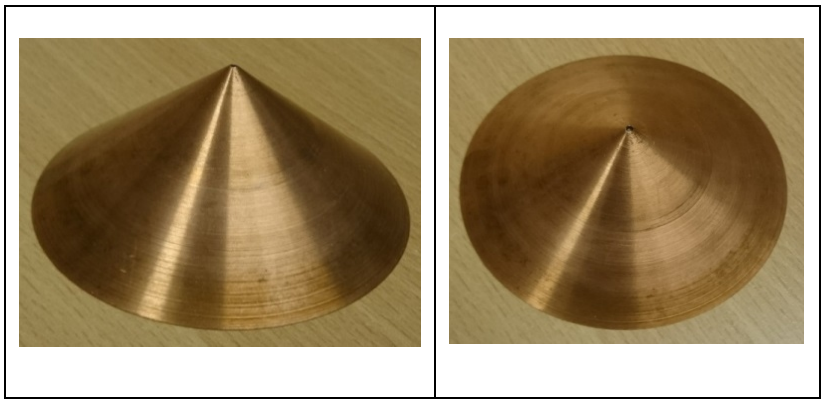

Fig. 5.9: Pictures of the fabricated prototype conical monopole antennas.

For the measurement of the reflection coefficient (S_{11}) of the antennas, an Anristsu 37397D VNA analyser calibrated to measure up to 12 GHz was used. The S_{11} results give a general overview of the antenna's behaviour. The analyser was connected to the coaxial feed, which was connected to the ground plane. The antennas were mounted on a stand during measurements as shown in Fig. 5.10 and Fig. 5.11. To support the weight of the conical antenna on the measuring equipment, a square shaped Styrofoam with a conical-shaped hollow middle was built and fastened to the ground plane with a nylon strip and bolt as shown in Fig. 5.13. The connection of the SMA feed to the cone was carefully set to ensure good contact.

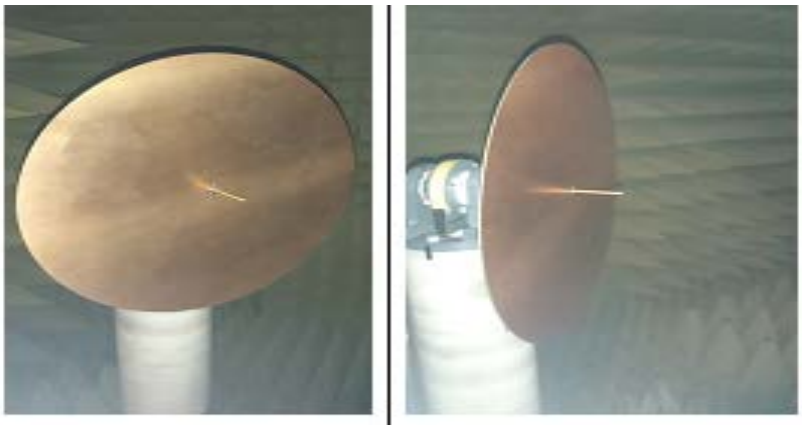

Fig. 5.10: Measurement set-up for the cylindrical monopole antenna.

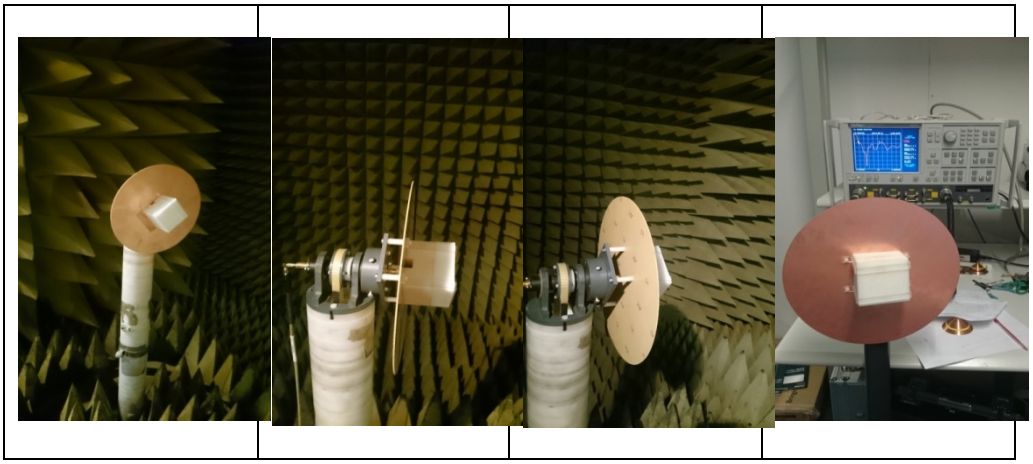

Fig. 5.11: Measurement set-up for the conical monopole antenna.

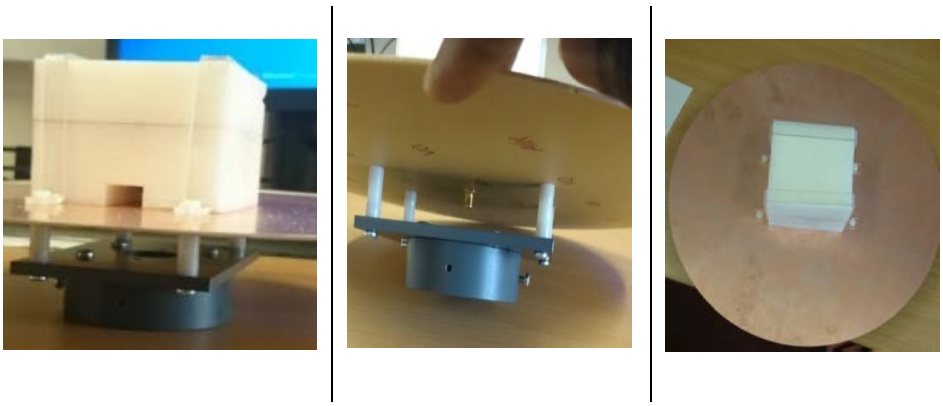

Fig. 5.12: Support structure for the cone antenna measurement.

The measured parameter in the experiment is S_{11} parameter while the simulated parameter is the electric field. It was observed that the simulated electric field peaks at the point where the crest of the S_{11} parameter lies. Therefore, to compare the simulation results to the experimental results, the peaks and the crests of the two results are compared. The measured S_{11} parameter for the cylindrical monopole antenna prototype is as shown in Fig. 5.14. The fabricated antenna resonates at 1.98 GHz and 5.8 GHz, which are very close to both the theoretical and simulated predictions.

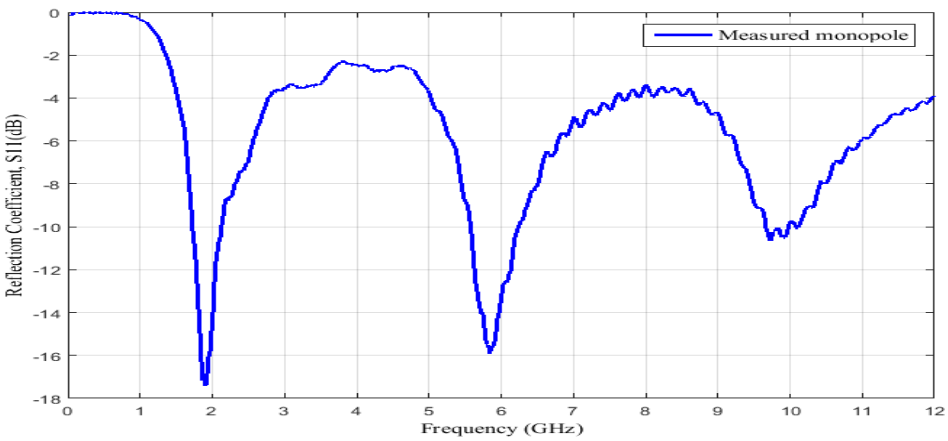

Fig. 5.13: S_{11} parameter for the prototype cylindrical monopole antenna.

The S_{11} parameter of the prototype conical monopole antenna is as shown in Fig. 5.15. Compared to the ultra-wide bandwidth predicted by the simulated

result, the prototype cone demonstrated a broad bandwidth from 1.10 – 6.41 GHz at -10 dB. Notwithstanding, at -9.5 dB, the antenna has an ultra-wide bandwidth over the frequency range 1.10 – 12.0 GHz, which is very good .

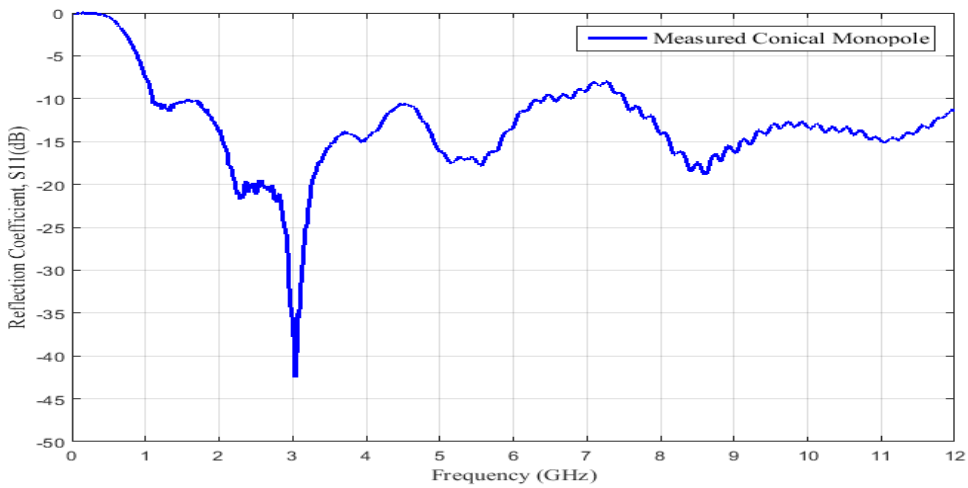

Fig. 5.14: Measured S_{11} parameter for the prototype conical monopole.

It was also observed that although the antenna's vertical height was calculated to be 37.5 mm for the 2 GHz fundamental frequency, the antenna started radiating below -10 dB at 1.10 GHz. This is in line with theoretical expectations because the lowest resonant frequency of an antenna, which is 1.10 GHz in this case, is determined by the longest length on the antenna structure. The longest length on the conical antenna is not the vertical height but the length of the slant edge of the cone, which is calculated as

$$Slant\ height = \frac{vertical\ height}{\sin(half\ cone\ angle)} = \frac{37.5}{\sin(45°)} = 53.03\ mm$$

With the length of 53.03 mm, the antenna is theoretically expected to radiate at 1.41 GHz frequency. However, the top of the solid cone formed a continuous path for the propagating wave and is expected to have some effect on the frequency.

5.4 CONCLUSIONS

The Transmission Line Simulator (TLS), developed for this research has been used successfully for the simulation of microwave cavity resonator in Chapter 4. In this Chapter, the application of the solver is extended to the modelling of axisymmetric radiating structures. The structures simulated are a cylindrical dipole, a cylindrical monopole and the conical monopole antennas. The simulated results were compared with the analytical results and were found to be in reasonable agreement.

To validate the simulated results, prototype cylindrical monopole and conical monopole antennas were fabricated and measured. The measured results compared well with the theoretical and simulated results.

Having established the effectiveness of the TLS in modelling axisymmetric radiating structure, the next step is to apply the simulator to a more advanced application. In Chapter 6, the solver is applied to the modelling of radial slots on a solid cone antenna and the effects of these slots on the antenna properties are investigated.

CHAPTER 6

MODELLING OF THE SLOTTED CONE

As mentioned in Chapter 5, the finite nature of the mono-cone antenna introduces end reflections and standing waves, which affect the bandwidth of the antenna [143]. One common method used in improving the bandwidth of conical antennas is modifying the top of the antenna such that it has a spherical surface [146]. Examples of such type of designs that have been used in practice are sphere-loading [147], teardrop (defined as the combination of a finite cone and a sphere [143]), the merge of a cone with a circular cylinder [133] and adding a hemispherical dome to the top of the cone [148]. These loading methods improve matching and thus reduce the amount of reflected energy. Sphere loading increases the electrical length of the antennas as well.

Other modifications that bring improvement to the conical antenna include dielectric loading and resistive loading. Dielectric loading increases the electrical length of the antenna but has a negative side effect of loading the near field of the antenna affecting the characteristic impedance of the antenna. Hallén [149] researched into an antenna with quasi-distributed capacitive loading and concluded that it has excellent broadband characteristics. Rao et al. [150] worked on an antennas with exponentially tapered capacitive loading and concluded that this also had good broadband characteristic. Palud et al. [151] and Gentili et al. [152] also researched into

the effect of adding parasitic elements and a capacitive loading ring to the antenna and came to a similar conclusion.

Resistive loading of the antenna, on the other hand, alters the current distribution along the antenna length thereby reducing the reflections from the ends of the antenna [153]. It reduces the distortion of the radiation from the open end and feed region of the antenna. Resistive antennas are an interesting concept but have a major disadvantage of low efficiency. This deficiency does not occur in reactive loading [153]. King and Wu [154] presented theoretical analysis of a resistive antenna with constant loading. Shen [155] experimentally analysed the resistive antenna and it was reported that his results were in agreement with King and Wu to some extent. More recently, Maloney and Smith [139] placed a continuous resistive material along the antenna length to produce an exact replica of the input pulse as observed on a conical antenna and conducted an experimental study using the discrete version of the resistive profile proposed by King and Wu [154] and obtained results that were in good agreement with the theoretical work.

Another method that has been used to improve the bandwidth of conical antennas is the alteration of the ground plane. Mulenga and Flint [144] researched into modifying the ground plane to achieve improved broadband antenna performance. They investigated the effect of using a partially corrugated reflector instead of the normal Perfect Electric Conductor (PEC) reflector on the radiation pattern of the conical antenna and detected that the corrugated reflector gives a more stable radiation pattern over a wide frequency band than the conventional PEC.

Oleksiy [156] carried out research into improving the radiation pattern of a bi-conical antenna by reducing its side lobes using radial slots. He achieved this by cutting quarter-wavelength deep annular slot out of the conical

radiating structure. The slots were also reported to have brought about a reduction in the antenna diameter by a factor of two. The bandwidth was however traded off for this size improvement to be achieved. Best [157] also researched into the effect of cutting slots into the body of open conical antenna but he worked on an open cone antenna. Doroshenko et al. are other researchers who have worked on the use of slot to enhance the performance of conical antenna characteristics [158].

Based on the work of Best [157], Mulenga [159] explored the use of single and multiple slots to improve the radiation pattern of conical antenna. It was reported that the behaviour of conical antennas with cut out slots was complex and slots on a 3-D conical antenna brought about disruption to the TEM mode of the broadband antenna. It was also reported that slots introduce several anti-resonant frequencies in the operating band.

In this Chapter, slotted cone antennas are simulated using the developed Transmission Line Modelling Solver. The purpose of these simulations is to check the effectiveness of the developed code in simulating slots because it has been reported that slots can be efficiently represented in TLM [4]**.** The simulated results of slotted conical antennas are presented and compared with the analytical results obtained using the equations proposed by Mulenga [159]. The possibilities of using dielectric loaded slots to improve the characteristics of the conical antenna was also investigated and reported here. The simulation procedures and the results obtained for the slotted cones are discussed in Section 6.2, simulated results showing the effect of the dielectric load on the conical antenna are presented in Section 6.3 and measured results to validate the simulated results are presented in Section 6.4.

6.1 SLOTTED-CONE ANTENNA SIMULATION AND SIMULATED RESULTS

In this Section, simulated results for cones having annular slots are discussed. Similar to the cone simulated in Section 5.2.1, the vertical length of all simulated slotted-cone antennas were set at λ/4 (37.5 mm) for 2 GHz frequency and the antenna half-angle set at 45°. The antennas were placed on a circular ground plane of 2λ diameter. These dimensions were chosen in order to be able to compare simulated results of the slotted antenna with the already simulated plain cone to determine the effect of the slot(s) on the conical monopole antenna parameters. Both the antenna and the ground plane were simulated as copper.

A solid cone antenna with a slot (see Fig. 6.1) is theoretically expected to generate anti-resonant frequency at a certain frequency band [159]. The expected anti-resonant frequency/trap frequency (f_s) and the position of the slot on the cone, slot-position (h_s) that would allow its occurrence are analytically calculated as [159]:

$$f_s = \frac{c}{2\pi s_d \sqrt{\varepsilon_r \mu_r}} \tag{6.1}$$

$$h_s = \frac{c}{4 f_s} \tag{6.2}$$

where $c = \frac{1}{\sqrt{\varepsilon_0 \mu_0}}$ is the speed of light in free space; ε_0 and μ_0 are the permittivity and the permeability of free space respectively; ε_r and μ_r are the relative permittivity and the relative permeability of material in the slot respectively and s_d is the depth of the slot.

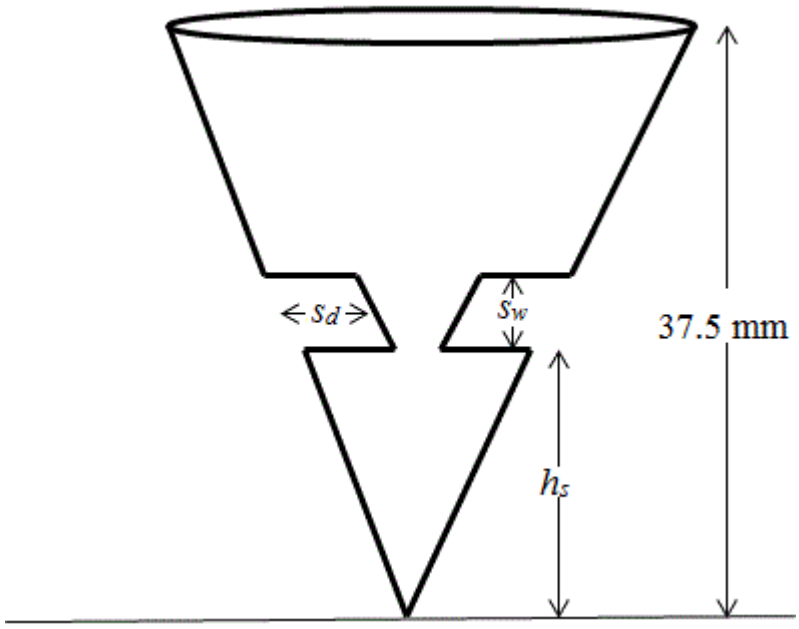

Fig. 6.1: The schematic diagram of single-slotted cone antenna.

In order to verify the accuracy of equations (6.1) and (6.2) for the calculation of f_s, a benchmark simulation was conducted for a slotted cone with cone-height = 37.5 mm, slot-width, s_w = 3 mm, s_d = 15 mm. Equation (6.1) gives $f_s = 3.18$ GHz and $h_s = 23.58$ mm. Since the two equations were yet to be verified, another simulation was run in CST for validation of the simulated result. The two simulated results were compared in Table 6.1. For the selected parameters, the simulation results compared to the theoretical results with a 21% difference in both TLS and CST. The difference in the analytical result compared to the simulated results could be as a result of the selected value of s_w, which is not included in the analytical equation but was reported to be very small. For accurate comparison of simulated results with the analytical solutions, the calculated values from the equations had to be corrected for this error. However, the equation gives a rough estimate of the frequency range for the occurrence of trap frequencies, which served as a useful guide.

Table 6.1: Comparison of benchmark analytical result to simulation results

	Frequency (GHz)
Theory	3.18
Simulation by CST	3.86
Simulation by TLS	3.85
s_w = 3 mm, s_d = 15 mm, h_s = 23.58 mm	

Four parametric studies showing the effect of the slots on the performance of the cone were carried out. The study includes the effect of the slot's-position, depth, width and multiple slots. The first three studies, *parametric test 1*, *2* and *3*, examined the effects of the slot's location depth and width, on the operating frequency of the antenna respectively. The fourth study *parametric test 4* checked the effects of two slots on the cone antenna parameters and the last test. Another simulation was performed to determine the effect of loading the slot with dielectric material of $\varepsilon_r > 1$ on the resonant frequency.

6.1.1 PARAMETRIC TEST 1 – THE LOCATION TEST

This parametric test was conducted to verify the effect of the slot's location on the operating frequency of a conical antenna and the results are discussed here using two simulations. An annular slot of $s_w = 1.5$ mm , $s_d = 15$ mm was positioned at two different locations on the cone and their simulated results compared. For the first simulation referred to as *slotted cone antenna 1a*, $h_s = 18.75$ mm and for the second simulation referred to as *slotted cone antenna 1b*, $h_s =$ 26.25 mm as shown in Fig. 6.2(a) and (b) respectively. The *rz*-view of the meshes used for the two single-slotted cones are shown in Fig. 6.3. With the application of symmetry, only one slice of the cone was simulated.

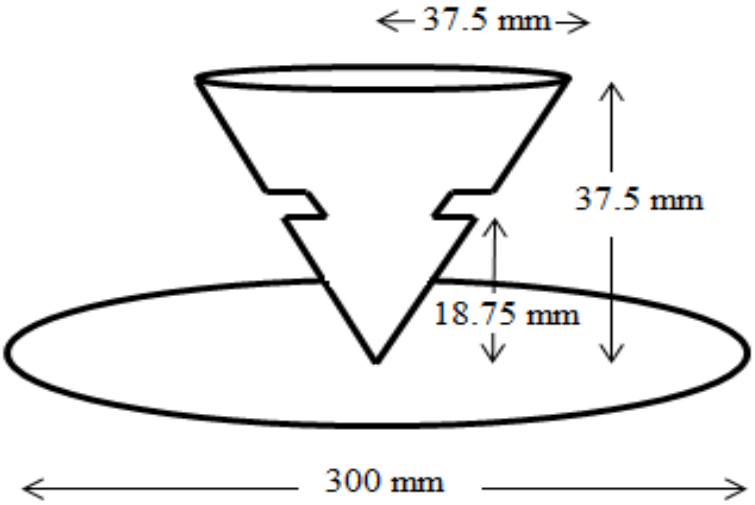

(a) Slotted-cone antenna 1a: $h_s = 18.75$ mm , $s_d = 15$ mm

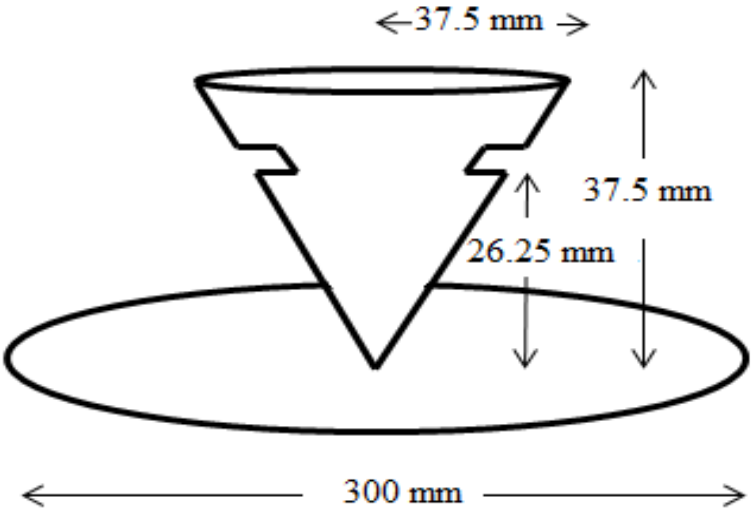

(b) Slotted-cone antenna 1b: $h_s = 26.25$ mm , $s_d = 15$ mm

Fig. 6.2: The schematic diagrams of simulated single-slotted cone antennas for the location parametric test, cone angle = 45°.

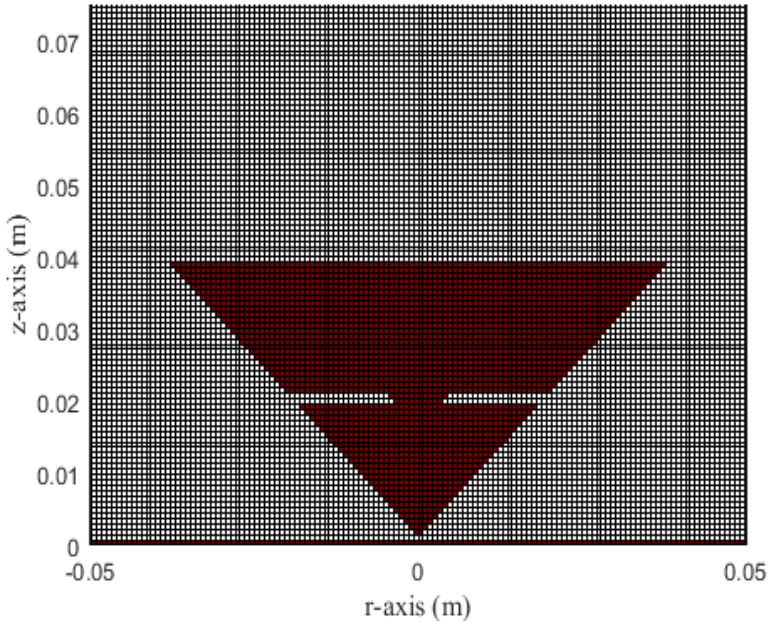

(a) slotted-cone antenna 1a: $h_s = 18.75$ mm , $s_d = 15$ mm

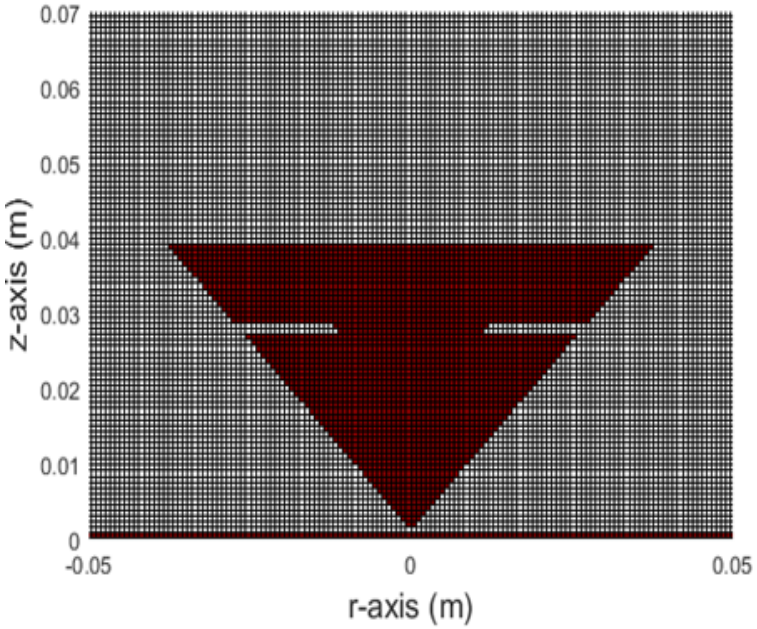

(b) slotted-cone antenna 1b: $h_s = 26.25$ mm , $s_d = 15$ mm

Fig. 6.3: The rz-view of the mesh used for the simulation of the single-slotted cone antennas for location parametric test.

The result obtained from the simulated plain cone discussed in Section 5.2.3 is used as reference for the results of the slotted cones simulated in this Section. The simulated plain cone was broadband in nature as shown in Fig. 5.18. Fig. 6.4 shows the normalised electric field as a function of frequency for the two slotted-cone antennas.

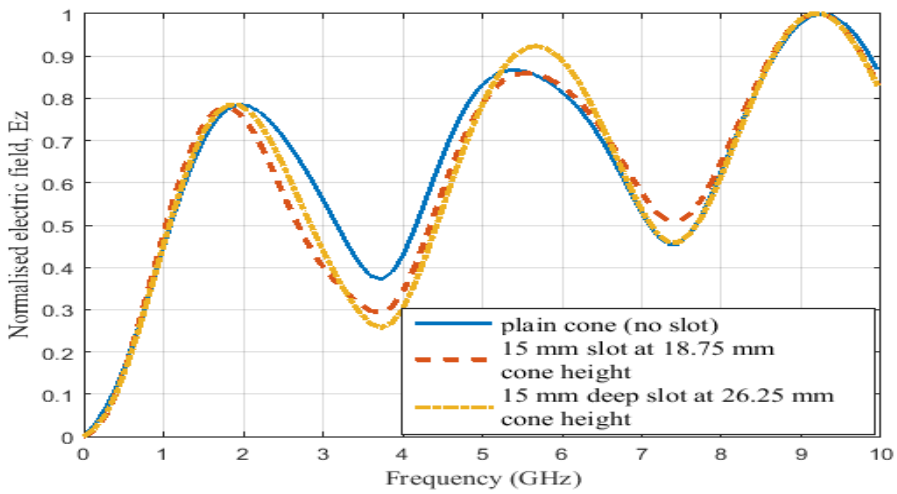

Fig. 6.4: Comparison of the normalised simulated electric field for plain cone (—) slotted-cone antenna 1a (---) and slotted-cone antenna 1b (-•-).

As shown in Fig. 6.4, the frequencies of the slotted-cone antennas followed the same trend as that of the plain cone. However, the insertion of the slot with s_w = 15 mm affected the magnitude of the electric field simulated for the slotted-cone antennas by introducing a deeper crest, which signify an anti-resonant frequency, at 3.73 GHz. The presence of the anti-resonant frequency produced a trap within the broad bandwidth of the plain cone. It can be deduced from Fig. 6.4 that despite the fact that the two slots were not positioned at the same location on the cone, both produced anti-resonant frequency about the same point. There was a little shift towards the lower frequency observed in the trap produced by the slot located at 18.75 mm cone height compared to that of the slot located at 26.25 mm cone height. The slot position could be responsible for this shift, which means that it is

important to put into consideration the position of the slot on the cone in order to obtain accurate results. This is in agreement with the theoretical prediction. The slot located closer to the top of the cone at 26.25 mm cone height was also observed to produce a stronger trap compared to the one placed at the mid-length of the cone (18.75 mm cone-height).

6.1.2 PARAMETRIC TEST 2 – THE DEPTH TEST

In order to evaluate the impact of s_d on the operating frequencies of the slotted-cone antennas, two different slot-depths were simulated and the results obtained compared. For the first simulation, the s_d = 7.5 mm and for the second simulation, s_d = 15 mm. s_w = 1.5 mm and h_s = 18.75 mm for the two antennas. The simulated electric field at different frequencies for the two slot-depths considered are compared with that of the cone with no slot in Fig. 6.5.

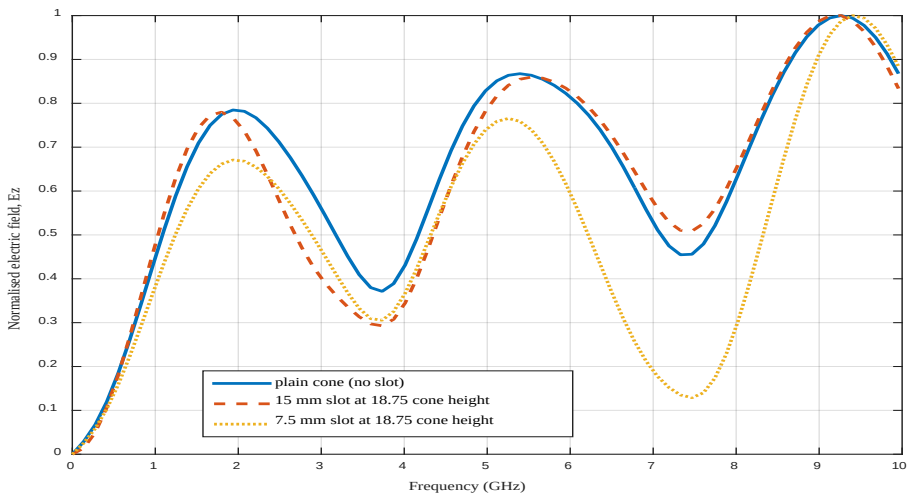

Fig. 6.5: Comparison of the simulated electric field of the plain cone antenna (—) with the slotted-cone antennas with s_d = 7.5 mm (---) and s_d = 15 mm (•••) at h_s = 18.75 mm.

It was observed from the results of the depth variation presented in Fig. 6.5 that the anti-resonance frequencies produced by the two slots considered are

inversely proportional to the depth of the slots as theoretically predicted. The deeper slot produced a trap at a lower frequency while the relatively shallow slot produced a trap at a higher frequency. It was also observed that the higher frequency was strongly affected by the slot as it produced a stronger trap compared to the lower frequency. This is in line with theoretical expectations. It can be deduced from these results that the s_d can be used to determine what frequency is radiated and which one is blocked/trapped within the broadband frequency range of the host antenna, the plain cone antenna.

6.1.3 PARAMETRIC TEST 3 – THE WIDTH TEST

In order to highlight the effect of the slot-width on the operating frequencies of the slotted-cone antennas, parametric simulations with varying width was conducted. While varying the widths of the slot, h_s was fixed at 26.25 mm and s_d was fixed at 15 mm. The results of four different slot-widths are compared with that of the ordinary plain cone in Fig. 6.6.

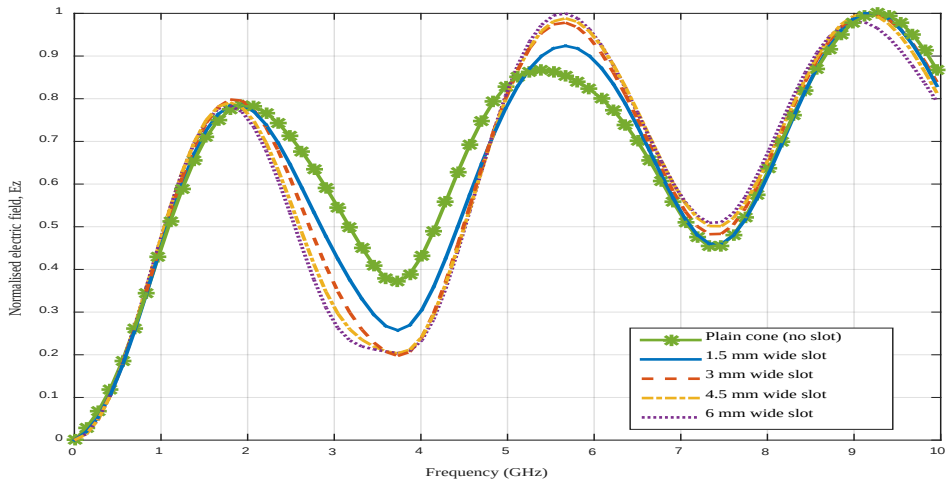

Fig. 6.6: Comparison of the simulated normalised electric field for single slotted-cones with different slot-widths.

It could be inferred from the results shown in Fig. 6.6 that the variation of the slot-width affected the bandwidth of the anti-resonance created by the slots in direct proportion. Contrary to the theoretical expectation, it was observed that the fundamental frequencies of the slotted cone did not significantly shift towards lower values but those of the anti-resonant frequencies did with increases in the slot width. This shift widened the bandwidths of the anti-resonant frequencies at the expense of the bandwidth of the fundamental frequency. It was observed that despite the difference in the slot-widths of the slotted-cone antennas, their frequencies followed the same trend by showing anti-resonances at approximately the same frequency. These results show that the slot-depth has significant impact in determining the position of the anti-resonant frequency as suggested by equation (6.1) while the slot-width affects the bandwidth of the trap. It can also be deduced from these results that a well calculated slot on a solid cone antenna can be used to suppress any frequency range that is not required in a wideband application. This also means that if the antenna is to be conditioned for frequency rejection or selective frequency radiation, the width of the slot can be used to adjust the bandwidth of the rejected frequency while the frequency to be blocked can be selected by varying the depth of the slot. These results were considered as a guide in the choice of the slot-width for the prototype antennas discussed in Section 6.2.

6.1.4 PARAMETRIC TEST 4 – DOUBLE SLOTS

The tests conducted on slotted-cone antennas in Section 6.1.1 – 6.1.3 involved the use of a single slot on the cone. To check the effect of multiple slots on the operating frequency of the cone antenna, two annular slots were placed on the cone as discussed in this Section. Two slots were positioned at heights h_{s1} = 18.75 mm and h_{s2} = 26.25 mm on the cone as shown Fig. 6.6 and this particular slotted-cone is referred to as a *double-slotted cone antenna*.

Two variants of the double–slotted cone antenna were considered: *double-slotted antenna 4a* and *double-slotted antenna 4b*. In the double-slotted antenna 4a test, s_d = 15 mm for the two slots. In the double-slotted antenna 4b test, a slot with s_d = 7.5 mm was positioned at h_{s1} = 18.75 mm and slot with s_d = 15 mm was positioned at h_{s2} = 26.25 mm. The s_w = 1.5 mm was maintained for both slots. The schematic diagram of the double slotted cone and the *rz*-view of the mesh used for the simulation are shown in Fig. 6.7 and Fig. 6.8 respectively. The simulated operating frequency for slotted-cone antenna 4a and 4b are compared with that of the plain cone in Fig. 6.9.

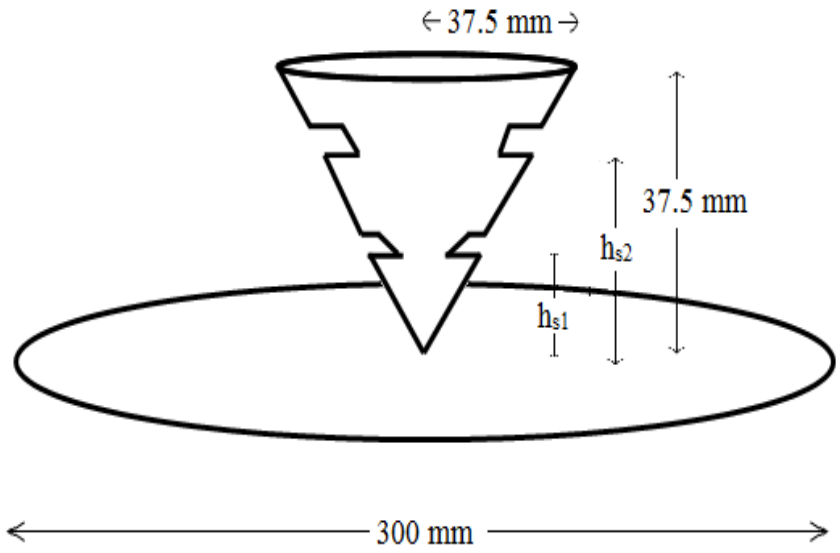

Fig. 6.7: The schematic diagram of the simulated double-slotted cone antenna.

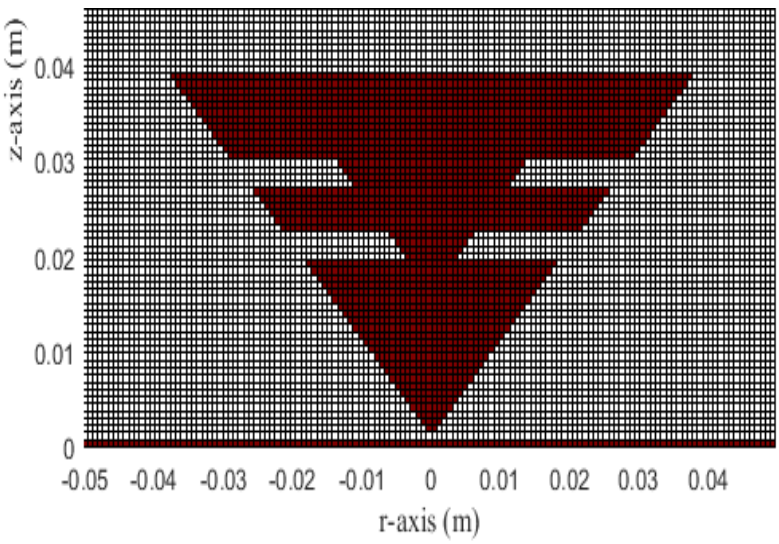

Fig. 6.8: The rz-view of the mesh used for the simulation of the double-slotted cone antennas.

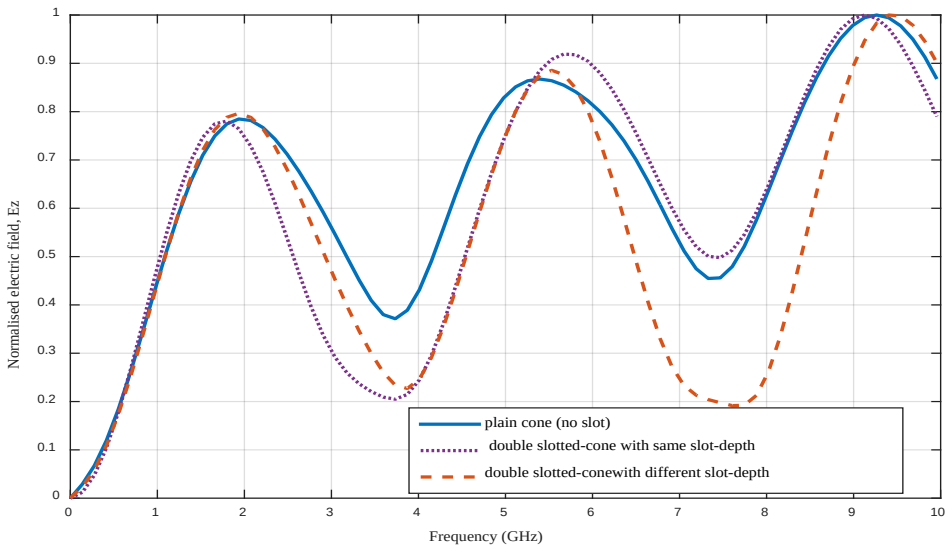

Fig. 6.9: Comparison of the simulated normalised electric field for the plain cone (—) and the double-slotted cone antennas.

Based on the analytical results and previous response of the 15 mm deep slot, positioned at 26.25 mm cone-height, it was expected that the double-slotted-cone would generate a trap frequency band about 3.73 GHz. The

simulation results confirmed this expectation by creating anti-resonant frequencies aligning within the predicted range of frequency range (3.31 - 3.99 GHz). Despite been located at different positions on the cone, there was only one noticeable trap produced by the two slots. However, the bandwidth of the trap frequency created was wider than that of a single slot. The width of the trap frequency was observed to be similar to the bandwidth produced by the single slot with 3 mm width. It can therefore be deduced that the width of the two slots had a cumulative effect on the result, producing an equivalent effect of 3 mm width. The trap created by the two slots is stronger than that of a single slot as shown in Fig. 6.9 despite the fact that the width was maintained at 1.5 mm depth.

It can be deduced from Fig. 6.9, that the double-slotted antenna 4b produced two clear anti-resonant frequencies associated with the two different slot-depths. The 15 mm deep slot produced the lower anti-resonant frequency while the 7.5 mm deep slot was responsible for the higher anti-resonant frequency. In the case of double-slotted antenna 4a, the trap frequency only occurred between 3.31 – 3.99 GHz confirming the fact that the slot-depth has great impact on the operating frequency of a slotted antenna. It was also observed that the double slotted-antenna produced stronger anti-resonance with wider bandwidth compared to their single slot counterparts showing the effect of the cumulative slot-width.

6.1.5 DIELECTRIC LOADED SLOTTED-CONE

The effect of loading the slots with a dielectric material of permittivity value $\varepsilon_r = 2.5$ is discussed here. A slotted cone with s_w = 3 mm, s_d = 15 mm and h_s = 26.25 mm was used for this test. The slot was filled with the dielectric material as shown in Fig. 6.10 and the simulated results are compared with the simulated results for the single-slotted cone without dielectric load in Fig. 6.11.

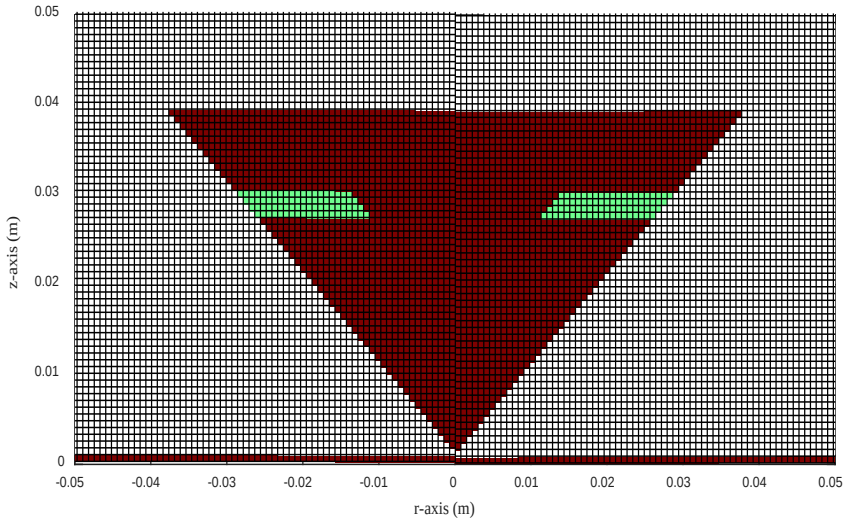

Fig. 6.10: The rz-view of the mesh used for the simulation of the dielectric loaded slotted-cone antenna.

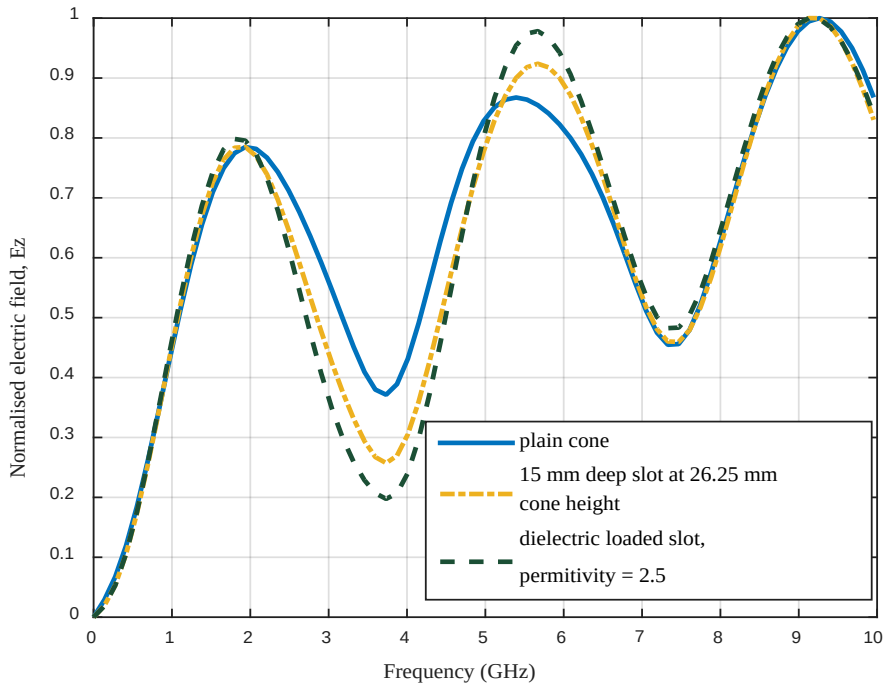

Fig. 6.11: Comparison of the normalised simulated electric field for the dielectric loaded single-slotted cone antenna (h_s = 26.25 mm, s_w = 3 mm, s_d = 15 mm) with plain cone (—) and unloaded double-slotted antenna (---).

Fig. 6.11 confirmed the theoretical expectation that the dielectric load would increase the electrical length of the slot and shift the trap frequencies of the double-slotted cone to lower values. A certain level of trap control may be possible with the application of the dielectric load to the slot but an extended study would be required to ascertain these effects on the characteristics of the conical antenna.

6.2 EXPERIMENTAL RESULTS AND DISCUSSIONS

Prototypes of some of the slotted-cone monopole antennas simulated in Section 6.1 were fabricated and the measured results are presented and discussed in this Section. The purpose of these measurements is to validate the simulated results obtained in Section 6.1. The antennas were built using solid copper with the same specifications used for the fabrication of the plain cone discussed in Section 5.3. This was to allow for easy comparison of the cone performances before and after incorporating the slot. Three variants of the slotted-cone antenna prototype were fabricated.

The width of all the slots was chosen to be 3 mm. This choice was based on results obtained in Section 6.1.3, which showed that the occurrence of an anti-resonant frequency became more evident with slots of widths $\geq$ 3 mm. The choice of 3 mm was also considered over the 1.5 mm width to facilitate easy and more accurate machining of the slot without compromising the resonance of the slotted antennas.

The first annular slot was cut 7.5 mm deep at 26.25 mm cone-height (slotted-cone antenna 1, see Fig. 6.12). The second slot was cut 15 mm deep at the same cone-height as the first (slotted-cone antenna 2, see Fig. 6.14). This example was used to evaluate the impact of varying the slot depth on the performance of the cone antenna while keeping the slot-width constant. There were two annular slots on the third cone (slotted-cone antenna 3, see Fig. 6.15). The first slot on slotted-cone antenna 3 was 15 mm deep positioned at 26.25 mm cone-height while the second slot was 7.5 mm deep and it was positioned at 18.75 mm cone height.

The measurement setting applied in Section 5.3 was adopted for all the measurements. The S_{11} parameters were measured using the Anritsu 37397D VNA analyser calibrated to measure up to 12 GHz frequency.

6.2.1 SLOTTED-CONE ANTENNA 1

The measured results of the prototype antenna with annular slot of 7.5 mm deep at 26.25 mm cone-height is presented and discussed here. The picture of the fabricated cone with the slot machined into it is shown in Fig. 6.12 and the measured S_{11} parameter of the prototype plain cone antenna discussed in Section 5.3 is compared to that of the slotted cone antenna 1 in Fig. 6.13.

As predicted in the simulation results, for slot cone with s_d = 7.5 mm, the measured result presented a trap between 6.04 - 8.68 GHz with S_{11} above -6 dB. The slotted-cone and the plain cone have similar operating frequency patterns but effect of the slot can be seen on the bandwidth of the antenna's radiation frequencies. There was another trap at 3.60 - 6.04 GHz in the measured result which was not predicted by either the analytical or the simulation method.

Fig. 6.12: Prototype cone with s_d = 7.5 mm and h_s = 26.25 mm.

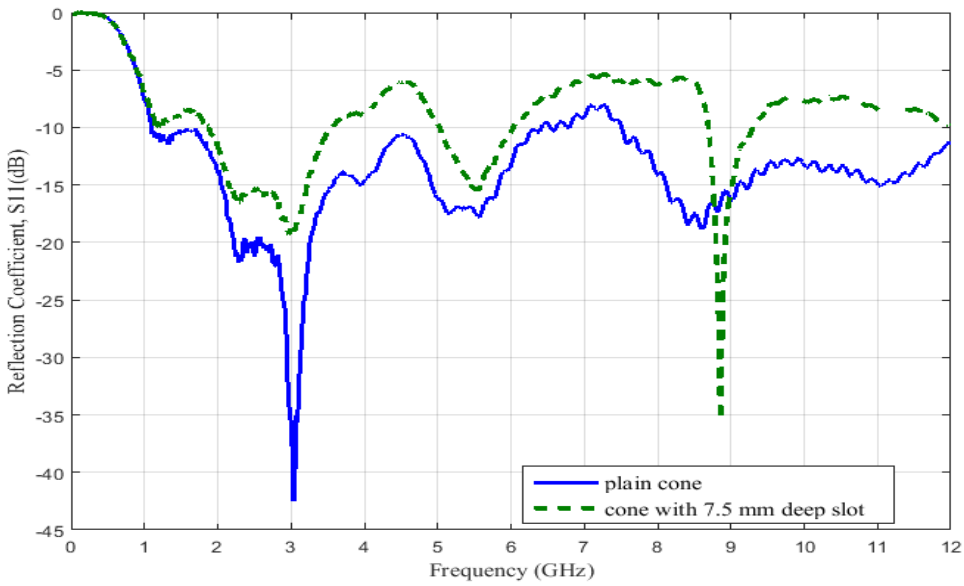

Fig. 6.13: Comparison of the measured S_{11} for plain cone (—) and cone with slot (- - -): s_d = 7.5 mm and h_s = 26.25 mm.

The trap divides the wide bandwidth of the plain cone antenna creating three narrower bandwidths with the application of the 7.5 mm deep slot. It was observed that the slot also has some effect on the matching of the antenna. Although still very good at $S_{11} \leq 15$ dB, the antenna impedance matches at the first two radiating frequencies were not as good as those obtained for the plain cone antenna. It did, however, improve the match for the much higher third radiation frequency.

6.2.2 SLOTTED-CONE ANTENNA 2

The measured results of the prototype antenna with an annular slot of s_d = 15 mm and h_s = 26.25 mm are presented and discussed here. The picture of the fabricated slotted-cone is shown in Fig. 6.14, similar to the slotted cone antenna 1 discussed in Section 6.2.1 except for the difference in the slot-depth. The S_{11} of the prototype plain cone antenna and the slotted-cone antenna 2 are compared in Fig. 6.15.

Fig. 6.14: Prototype cone with s_d = 15 mm single slot at h_s = 26.25 mm.

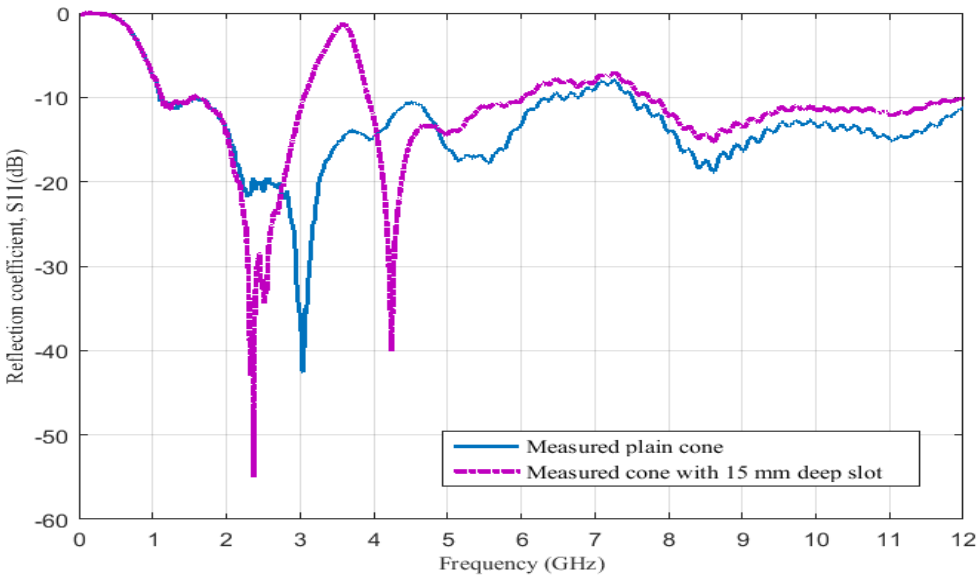

Fig. 6.15: Comparison of the measured S_{11} for plain cone (—) and cone with slot (-•-): s_d = 15 mm and h_s = 26.25 mm.

In line with the simulated result shown in Fig. 6.5 for the 15 mm deep slot, there was a clear anti-resonant frequency between 3.06 - 3.91 GHz. This means that, as with the slotted cone measured in Section 6.1.2, the antenna demonstrated a stopband. The frequency ranges affected in this case were

lower compared with those affected by the 7.5 mm slot in Section 6.2.1. These results confirm the conclusion drawn from the simulations: the frequency range affected by the slot is predominantly related to the depth of the slot(s). If this property is explored, the antenna can be customised to preferentially radiate or receive signals at a given frequency band while suppressing others. This could be a useful tool to be harnessed in frequency selection or for prevention of interference where antennas operating within a common band are being used for different purposes in the same environment.

Like the 7.5 mm deep slot, the presence of the slot produced three distinct bands in the measured S_{11} parameter plot: 1.59 - 3.05 GHz, 3.92 - 6.03 GHz and 7.73 - 12 GHz. The bandwidth of the fundamental resonant frequency became narrower compared to that of the cone without slot but it displayed wider band in comparison to the 7.5 mm deep slotted-cone especially at the two higher resonant frequencies. It was also observed that the 15 mm deep slotted-cone antenna has better match for the first two bands compared to the slotted cone with 7.5 mm depth.

As predicted in the simulations, the cone with the 15 mm deep slot was observed to display a trap with bandwidth starting from a lower frequency compared to both the plain cone and the cone with 7.5 mm deep slot. This shift in the operating frequency was not very significant with the relatively shallow slot of the slotted-cone antenna 1, meaning the shift is relative to the depth of the slot. This implies that the electrical length of the antenna became longer with the input of these slots as theoretically expected and the level of impact is relative to the depth of the slot. These results show that a solid cone antenna can be miniaturised by cutting slots of strategically calculated depth into the body of the cone. There are other variables that could affect this result such as the width of the slot on the characteristics of the antenna but keeping the slot location and the s_w constant and varying the

s_d in Section 6.1.3 has shown that the depth of the slot plays a significant role in the behaviour of the slotted cone antenna.

Cutting of a slot in the cone is also advantageous in reducing the weight of the antenna. Solid cone antennas are generally known for their weight and cutting slots into the cone would not only increase the antenna's electrical length but it will also reduce the weight of the antenna by the volume of the material removed to form the slot. These results show that, with effective placement and well calculated depth, a slot can be used to modify the antenna bandwidth for different applications.

6.2.3 SLOTTED-CONE ANTENNA 3

For this antenna, there are two annular slots on the cone. The picture of the fabricated cone showing the position of the slots on the cone is shown in Fig. 6.16. The S_{11} of the prototype plain cone antenna and the slotted cone antenna 3 are compared in Fig. 6.17.

Fig. 6.16: Prototype cone with 2 slots: s_d = 15 mm at h_s = 26.25 mm and s_d = 7.5 mm at h_s = 18.75 mm.

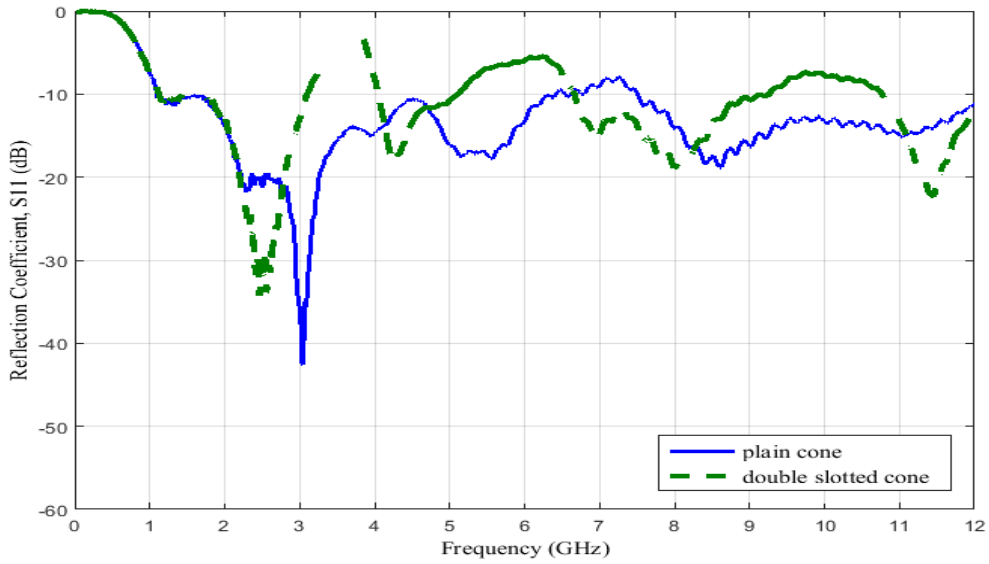

Fig. 6.17: Comparison of the measured S_{11} for plain cone (—) and cone with double slots (- -).

The measured result shown in Fig. 6.17 agreed with the simulated result obtained in Section 6.1.4 (see Fig. 6.9). There are two anti-resonant frequencies associated with each of the two slots between 3.10 - 4.03 GHz and 5.18 - 6.57 GHz. This means that multiple stopbands can be created by the use of multiple slots. The fundamental frequency of the measured result shifted to a lower value confirming the increase in the electrical length of the antenna with the presence of the two slots as theoretically expected, and as predicted by the simulated results.

To further check the effect of multiple slots on the performance of the conical monopole, the resonance of double-slotted cone was compared with resonances of the plain cone and the single-slotted cones (slotted cone antenna 1and 2) as shown in Fig. 6.18.

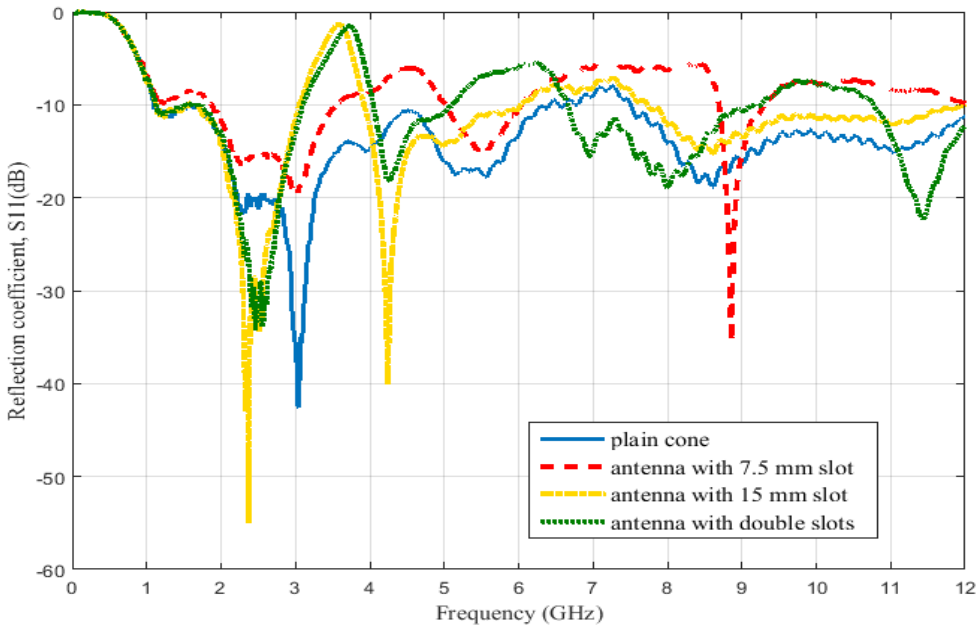

Fig. 6.18: Comparison of the measured S_{11} for plain cone (—) with cone antennas 1, 2 and 3.

It was observed from Fig. 6.17 that unlike the single-slotted cone that produced three frequency bands, the double-slotted cone produced four frequency bands at: 1.18 - 3.09 GHz, 4.05 - 5.09 GHz, 6.66 - 9.19 GHz and 10.77 - 12 GHz. The antenna match for all the bands was fairly maintained at the same level with the match of the original cone. These results show that with effective placement and well calculated depth, a slot can be used to manipulate the width of an antenna bandwidth.

6.2.4 DIELECTRIC LOADED SLOTTED-CONE ANTENNAS

The slots were loaded with dielectric material of $\varepsilon_r = 2.5$. The dielectric material was printed from polyamide material (ε_r = 2.4 - 2.7) using a 3D printer. The effective ε_r of the dielectric material is likely lower than the specified value because the printed material had some air trapped in it during the printing process, which could not be quantified. The measured results for the dielectric loaded single- and double-slotted cones are

presented in Fig. 6.19 and 6.20 respectively. In line with the theoretical expectation, the trap frequencies were shifted to lower values as a result of the dielectric loading. The effect was more pronounced in the loaded double-slotted cone result than in the loaded single-slotted cone. It is important to note that the dielectric load also brought about a reduction in the bandwidth of the antenna compared to the slotted-cone without dielectric load.

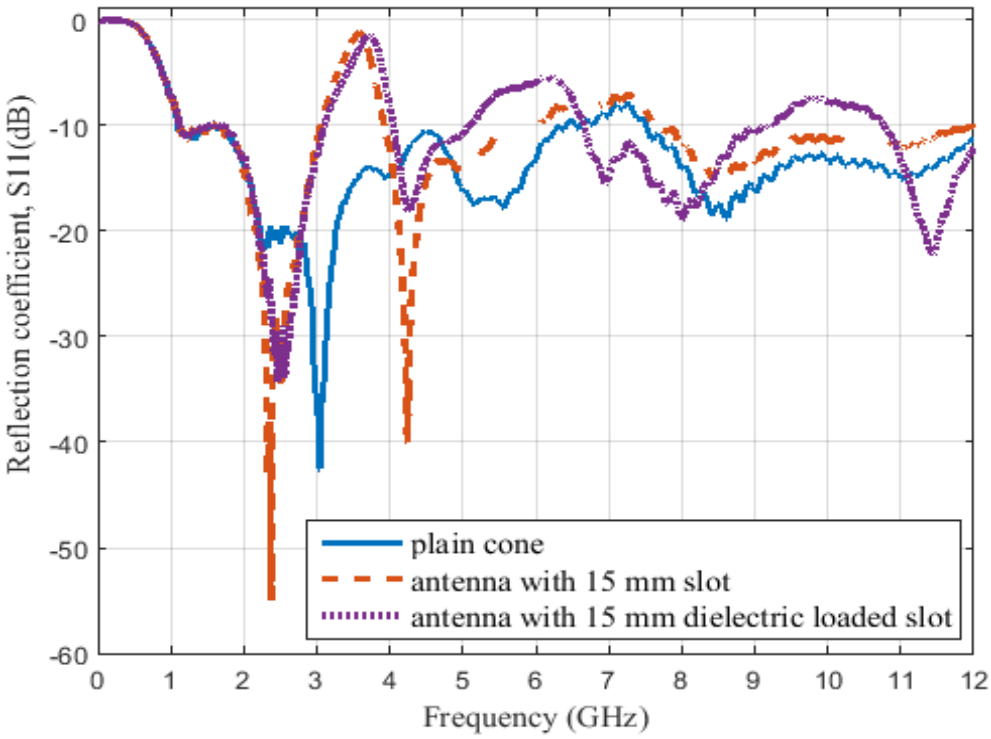

Fig. 6. 19: Comparison of the measured S_{11} for plain, unloaded and loaded slotted cones (s_d = 15 mm at h_s = 26.25 mm).

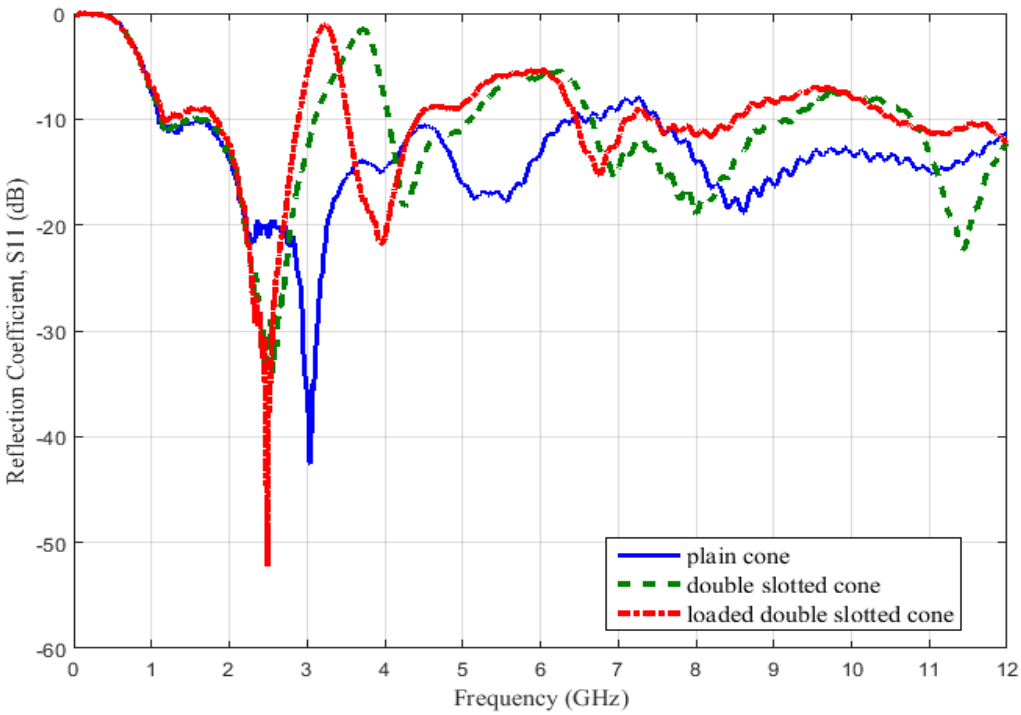

Fig. 6. 20: Comparison of the measured S_{11} for plain cone (—), unloaded (- - -) and loaded (-•-) double slots cones (s_d = 7.5 mm at h_s = 18.75 mm and s_d = 15 mm at h_s = 26.25 mm).

6.3 CONCLUSIONS

The concept of adding slots to a solid cone antenna has been described in this Chapter. The addition of the slot to the cone produced anti-resonances as theoretically predicted. Parametric studies on the effects of slot parameters such as its position, depth, width and permittivity (dielectric loading) on the performance of the solid cone antenna was carried out. The anti-resonant frequencies produced by the slots varied inversely proportional with the depth of the slots such that deeper slots produced anti-resonance at lower frequencies while the relatively shallow slot produced anti-resonance at higher frequencies. Increase in the slot-width was found to widen the bandwidth of the stopband created by the anti-resonant frequencies. The application of double slots to the cone produced a wider stopband and the widths of the two slots were found to be cumulative in their relationship. Dielectric loading of the slots produced a little shift in the operating frequency of the antenna but further research is required to fully quantify the effect of the slot-loading on the general characteristics of the antenna. The prototype antennas were fabricated and measured to verify the simulated results and agreement between the measured results and the simulated is good.

These features displayed by the slotted-cone antennas can be used as a tool for adjusting the operation bandwidth of a cone antenna and to reject a band of unwanted frequencies.

CHAPTER 7

CONCLUSIONS

The aim of this thesis was to develop efficient technique for modelling of axisymmetric radiating structures using a numerical method. The TLM technique was chosen because of its many attractive features. A short review of the fundamentals of TLM including a brief history of TLM and an introduction to the analogies of TLM to Maxwell's equations in rectangular and cylindrical coordinates was presented. The outcome of this research is the development of a 3D modelling tool for axisymmetric radiating structures such as cylindrical dipoles, cylindrical monopoles, conical monopoles and slotted cone antennas. The model was validated by fabricated prototypes of the simulated antennas as well as by comparison with analytical models and a commercial rectilinear TLM solver (CST) where appropriate. This Chapter summarises the contribution of this research and suggests areas for future research.

7.1 Contributions of the Thesis

- An electromagnetic solver was developed for this research based on the TLM algorithm written in MATLAB. The solver was termed *Transmission Line Solver, TLS.*

- Canonical problems with known theoretical solutions were simulated with the intention to validate the rectangular part of the developed code (TLS). Reports of the electromagnetic simulation of some

canonical problems using 2D shunt TLM mesh and 3D symmetrical condensed node were presented and compared to that of the analytical results for validation purposes. The simulation results obtained from an existing modelling tool, CST, are also presented for the validation of newly developed solver. The effect of stair-cased approximation on curved boundaries when modelling with rectangular TLM mesh is highlighted.

- The fundamentals of cylindrical TLM were presented and the relationship of the cylindrical TLM and to the Maxwell's equations was discussed. The implementation of the cylindrical TLM algorithm was described and the simulated results for benchmarked microwave problems solved with cylindrical mesh were presented and discussed. The quantitative comparison of the cylindrical and the rectangular TLM mesh was also presented along with the improvement obtained by modelling the curved boundaries using cylindrical mesh instead of the rectangular mesh.

- The application of the cylindrical TLM to the modelling of axisymmetric radiating structures was described. A brief review of cylindrical dipole, cylindrical monopole and conical monopole antennas and description of the modelling procedures for the simulated of the three antennas using TLS were presented. The simulated results were compared with the measured results of fabricated prototype cylindrical and conical monopole antennas and were found to be in good agreement.

- The modelling of axisymmetric conical antennas with incorporated slots was described. The solid cone monopole with slot cut into the body of the cone at strategically calculated locations were simulated and the parametric studies to determine the effects of the slot-

position, slot-width, slot-depth and multiple slots on the performance on the antenna was conducted. In addition, the effects of loading the slotted antennas, by filling the slots with dielectric material of known permittivity value, on the radiation characteristics of the antennas were investigated and reported in this Chapter.

7.2 Suggestions for Further Research

- A Dirac impulse function was used for the excitation for all simulations reported in this thesis. It is well known that the Fourier Transform of a Dirac impulse function is a wideband response ranging from 0 - ∞. This brings some spurious modes into the simulated results and some of these resonances have very high amplitude that dwarfs the desired resonances to be extracted from the problem space. There are different approaches to dealing with this problem. One of such approaches is to use a controlled input such as cosine, sinusoidal or Gaussian input. Another approach is to filter either the input or output with a low pass or bandlimited filter. Exploring the best approach to extracting simulated data from the simulation space would be part of the work that will be done to enhance the solver.

- Calculation of parameters such as radiation pattern, s-parameter, gain and antenna effectiveness would be focus of future work.

- The visualisation of results at the moment is limited. The impacts of different modifications on the antenna such as effect of the slot load on the antenna performance are better relayed in terms of visualisation of the result. These are possible addition to the code in the near future.

- The boundary used in terminating the simulation space edge for the antenna simulating edge was a simple absorbing boundary with a reflection coefficient of 0. Addition of a PML absorbing boundary to the model will enhance the effectiveness of the boundary. Further study on the centre boundary of the cylindrical mesh for radiating structures is also essential.

- An extended parameter studies on the slotted cones could give a lot of useful data.

- Creation of a user interface for the solver. This will make it easier for individual with little or no understanding of the code to use it easily and makes it accessible to the general public.

REFERENCES

[1] B. P. Johns, R. L. Buerle, “Numerical Solution of 2-Dimensional Scattering Problems using a Transmission-Line Matrix,” *Proced. IEE*, vol. 118, p. 1203-1208, 1971.

[2] P. B. Johns, “The Art of Modelling,” *Electron. Power*, vol. 25, no. 8, pp. 565–569, 1979.

[3] C. Christopoulos, *The Transmission-Line Modeling Method (TLM)*. IEEE/OUP Press, 1995.

[4] A. R. Ruddle, A. Sarantidis, and D. D. Ward, “Modelling the Installed Performance of Vehicle Mounted Antennas using TLM,” in *National Conference on Antennas and Propagation*, 1999, no. 461, pp. 5–7.

[5] A. R. Ruddle, “Two-Stage Tlm Modelling Approach for More Efficient Analysis of Vehicle Antenna Installations,” in *Antennas and Propagation, EuCAP 2007. The Second European Conference on*, 2007, pp. 1–6.

[6] C. Christopoulos and J. L. Herring, “Application of transmission-line modeling (TLM) to electromagnetic compatibility problems,” *IEEE Trans. Electromagn. Compat.*, vol. 35, no. 2, pp. 185–191, 1993.

[7] A. P. Duffy, T. M. Benson, and C. Christopoulos, “Numerical Modelling of Cavity Backed Apertures using Transmission-Line Modelling (TLM),” in *Antennas and Propagation, 1993., Eighth International Conference on*, 1993, pp. 107–110.

[8] J. L. Dubard, O. Benevello, D. Pompei, J. Le Roux, P. P. M. SO, and W. J. R. Hoefer, “Acceleration of TLM Through Signal Processing and Parallel Computing,” in *Proceedings of the International conference of computation in Electromagnetics*, 1991, pp. 71–74.

[9] F. Ndagijimana, P. Saguet, and M. Bouthinon, “Tapered Slot Antenna Analysis With 3-D TLM Method,” *Electron. Lett.*, vol. 26, no. 7, pp. 468–470, 1990.

[10] P. Sewell, A. Vukovic, T. M. Benson, C. Christopoulos, D. W. P. Thomas, and A. I. Nosich, “Analytic Coupling of Spatially Distinct Unstructured TLM Meshes,” *2006 Int. Conf. Math. Methods Electromagn. Theory*, pp. 89–94, 2006.

[11] T. Dimitrijevic, J. Jokovic, N. Don, and B. Milovanovic, “TLM Modelling of a Microstrip Circular Antenna in a Cylindrical Grid,” *Microw. Rev.*, pp. 28–33, 2013.

[12] O. Agunlejika, J. A. Flint, and R. D. Seager, “Transmission Line Modelling of Axisymmetry Curvilinear Structures,” in *IET Colloquium on Antennas, Wireless and Electromagnetics*, 2014, no. May, pp. 1–18.

[13] Q. Zhang and W. J. R. Hoefer, “Dispersion Analysis of TLM Node for Modeling General Anisotropic and Gyromagnetic Materials,” in *Microwave Symposium Digest, IEEE MTT-s International*, 1996, vol. 2, pp. 1039–1042.

[14] P. Sewell, J. G. Wykes, S. Member, T. M. Benson, S. Member, C. Christopoulos, D. W. P. Thomas, A. Vukovic, and A. Transmission-line, “Transmission-Line Modeling Using Unstructured Triangular Meshes,” *IEEE Trans Microw. theory Tech.*, vol. 52, no. 5, pp. 1490–1497, 2004.

[15] P. Sewell, S. Member, T. M. Benson, C. Christopoulos, D. W. P. Thomas, A. Vukovic, J. G. Wykes, and S. Member, “Transmission-Line Modeling (TLM) Based Upon Unstructured Tetrahedral Meshes,” *IEEE Trans Microw. theory Tech.*, vol. 53, no. 6, pp. 1919–1928, 2005.

[16] D. A. Al-Mukhtar and J. E. Sitch, “Transmission-line matrix method with irregularly graded space,” *IEE Proc. H*, vol. 128, no. 6, pp. 299–305, 1981.

[17] D. De Cogan and S. A. John, “A two dimensional transmission line matrix model for heat flow in power semiconductors,” *J. Phys. D Appl. Physics, Print. Gt. Britain*, vol. 18, pp. 507–516, 1985.

[18] J. Jokovic and T. Dimitrijevic, “TLM cylindrical model of a coaxially loaded cylindrical cavity,” *2011 10th Int. Conf. Telecommun. Mod. Satell. Cable Broadcast. Serv. TELSIKS 2011 - Proc. Pap.*, vol. 2, pp. 420–423, 2011.

[19] H. Youssef and H. Elmokdad, “A Three-Dimensional Transmission Line Matrix Method (TLM) In Cylindrical Coordinates,” pp. 4–9, 2006.

[20] C. A. Balanis, *Antenna Theory: analysis and design*, 2nd ed. John Wiley & Sons, 1997.

[21] C. Christopoulos, “Review of computational electromagnetics in electromagnetic compatibility applications,” *IET 8th Int. Conf. Comput. Electromagn. (CEM 2011)*, pp. 85–85, 2011.

[22] W. J. R. Hoefer, “The Transmission-Line Matrix Method— Theory and Applications,” *IEEE Trans Microw. theory Tech.*, vol. 33, no. 10, pp. 882–893, 1985.

[23] N. S. Doncov and B. D. Milovanovic, “TLM modeling of the circular cylindrical cavity loaded by lossy dielectric sample of various

geometric shapes.," *J. Microw. Power Electromagn. Energy*, vol. 37, no. 4, pp. 237–247, 2002.

[24] R. Scaramuzza and A. J. Lowery, "Hybrid Symmetrical Condensed Node for the TLM Method," *Electron. Lett.*, vol. 26, no. 23, pp. 1947–1949, 1990.

[25] S. Berntsen and S. N. Homsleth, "Retarded Time Absorbing Boundary Conditions," *IEEE Trans. Antennas Propag.*, vol. 42, no. 8, pp. 1059–1064, 1994.

[26] Jian-Ming Jin, *The Finite Element Method in Electromagnetics*, 3rd Editio. New Jersey: John Wiley & Sons, 2014.

[27] H. D. Brüns, C. Schuster, and H. Singer, "Numerical electromagnetic field analysis for EMC problems," *IEEE Trans. Electromagn. Compat.*, vol. 49, no. 2, pp. 253–262, 2007.

[28] J. L. Volakis, A. Chatterjee, and L. C. Kempel, *Finite Element Method for Electromagnetics*. New York, USA: Oxford, UK: IEEE Press; Oxford University Press, 1998.

[29] A. Taflove, *Computational Electromagnetics. The Finite-Difference Time-Domain Method*. Norwood: Artech House, Inc., 1995.

[30] N. R. S. Simons, R. Siushansian, J. LoVetri, and M. Cuhaci, "Comparison of the transmission-line matrix and finite-difference time-domain methods for a problem containing a sharp metallic edge," *IEEE Trans. Microw. Theory Tech.*, vol. 47, no. 10, pp. 2042–2045, 1999.

[31] K. S. Yee, "Numerical Solution of Initial Boundary Value Problems Involving Maxwell's Equations in Isotropic Media," *Antennas Propag.*, vol. 14, no. 3, pp. 302 – 307, 1966.

[32] C. Christopoulos, *The Transmission-Line Modeling (TLM) Method in Electromagnetics*. Morgan and Claypool, 2006.

[33] B. Shanker, M. L. M. Lu, J. Y. J. Yuan, and E. Michielssen, "Time Domain Integral Equation Analysis of Scattering From Composite Bodies via Exact Evaluation of Radiation Fields," *IEEE Trans. Antennas Propag.*, vol. 57, no. 5, pp. 1506–1520, 2009.

[34] G. Kobidze, B. Shanker, and E. Michielssen, "A fast time domain integral equation based scheme for analyzing scattering from dispersive objects," *IEEE Trans. Antennas Propag.*, vol. 53, no. 3, pp. 1215–1226, 2005.

[35] R. F. Harrington, *Field computation by moment methods*. New York, USA: Macmillan, 1968.

[36] R. Coifman, V. Rokhlin, and S. Wandzura, "Fast multiple method for the wave equation: a pedestrian prescription," *IEEE Antennas Propag.*

Mag., vol. 35, no. 3, pp. 7–12, 1993.

[37] P. B. S. Kumar and G. S. Ranganath, "Geometrical theory of diffraction," *Pramana*, vol. 37, no. 6, pp. 457–488, 1991.

[38] M. Clemens and T. Weil, "Discrete Electromagnetism with the Finite Integration Technique," *Prog. Electromagn. Res.*, vol. 32, pp. 65–87, 2001.

[39] A. Taflove and S. C. Hagness, *Computational Electrodynamics: the Finite Difference Time-Domain Method*, 3rd ed. Norwood MA: Artech House, 2005.

[40] Lee Jin-Fa, Lee Robert, and A. Cangellaris, "Time-domain finite-element methods," *IEEE Trans. Antennas Propag.*, vol. 45, no. 3, pp. 430–442, 1997.

[41] P. Sewell, T. M. Benson, A. Vukovic, and A. Al Jarro, "The challenges for numerical time domain simulations of optical resonators," in *2010 12th International Conference on Transparent Optical Networks, ICTON 2010*, 2010.

[42] V. Janyani, T. Benson, and A. Vukovic, "Accurate time domain method for simulation of microstructured electromagnetic and photonic structures," *Int. J. Electr. Comput. Eng.*, vol. 3, no. 11, pp. 720 – 723, 2008.

[43] W. J. R. Hoefer, "Time domain electromagnetic simulation for microwave CAD applications," *IEEE Trans. Microw. Theory Tech.*, vol. 40, pp. 1517–1527, 1992.

[44] N. R. S. Simons and A. Sebak, "Application of the transmission line matrix method to the analysis of scattering by three-dimensional objects," in *IEE Proceedings Microwaves, Antennas and Propagation*, 1995, vol. 142, no. 4, pp. 319–325.

[45] T. H. Hubing, "Survey of Numerical Electromagnetic Modeling Techniques," *Univ. Missouri-Rolla, Electromagn. Compat. Lab.*, p. 20, 1991.

[46] N. R. S. Simons and E. Bridges, "Equivalence of propagation characteristics for the transmission-line matrix and finite-difference time-domain methods in two dimensions," *IEEE Trans. Microw. Theory Tech.*, vol. 39, pp. 354–357, 1991.

[47] Z. Chen, M. M. Ney, and W. J. R. Hoefer, "A new finite-difference time-domain formulation and its equivalence with the TLM symmetrical condensed node," *IEEE Trans. Microw. Theory Tech.*, vol. 39, pp. 2160–2169, 1991.

[48] H. Jin, R. Vahldieck, and S. Member, "Direct Derivations of TLM Symmetrical Condensed Node and Hybrid Symmetrical Condensed Node from Maxwell ' s Equations Using Centered Differencing and

Averaging," *IEEE Trans Microw. theory Tech.*, vol. 42, no. 12, pp. 2554–2560, 1994.

[49] C. Eswarappa and W. J. R. Hoefer, "Bridging the gap between TLM and FDTD," *IEEE Microw. Guid. Wave Lett.*, vol. 6, pp. 4–6, 1996.

[50] N. R. S. Simons, a. a. Sebak, E. Bridges, and Y. M. M. Antar, "Transmission-line matrix (TLM) method for scattering problems," *Comput. Phys. Commun.*, vol. 68, no. 1–3, pp. 197–212, Nov. 1991.

[51] P. B. Johns, "Short Papers," *IEEE Trans Microw. theory Tech.*, vol. MTT- 35, no. 1, pp. 60–61, 1987.

[52] J. Paul, C. Christopoulos, and D. W. P. Thomas, "Generalized material models in tlm-part i: materials with frequency-dependent properties," *IEEE Trans. Antennas Propag.*, vol. 47, pp. 1528–1534, 1999.

[53] P. B. Johns, "A Symmetrical Condensed Node for the TLM Method," *IEEE Transactions on Microwave Theory and Techniques*, vol. 35. pp. 370–377, 1987.

[54] A. P. Duffy and C. Herring, J.L. Benson, T.M. Christopoulos, "The application of transmission-line modelling to EMC design, Does Electromagnetic Modelling Have a Place in EMC Design," *IEE Colloq.*, pp. 5/1 – 5/5, 1993.

[55] P. Russer and J. A. Russer, "Some Remarks on the Transmission Line Matrix (TLM) Method and Its Application to Transient EM Fields and to EMC Problems," in *Computational Electromagnetics—Retrospective and Outlook*, 2015, pp. 29–57.

[56] G. Kron, "Equivalent Circuit of the Field Equations of Maxwell-I," *Proc. IRE*, vol. 32, no. 5, pp. 289 –299, 1944.

[57] C. Huygens, "Traite de la Lumiere," *Soc. Hollandaise des Sci.*, vol. 19, 1967.

[58] P. Russer, "The Transmission Line Matrix Method," in *America*, no. July, 2010, pp. 1–27.

[59] S. Akhtarzad and P. B. Johns, "Generalised elements for TLM method of numerical analysis," *Proc. Inst. Electr. Eng.*, vol. 122, no. 12, pp. 1349–1352, 1975.

[60] W. J. R. Hoefer and P. P. M. So, *The Electromagnetic wave Simulator*. New York: John Wiley & Sons, 1991.

[61] S. Akhtarzad and P. B. Johns, "The solution of Maxwell's Equations in Three Space Dimensions and Time by the TLM Method of Numerical Analysis," in *Proc. Inst. Electr. Eng*, 1975, vol. 122, no. 12, pp. 1344–1348.

[62] V. Trenkic, "The development and characterisation of advanced

nodes for the TLM method. PhD thesis , University of Nottingham.," 1995.

[63] M. Krumpholz, C. Huber, and P. Russer, "A field theorical comparison of FDTD and TLM," *IEEE Trans Microw. theory Tech.*, vol. 43, no. 8, pp. 1935 – 1950, 1995.

[64] P. Saguet and E. Pic, "Utilisation d'un Nouveau Type de Noeud dans la Method TLM en 3 Dimensions," *Electron. Lett.*, vol. 18, no. 11, pp. 478 – 480, 1982.

[65] A. Amri, A. Saidane, and S. Pulko, "Thermal analysis of a three-dimensional breast model with embedded tumour using the transmission line matrix (TLM) method.," *Comput. Biol. Med.*, vol. 41, no. 2, pp. 76–86, Feb. 2011.

[66] M. M. Ney and A. Ijjeh, "Comparison of the Symmetrical Condensed-TLM node with hybrid and super condensed nodes for time-domain field computation in complex media," in *Electromagnetics in Advanced Applications (ICEAA), 2015 International Conference on*, 2015, no. 1, pp. 1194–1197.

[67] R. Scaramuzza; A.J. Lowery, "Hybrid Symmetrical Condensed Node for the TLM method," *Electron. Lett.*, vol. 26, no. 23, pp. 1947–1948, 1990.

[68] J. L. Herring and C. Christopoulos, "Multigrid transmission-line modelling (TLM) method for solving electromagnetic field problems," *Electron. Lett.*, vol. 27, no. 20, pp. 1794–1795, 1991.

[69] J. L. Herring and C. Christopoulos, "Solving electromagnetic field problems using a multiple gridtransmission-line modeling method," *IEEE Trans. Antennas Propag.*, vol. 42, 1994.

[70] J. L. Herring and C. Christopoulos, "The use of graded and multigrid techniques in transmission-line modelling," in *Second International Conference on Computation in Electromagnetics*, 1994, pp. 142–145.

[71] H. Meliani, J. A. Djebbar, and D. De Cogan, "Generation of orthogonal curvilinear meshes in three dimensions," *Int. J. Numer. Model. Electron. Networks, Devices Fields*, vol. 16, no. 5, pp. 401–415, Sep. 2003.

[72] H. Meliani and Y. A. Jebbar, "Application of Orthogonal Curvilinear Meshes to the TLM Method," *6th Saudi Eng. Conf. KFUPM, Dhahran*, vol. 4, pp. 209–221, 2002.

[73] H. Youssef, H. ElMokdad, J. Jomaah, and H. Ayad, "General and complete 2D TLM curvilinear node," *2012 2nd Int. Conf. Adv. Comput. Tools Eng. Appl.*, pp. 128–133, 2012.

[74] P. Berini, S. Member, K. Wu, and S. Member, "A Pair of Hybrid Symmetrical Condensed TLM Nodes," *IEEE Microw. Guid. Wave*

Lett. Microw. Guid. Wave Lett., vol. 4, no. 7, pp. 244–246, 1994.

[75] V. Trenkic, C. Christopoulos, and T. M. Benson, "Generally graded TLM mesh using the symmetrical supercondensed node," *Electron. Lett.*, vol. 30, no. 10, pp. 795–797, 1994.

[76] H. Jin and R. Vahldieck, "The frequency-domain transmission line matrix method-a new concept," *IEEE Trans. Microw. Theory Tech.*, vol. 40, no. 12, pp. 2207–2218, 1992.

[77] J. Meng, L. Zhang, J. Tang, Y. Li, F. He, and H. Xiao, "Computation of Radiated Electric Fields from Cables Using the 1D Time-Domain and Frequency-Domain TLM Methods," in *17th International Conference on Electrical Machines and Systems (ICEMS)*, 2014, pp. 3253–3258.

[78] Z. D. Chen and M. M. Ney, "On the relationship between the time-domain and frequency-domain TLM methods," *IEEE Antennas Wirel. Propag. Lett.*, vol. 7, pp. 46–49, 2008.

[79] S. C. Pomeroy, H. R. Williams, and P. Blanchfield, "Evaluation of ultrasonic inspection and imaging systems for robotics using TLM modelling," *Robotica*, vol. 9, no. 03, p. 283, 1991.

[80] P. Russer and J. A. Russer, "Transmission Line Matrix (TLM) and network methods applied to electromagnetic field computation," *2011 IEEE MTT-S Int. Microw. Symp.*, pp. 1–4, 2011.

[81] C. Lucia and W. J. R. Hoefer, "WEIF-32 Modification of the 3D-TLM Sscattering Matrix to Model Nonlinear Devices in Graded and Heterogenous Regions," *Microw. Symp. Dig. IEEE MTT-s Int.*, vol. 2, pp. 897–900, 1998.

[82] V. Trenkic, T. M. Benson, and C. Christopoulos, "Dispersion analysis of a TLM mesh using a new scattering matrix formulation," *IEEE Microw. Guid. Wave Lett.*, vol. 5, 1995.

[83] C. Christopoulos, *The Transmission-Line Modeling (TLM) Method in Electromagnetics*. United State of America: Morgan & Claypool, 2006.

[84] V. Trenkic, C. Christopoulos, and T. M. Benson, "A graded symmetrical super-condensed node for the TLM method," *Antennas Propag. Soc. Int. Symp. AP-S. Dig.*, vol. 2, pp. 1106–1109, 1994.

[85] V. Trenkic, C. Christopoulos, and T. M. Benson, "Theory of the symmetrical super-condensed node for the TLM method," *IEEE Trans. Microw. Theory Tech.*, vol. 43, no. 6, pp. 1342–1348, 1995.

[86] M. Keskin, U. Moon, and G. C. Temes, "Application of PML to open boundary problem using TLM method," *Electron. Lett.*, vol. 37, no. 4, pp. 213–215, 2001.

[87] V. Trenkic, C. Christopoulos, and T. M. Benson, “On the time step in hybrid symmetrical condensed TLM nodes,” *IEEE Trans. Microw. Theory Tech.*, vol. 43, 1995.

[88] L. Khashan, A. Vukovic, P. Sewell, and T. M. Benson, “Assessment of Accuracy and Runtime Trade-offs in Unstructured TLM Meshes for Electromagnetic Simulations,” *Antennas Propag.*, no. November, pp. 518–523, 2013.

[89] J. A. Flint, “Efficient Automotive Electromagnetic Modelling,” PhD Thesis, Loughborough University, 2000.

[90] C. Christopoulos, “Electromagnetics - ancient and modern,” *AsiaPacific Conf. Appl. Electromagn. 2003 APACE 2003*, pp. 1–4, 2003.

[91] T. M. Duffy, A.P. Johnson, M. Hill, D.J. Benson, “Analysis of microwave resonators using transmission line modelling,” *IEE Proc. - Sci. Meas. Technol.*, vol. 143, no. 6, pp. 362 – 368.

[92] V. Trenkic, C. Christopoulos, and T. M. Benson, “Analytical Expansion of the Dispersion Relation for TLM Condensed Nodes,” *IEEE Trans Microw. theory Tech.*, vol. 44, no. 12, pp. 2223 – 2230, 1996.

[93] J. Nielsen and W. Hoefer, “A complete dispersion analysis of the condensed node TLM mesh,” *IEEE Trans. Magn.*, vol. 27, no. 5, pp. 3982–3985, 1991.

[94] J. A. Morente, G. Gimenez, J. A. Porti, and M. Khalladi, “Dispersion analysis for a TLM mesh of symmetrical condensed nodes with stubs,” *IEEE Trans. Microw. Theory Tech.*, vol. 43, no. 2, pp. 452–456, 1995.

[95] Stothard David, “The Development of an Application Specific Processor for the Transmission Line Matrix Method,” 2000.

[96] N. R. S. Simons and E. Bridges, “Application of Absorbing Boundary Conditions to TLM Simulations,” in *Antennas and Propagation Society International Symposium, AP-S. Merging Technologies for the 90’s. Digest.*, 1990, vol. 1, pp. 2–5.

[97] G. Guillaume and J. Picaut, “A simple absorbing layer implementation for transmission line matrix modeling,” *J. Sound Vib.*, vol. 332, no. 19, pp. 4560–4571, Sep. 2013.

[98] J. A. Morente, J. A. Porti, and Khalladi Mohsine, “Absorbing Boundary Conditions for the TLM Method,” *IEEE Trans Microw. theory Tech.*, vol. 40, no. 11, pp. 2095–2099, 1992.

[99] N. R. S. Simons and E. Bridges, “Method For Modelling Free Space Boundaries in TLM Situations,” *Electron. Lett.*, vol. 26, no. 7, pp. 453–455, 1990.

[100] O. Pertz, B. Muller, U. Muller, and A. Beyer, “Implementing PML boundary conditions in TLM,” *1998 IEEE MTT-S Int. Microw. Symp. Dig. (Cat. No.98CH36192)*, vol. 3, pp. 1731–1734, 1998.

[101] J. L. Dubard and D. Pompei, “Optimization of the PML Efficiency in 3-D TLM Method,” *IEEE Trans. Microw. Theory Tech.*, vol. 48, pp. 1081–1088, 2000.

[102] D. S. Katz, E. T. Thiele, and A. Taflove, “Validation and extension to three dimensions of the berenger PML absorbing boundary condition for FD-TD meshes,” *IEEE Microwave and Guided Wave Letters*, vol. 4, no. 8. pp. 268–270, 1994.

[103] N. R. S. Simons, A. R. Sebak, and G. E. Bridges, “Application of the TLM method to half-space and remote-sensing problems,” *IEEE Trans. Geosci. Remote Sens.*, vol. 33, no. 3, pp. 759–767, 1995.

[104] X. Gui, S. K. Dew, M. J. Brett, and D. de Cogan, “Transmission-line-matrix modeling of grain-boundary diffusion in thin films,” *J. Appl. Phys.*, vol. 74, no. 12, p. 7173, 1993.

[105] Z. Chen, M. M. Ney, and W. J. R. Hoefer, “A New Boundary Description in Two-Dimensional TLM Models,” *IEEE Trans Microw. Theory Tech.*, vol. 39, no. 3, pp. 377 –382, 1991.

[106] F. J. German, “Infinitesimally adjustable boundaries in symmetrical condensed node TLM simulations,” in *9th annual review of progress in applied computational electromagnetics*, 1993, pp. 482–490.

[107] U. Muller, A. Beyer, and W. J. R. Hoefer, “The Implementation of Smoothly Moving Boundaries in,” *IEEE Trans Microw. Theory Tech. MTT40*, pp. 791–792, 1992.

[108] S. J. Porter and J. F. Dawson, “Improved plane-wave illumination for TLM method,” *Electron. Lett.*, vol. 29, no. 18, pp. 1663–1664, 1993.

[109] J. A. Flint, S. C. Pomeroy, and D. D. Ward, “Compact partial Huygen’s surface for TLM,” *Electron. Lett.*, vol. 35, no. 2, pp. 132–133, 1999.

[110] D. M. Pozar, *Microwave Engineering*, 4th ed. United State of America: John Wiley & Sons, 2012.

[111] R. E. Collin, *Foundations for Microwave Engineering (IEEE Press series on electromagnetic wave theory)*, 2nd ed. New York: John Wiley & Sons, 2001.

[112] R. Allen, A. Mallik, and P. Johns, “Numerical Results for the Symmetrical Condensed TLM Node,” *IEEE Trans Microw. Theory Tech. MTT40*, vol. MTT-35, no. 4, pp. 378–382, 1987.

[113] S. V Boriskina, T. M. Benson, P. Sewell, and A. I. Nosich, “Spectral shift and Q-change of circular and square-shaped optical microcavity

modes due to periodic sidewall surface roughness," pp. 1–5, 2005.

[114] J. Nielsen, "Spurious Modes of the TLM-Condensed Node Formulation," *IEEE Microw. Guid. Wave Lett.*, vol. 1, no. 8, pp. 201–203, 1991.

[115] J. L. Herring and W. J. R. Hoefer, "Improved correction for 3-D TLM coarseness error," *Electron. Lett.*, vol. 30, no. 14, p. 1149, 1994.

[116] J. S. Nielsen and W. J. R. Hoefer, "Generalized Dispersion Analysis and Spurious Modes of 2-D and 3-D TLM Formulations," *IEEE Trans. Microw. Theory Tech.*, vol. 41, no. 8, pp. 1375–1384, 1993.

[117] O. Agunlejika, J. A. Flint, and R. D. Seager, "Application of Cylindrical Transmission Line Method to the Modelling of Curvilinear Axisymmetric Radiating Structure," in *Loughborough Antennas and Propagation Conference (LAPC)*, 2014, pp. 340–343.

[118] H. Youssef, H. Elmokdad, H. Ayad, and J. Jamaah, "Dispersion Analysis of a 3D-TLM Particular Curvilinear Node : Cylindrical Node," in *2nd International Conference on Advances in Computational Tools for Engineering Applications CACTCAS*, 2012, pp. 134–139.

[119] D. DeCogan, *Transmission Line Matrix (TLM) Techniques for Diffusion Applications*. CRC Press, 1998.

[120] T. V. C. T. Chan and H. C. Reader, *Understanding Microwave Heating Cavities*. Boston, London: Artech House, 2000.

[121] S. Maruoka, Y. Nikawa, T. Izumikawa, and S. Maji, "Oversized cylindrical cavity to measure complex permittivity in millimeter waves," *2009 Asia Pacific Microw. Conf.*, no. 3, pp. 337–340, Dec. 2009.

[122] H. Kawabata, Y. Kobayashi, and S. Kaneko, "Analysis of Cylindrical Cavities to Measure Accurate Relative Permittivity and Permeability of Rod Samples," in *Proceedings of Asia-Pacific Microwave Conference 2010*, 2010, pp. 1459–1462.

[123] A. Parkash, J. K. Vaid, and A. Mansingh, "Measurement of Dielectric Parameters at Microwave Frequencies by Cavity-Perturbation Technique," *IEEE Trans Microw. theory Tech.*, vol. MTT.27, no. 1, pp. 791–795, 1979.

[124] J. A. Monsoriu, B. Gimeno, E. Silvestre, and M. V. Andres, "Analysis of inhomogeneously dielectric filled cavities coupled to dielectric-loaded waveguides: application to the study of NRD-guide components," *IEEE Trans. Microw. Theory Tech.*, vol. 52, no. 7, 2004.

[125] A. P. Duffy, M. Johnson, D. J. Hill, and T. M. Benson, "Analysis of Microwave Resonators using Transmission Line Modelling," *IEE*

Proc - Sci Meas. Technol, vol. 143, no. 6, pp. 362–368, 1996.

[126] H. Tanaka and A. Tsutsumi, "Resonant Frequency and Q-Factor of a Dielectric-Loaded-Cavity Resonator with a Conductive Layer on Its Metal Wall," *Jpn. J. Appl. Phys.*, vol. 42, no. Part 2, No. 11B, pp. L1400–L1403, Nov. 2003.

[127] E. O. Ammann, "Tunable, Dielectric-Loaded Microwave Cavities Capable of High Q and High Filling Factor," *IEEE Trans. Microw. Theory Tech.*, vol. 11, no. 6, pp. 528–541, 1963.

[128] S. Verdeyme, P. Guillon, S. Vigneron, B. Theron, L. C. Espace-, T. C. Two, and F. E. Method, "A New Dielectric Loaded Cavity for High Power Microwave Filtering," *Optimization*, pp. 615–618, 1996.

[129] B. Milovanovic, N. Doncov, and A. Atanaskovic, "TLM modelling of cylindrical metallic cavity loaded byinhomogeneous dielectric sample," *2000 10th Mediterr. Electrotech. Conf. Inf. Technol. Electrotechnol. Mediterr. Countries. Proceedings. MeleCon 2000 (Cat. No.00CH37099)*, vol. 1, 2000.

[130] S. N. Doncov, B. D. Milovanovic, and S. T. Ivkovic, "Modelling of circular cylindrical metallic cavity loaded by a lossy dielectric sample of various geometries using 3-D TLM method," *Microw. Rev.*, 1998.

[131] P. S. Kooi, M. S. Leong, and S. P. Yeo, "Circular cylindrical cavity loaded with a dielectric sleeve for Gunn-effect oscillator stabilisation application," *IEE Proc. H Microwaves, Antennas Propag.*, vol. 133, no. 4, p. 259, 1986.

[132] A. J. M. Williams, T. M. Benson, and A. P. Duffy, "Determining the accuracy of TLM in simulating the behaviour of resonant cavities with arbitrary dielectric loading," *Int. J. Electron.*, vol. 83, no. 5, pp. 645–660, 1997.

[133] J. L. McDonald and D. S. Filipovic, "On the Bandwidth of Monocone Antennas," *IEEE Trans. Antennas Propag.*, vol. 56, no. 4, pp. 1196–1201, Apr. 2008.

[134] N. I. Khan, A. Azim, and S. Islam, "Radiation Characteristics of a Quarter-Wave Monopole Antenna above Virtual Ground," *J. Clean Energy Technol.*, vol. 2, no. 4, pp. 339–342, 2014.

[135] M. Antoniou, V. Sizov, C. Hu, P. Jancovic, R. Abdullah, N. E. a Rashid, and M. Cherniakov, "The concept of a forward scattering micro-sensors radar network for situational awareness," *Proc. 2008 Int. Conf. Radar, Radar 2008*, pp. 171–176, 2008.

[136] V. Sizov, M. Gashinova, N. E. a. Rashid, N. a. Zakaria, P. Jancovic, and M. Cherniakov, "FSR Sensors Network: Performance and Parameters," *7th EMRS DTC Tech. Conf. – Edinburgh 2010 A13*, no. 1, p. 11, 2010.

[137] M. N. Majid, N. E. A. Rashid, S. Subahir, and M. T. Ali, “Miniature Stub-Loaded Monopole Antenna at 800 MHz for FSR sensor,” in *Digital Information and Communication Technology and it’s Applications (DICTAP), 2014 Fourth International Conference on*, 2014, pp. 357–362.

[138] W. Wiesbeck, G. Adamiuk, and C. Sturm, “Basic properties and design principles of UWB antennas,” *Proc. IEEE*, vol. 97, pp. 372–385, 2009.

[139] J. G. Maloney and G. S. Smith, “Optimization of a conical antenna for pulse radiation: an efficient design using resistive loading,” *IEEE Trans. Antennas Propag.*, vol. 41, no. 7, pp. 940–947, Jul. 1993.

[140] R. W. P. King and S. S. Sandler, “Compact conical antennas for wide-band coverage,” *IEEE Trans. Antennas Propag.*, vol. 42, pp. 436–439, 1994.

[141] S. Palud, F. Colombel, M. Himdi, and C. Le Meins, “Compact multi-octave conical antenna,” *Electronics Letters*, vol. 44. p. 659, 2008.

[142] Y. K. Yu and J. Li, “ANTENNAS,” *Prog. Electromagn. Res. Lett.*, vol. 1, pp. 85–92, 2008.

[143] T. Taniguchi and T. Kobayashi, “An omnidirectional and low-VSWR antenna for ultra-wideband wireless systems,” *Proc. RAWCON 2002. 2002 IEEE Radio Wirel. Conf. (Cat. No.02EX573)*, vol. 2, no. c, pp. 145–148, 2002.

[144] C. B. Mulenga and J. A. Flint, “Radiation characteristics of a conical monopole antenna with a partially corrugated ground plane,” *2009 Loughbrgh. Antennas Propag. Conf.*, pp. 517–520, 2009.

[145] P. Sewell, Y. K. Choong, and C. Christopoulos, “An accurate thin-wire model for 3-d tlm simulations,” *IEEE Trans. Electromagn. Compat.*, vol. 45, no. 2, pp. 207–217, May 2003.

[146] H. Schelkunoff, S.A. and Friis, *Antennas: Theory and Practice*. New York: Wiley, 1952.

[147] Q. I. N. Chunlan and J. Gao, “Analysis Design and Application of Sphere Loaded Monopole Antenna,” vol. 100876, no. 69931030, pp. 131–134.

[148] H. Aliakbarian, M. Azarbadegan, M. M. Danei, and J. Rashed-Mohassel, “Design of Skull-Cap Ended Monoconical Antenna for Ultra Wideband Systems,” *2006 Int. Conf. Math. Methods Electromagn. Theory*, vol. 1, no. 2, pp. 121–123, 2006.

[149] E. Hallén, *Electromagnetic Theory*. London: Chapman and Hall, 1962.

[150] B. Rao, J. Ferris, and W. Zimmerman, “Broadband characteristics of

cylindrical antennas with exponentially tapered capacitive loading," *1967 Antennas Propag. Soc. Int. Symp.*, vol. 5, 1969.

[151] S. Palud, F. Colombel, M. Himdi, and C. Le Meins, "A Novel Broadband Eighth-Wave Conical Antenna," *IEEE Trans. Antennas Propag.*, vol. 56, pp. 2112–2116, 2008.

[152] G. B. Gentili, M. Cerretelli, and L. Cecchi, "Coated Conical Antennas for Automotive Application," *J. Electromagn. Waves Appl.*, vol. 18, no. 1, pp. 85–97, Jan. 2004.

[153] B. D. Popovic, "Theory of cylindrical antennas with arbitrary impedance loading," *Proc. Inst. Electr. Eng.*, vol. 118, no. 10, pp. 1327 –1332, 1971.

[154] R. King and T. Wu, "The imperfectly conducting cylindrical transmitting antenna," *IEEE Trans. Antennas Propag.*, vol. 14, no. 5, pp. 524–534, Sep. 1966.

[155] L. Shen, "An experimental study of the antenna with nonreflecting resistive loading," *IEEE Trans. Antennas Propag.*, vol. 15, no. 5, pp. 606–611, Sep. 1967.

[156] S. K. Oleksiy, "A Compact Biconical Antenna With Improved Radiation Pattern," *Union Radio Sci. Int. (URSI)-2008*, pp. 2–5, 2008.

[157] S. R. Best and S. Member, "A Multiband Conical Monopole Antenna Derived From a Modified Sierpinski Gasket," vol. 2, pp. 205–207, 2003.

[158] V. O. Doroshenko, O. E. Strelnytskyi, and O. O. Strelnytskyi, "Excitation of the Slot Conical Antenna (Theory and Experiment)," in *X International Conference on Antenna Theory and Techniques*, 2015, pp. 5–7.

[159] C. B. Mulenga, "The Application of Periodic Structures to Conical Antenna Design," PhD Thesis, Loughborough University, 2009.